

International Journal of

# **Rotating Machinery**

Special Issue  
Rotating Machinery in Renewable Energy Systems

Lead Guest Editor: Ali Mostafaeipour

Guest Editors: Ahmad Sedaghat, Mamdouh H. Assad, Tareq S. Z. Salameh, and Rafat Al-Waked



---

# **Rotating Machinery in Renewable Energy Systems**

International Journal of Rotating Machinery

---

## **Rotating Machinery in Renewable Energy Systems**

Lead Guest Editor: Ali Mostafaeipour

Guest Editors: Ahmad Sedaghat, Mamdouh H. Assad,  
Tareq S. Z. Salameh, and Rafat Al-Waked



---

Copyright © 2018 Hindawi. All rights reserved.

This is a special issue published in “International Journal of Rotating Machinery.” All articles are open access articles distributed under the Creative Commons Attribution License, which permits unrestricted use, distribution, and reproduction in any medium, provided the original work is properly cited.

---

## Editorial Board

H. Joon Ahn, Republic of Korea  
Ryoichi Samuel Amano, USA  
Sourabh V. Apte, USA  
Farid Bakir, France  
Hans Joerg Bauer, Germany  
Gerard Bois, France  
Ch. Earls Brennen, USA  
Alessandro Corsini, Italy  
Luis Gato, Portugal

Awatef Hamed, USA  
Jechin Han, USA  
Hooshang Heshmat, USA  
D. T. Hountalas, Greece  
Norihiko Iki, Japan  
M. Tariq Iqbal, Canada  
Funazaki Ken-ichi, Japan  
Akira Murata, Japan  
M. Razi Nalim, USA

Eddie Ng Yin Kwee, Singapore  
Yutaka Ohta, Japan  
Ion Paraschivoiu, Canada  
Paolo Pennacchi, Italy  
Sergio Preidikman, USA  
Meinhard T. Schobeiri, USA  
Terrence W. Simon, USA  
Seung Jin Song, Republic of Korea

# Contents

---

## **Rotating Machinery in Renewable Energy Systems**

M. El Haj Assad, Tareq Salameh, Ali Mostafaepour , Ahmad Sedaghat, and Rafat Al-Waked   
Editorial (2 pages), Article ID 9034934, Volume 2018 (2018)

## **Static Mechanical Properties and Modal Analysis of a Kind of Lift-Drag Combined-Type Vertical Axis Wind Turbine**

Fang Feng , Chunming Qu, Shouyang Zhao, Yuedi Bai, Wenfeng Guo, and Yan Li   
Research Article (13 pages), Article ID 1840914, Volume 2018 (2018)

## **Research on Aerodynamic Characteristics of Straight-Bladed Vertical Axis Wind Turbine with S Series Airfoils**

Fang Feng , Shouyang Zhao, Chunming Qu, Yuedi Bai, Yuliang Zhang, and Yan Li   
Research Article (13 pages), Article ID 8350243, Volume 2018 (2018)

## **Fault Tolerant Control of Internal Faults in Wind Turbine: Case Study of Gearbox Efficiency Decrease**

Younes Ait El Maati , Lhoussain El Bahir , and Khalid Faitah  
Research Article (8 pages), Article ID 9538489, Volume 2018 (2018)

## **Time-Dependent Effects of Glaze Ice on the Aerodynamic Characteristics of an Airfoil**

Narges Tabatabaei , Michel J. Cervantes, and Chirag Trivedi  
Research Article (14 pages), Article ID 2981739, Volume 2018 (2018)

## **Axial Fan Performance under the Influence of a Uniform Ambient Flow Field**

Till Heinemann  and Stefan Becker  
Research Article (10 pages), Article ID 6718750, Volume 2018 (2018)

## **Design, Modeling, and CFD Analysis of a Micro Hydro Pelton Turbine Runner: For the Case of Selected Site in Ethiopia**

Tilahun Nigussie, Abraham Engeda, and Edessa Dribssa  
Research Article (17 pages), Article ID 3030217, Volume 2017 (2018)

## Editorial

# Rotating Machinery in Renewable Energy Systems

**M. El Haj Assad,<sup>1</sup> Tareq Salameh,<sup>1</sup> Ali Mostafaeipour ,<sup>2</sup>  
Ahmad Sedaghat,<sup>3</sup> and Rafat Al-Waked <sup>4</sup>**

<sup>1</sup>*Sustainable and Renewable Energy Engineering Department, University of Sharjah, P.O. Box 27272, Sharjah, UAE*

<sup>2</sup>*Department of Industrial Engineering, Yazd University, Iran*

<sup>3</sup>*Department of Mechanical Engineering, Australian College of Kuwait, Kuwait*

<sup>4</sup>*Department of Mechanical and Maintenance Engineering, German Jordanian University, Jordan*

Correspondence should be addressed to Ali Mostafaeipour; mostafaei@yazd.ac.ir

Received 27 September 2018; Accepted 27 September 2018; Published 18 October 2018

Copyright © 2018 M. El Haj Assad et al. This is an open access article distributed under the Creative Commons Attribution License, which permits unrestricted use, distribution, and reproduction in any medium, provided the original work is properly cited.

Renewable energy systems performance was studied by many researchers during the last decade in order to help in reducing greenhouse gas emissions as well as having energy at lower cost than that of conventional energy sources. Among the renewable energy sources is wind energy which is considered to be the most friendly renewable energy source. However, the design of wind turbine is not an easy task for engineers due to its large blades which are exposed to a wind velocity at high elevation causing vibration within the whole system. Rotor is another important component which needs to be controlled from speed point of view in the presence of gearbox which requires lubrication. Moreover, the exposure of wind turbine to very severe weather (ambient conditions) in cold countries causes turbine blades icing. In the paper titled “Static Mechanical Properties and Modal Analysis of a Kind of Lift-Drag Combined-Type Vertical Axis Wind Turbine,” F. Feng et al. developed a prototype of lift-drag-vertical axis wind turbine based on finite element methods to obtain structural design and vibration profile. The aerodynamics of S series airfoils on straight-bladed vertical axis wind turbine was investigated numerically and experimentally by F. Feng et al. in the paper titled “Research on Aerodynamic Characteristics of Straight-Bladed Vertical Axis Wind Turbine with S Series Airfoils.” These authors obtained that S series airfoil for SB-VAWT is worth researching deeply.

The control method for the speed of wind turbine under the fault of gearbox efficiency due to lack of lubrication was presented by Y. A. El Maati et al. in the paper titled “Fault

Tolerant Control of Internal Faults in Wind Turbine: Case Study of Gearbox Efficiency Decrease.” The authors evaluated the effectiveness of this method and its convergence with the rotor parameter.

The dynamic oscillation load acting over a glazed-iced airfoil was simulated numerically by N. Tabatabaei et al. in the paper titled “Time-Dependent Effects of Glaze Ice on the Aerodynamic Characteristics of an Airfoil.” The authors found that the higher frequency has the same characteristics of shedding mode while the lower frequency has the flapping mode characteristics.

The integral influence of uniform ambient flow field on a single axial fan over a wide operating range was tested inside wind tunnel by T. Heinemann and S. Becker in the paper titled “Axial Fan Performance under the Influence of a Uniform Ambient Flow Field.” The authors found that the straight-bladed fan reacted less sensitively than the forward skewed fan.

The Pelton turbine for micro hydro potential site was studied by CFD in terms of design, modeling, and performance by T. Nigussie et al. in the paper titled “Design, Modeling, and CFD Analysis of a Micro Hydro Pelton Turbine Runner: For the Case of Selected Site in Ethiopia.” They showed that the model is highly dependent on the size of Pelton turbine.

The authors contributing to this special issue highlight the recent challenges in rotating machinery in renewable energy as in wind and hydro energy systems.

Finally, this special issue will provide guidance on how to design and control the performance of turbomachinery systems such as VAWT, axial fan, and Pelton turbine.

### **Conflicts of Interest**

The authors declare that they have no conflicts of interest.

*M. El Haj Assad  
Tareq Salameh  
Ali Mostafaeipour  
Ahmad Sedaghat  
Rafat Al-Waked*

## Research Article

# Static Mechanical Properties and Modal Analysis of a Kind of Lift-Drag Combined-Type Vertical Axis Wind Turbine

Fang Feng <sup>1,2</sup>, Chunming Qu,<sup>3</sup> Shouyang Zhao,<sup>3</sup> Yuedi Bai,<sup>3</sup>  
Wenfeng Guo,<sup>3</sup> and Yan Li <sup>2,3</sup>

<sup>1</sup>College of Science, Northeast Agricultural University, Harbin, China

<sup>2</sup>Heilongjiang Provincial Key Laboratory of Technology and Equipment for Utilization of Agricultural Renewable Resources in Cold Region, Harbin 150030, China

<sup>3</sup>College of Engineering, Northeast Agricultural University, Harbin, China

Correspondence should be addressed to Fang Feng; [fengfang@neau.edu.cn](mailto:fengfang@neau.edu.cn) and Yan Li; [liyanneau@163.com](mailto:liyanneau@163.com)

Received 27 October 2017; Revised 5 July 2018; Accepted 30 July 2018; Published 7 August 2018

Academic Editor: Tareq S. Z. Salameh

Copyright © 2018 Fang Feng et al. This is an open access article distributed under the Creative Commons Attribution License, which permits unrestricted use, distribution, and reproduction in any medium, provided the original work is properly cited.

In order to explore a set of methods to analyze the structure of Lift-Drag Combined-Type Vertical Axis Wind Turbine (LD-VAWT), a small LD-VAWT was designed according to the corresponding Standards and General Design Requirements for small vertical axis wind turbines. The finite element method was used to calculate and analyze the static mechanical properties and modalities of main parts of a kind of small-scale LD-VAWT. The contours of corresponding stress and displacement were obtained, and first six-order mode vibration profiles of main parts were also obtained. The results show that the main structure parts of LD-VAWT meet the design requirements in the working condition of the rated speed. Furthermore, the resonances of all main parts did not occur during operation in the simulations. The prototype LD-VAWT was made based on the analysis and simulation results in this study and operated steadily. The methods used in this study can be used as a reference for the static mechanical properties and modal analysis of vertical axis wind turbine.

## 1. Introduction

The vertical axis wind turbine (VAWT) has a simple structure and does not need special device to catch the wind. In addition, it is environmentally friendly; therefore, it has a rapid development in recent years. Among them, the Straight-Bladed Vertical Axis Wind Turbine (SB-VAWT) has been studied more deeply due to better power characteristics and higher transfer efficiency of wind energy. However, the starting characteristic is not well, which is one of the important factors restricting the development of SB-VAWT [1]. Therefore, improving the starting characteristics of SB-VAWT has become the research focus for many scholars [2]. Tang Jing et al. [3] have installed wind hood at the top and bottom of the SB-VAWT to increase the flow speed which can improve the start-up performance of wind turbine; Wu Zhicheng et al. [4] have changed symmetric wind rotor into eccentric wind rotor in order to improve the starting torque of

the wind turbine. The theoretical calculations and model tests for the aerodynamic characteristics are numerous; however, the analysis of static and dynamic mechanical properties of wind turbine structure for designing prototype is little. M. SaqibHameed et al. [5] have shown that larger centrifugal load mainly causes bending deformation of blade and used finite element method to compare the mechanical properties of blades made in aluminum and glass fibre reinforced plastic (FRP). The results show that FRP is more suitable to blade material; Lin Wang [6] has used the finite element analysis and genetic algorithm to optimize the structure and weight of blade in the requirement of strength; Zhang Tingting et al. [7] have analyzed the dynamics of the main axis of Darrieus wind turbine, calculated the range of wind speed which can avoid resonance, and obtained the optimal thickness of tube wall of main axis; Wang Jianyu [8] has analyzed the influence of blade shedding vortex on the dynamics of tower and main axis. The research shows that shedding vortex can induce

TABLE 1: Basic structural parameters of LD-VAWT.

Name	Symbol	Value
Rated power [kW]	$P$	3
Rated wind speed [m/s]	$V$	10
Wind rotor diameter [mm]	$d$	4000
Wind rotor height [mm]	$H$	5200
Number of main blades	$N$	3
Chord length of main blade [mm]	$c$	400
Airfoil of main blade	—	NACA0018
Attack angle of main blade [°]	$\beta$	0
Drag rotor diameter [mm]	$d$	700
Drag rotor height [mm]	$h$	2600
Mounting position of drag rotor [mm]	$S$	250

resonance; Nidal H. Abu-Hamdeh [9] used ANSYS to model the majority of the structural components of a collapsible vertical axis wind turbine, and data from the mathematical models were used to verify the structure of the turbine and shafts were within acceptable stress and strain limits, the result of the experiments verified the mathematical simulation analysis; Yu Tang [10] used ANSYS Workbench static and modal analysis module to make load analysis of wind turbine internal maintenance lifting platform and obtained the maximum stress of platform bridge structure and place and form of deformation; E. Verkinderen [11] analyzed the coupled structure through a multidegree of freedom system, as well as numerically through the finite element (FE) method of H-Darrieus vertical axis wind turbines; Zheng Li [12] presented a method to simulate wind turbine gearbox system with the multibody drivetrain dynamic analysis software, and the modal analysis of wind turbine gearbox can be carried out on the basis of the multibody dynamic theory. The above researches are only focused on the analysis of common vertical axis wind turbine. However the analysis on the structure of LD-VAWT is little and it does not build a perfect set of designing plan and methods yet. Therefore, this paper will search on the static and dynamic mechanical properties of structure based on a small-scale lift-type vertical axis wind turbine [13–21] and propose a set of suitable research plans and methods as references to other kinds of LD-VAWTs and vertical axis wind turbines.

## 2. Design of Wind Turbine

**2.1. Wind Turbine Model.** The model of LD-VAWT designed is shown in Figure 1, and the basic structural parameters are shown in Table 1.

**2.2. Structure Design of Wind Turbine.** (1) Wind Rotor: The wind rotor of LD-VAWT is an important part, which can convert wind energy into mechanical energy. It is composed of main blade, drag rotor, beam, main axis, and so on. The main blade is made of FRP which has characteristics of being light, having high strength, having corrosion resistance, and being manufactured easily. The main blade is hollow and

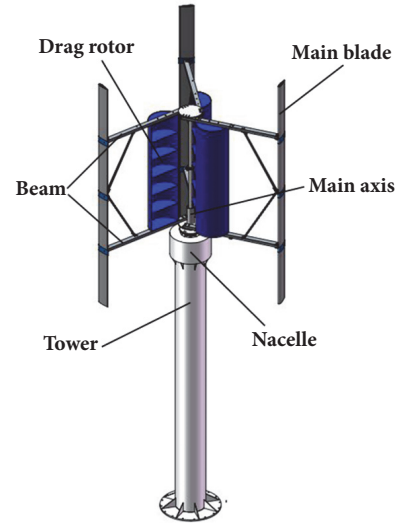


FIGURE 1: Model of LD-VAWT.

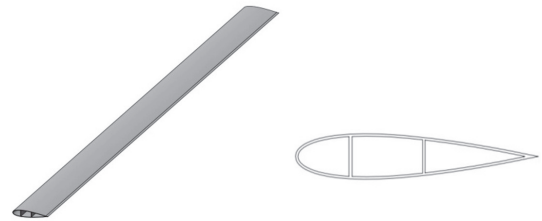


FIGURE 2: The structure of main blade.

stiffened by two ribs, which can reduce the weight of blade. The main blade is shown in Figure 2.

The shape of drag rotor is a semicylindrical surface with thin wall thickness. In order to reduce the weight in the premise of strength requirement, the aluminum alloy material is selected. The thickness of aluminum plate is 3 mm. The structure of drag rotor is shown in Figure 3.

In Figure 1 the beams support the main blades and transmit the torque generated by blade to the main axis. In



FIGURE 3: The structure of drag rotor.

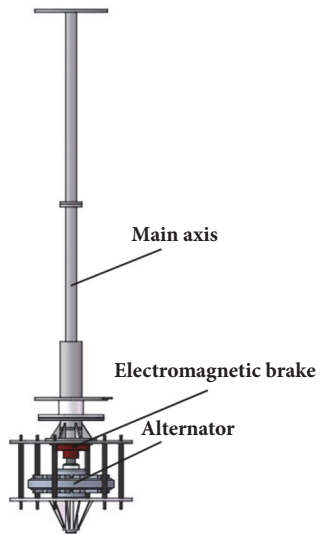


FIGURE 4: The structure of nacelle.

order to enhance bending strength, the square steel is selected as structure of beam. The material of square steel is Q235. The size of cross section is  $60 \times 60$  mm and thickness of wall is 3 mm.

(2) Nacelle: The nacelle consists of alternator, electromagnetic brake, main axis, and support bars as shown in Figure 4. The alternator is disc-type permanent magnet synchronous generator. The dynamic friction torque of brake is 400 N·m.

The main axis in the nacelle is an important part in designing process. The diameter of axis is designed based on the analog method and empirical method. The minimum diameter of main axis is 40 mm and a pair of angular contact ball bearings with model number 7214 is used.

(3) Tower: The role of the tower is to support and fix the wind rotor and nacelle. The material of tower is Q235,

TABLE 2: The parameters of tower.

Name	Value
Height [m]	6
Outside diameter [mm]	630
Inside diameter [mm]	616
Wall thickness [mm]	8

TABLE 3: Material properties of main blade.

Name	Value
Density [ $\text{kg}/\text{m}^3$ ]	$2 \times 10^3$
Elastic Modulus [MPa]	$7.2 \times 10^4$
Yield limit [MPa]	450
Poisson ratio	0.22
Allowable stress [MPa]	320

the structure is shown in Figure 1, and the configuration parameters are shown in Table 2.

### 3. Static Mechanical Property Analysis Structure

**3.1. Main Blade.** The loads of main blade during operation mainly include self-gravity  $G_L$ , centrifugal force load  $F_{rL}$  caused by the rotation, and aerodynamic load  $F_{pL}$  from wind. According to theoretical calculation, the self-gravity  $G_L$  is 312 N, the centrifugal force  $F_{rL}$  is 6843 N, and the wind load  $F_{pL}$  is 95.6 N.

The static mechanical property of main blade is analyzed by finite element method (FEM). The tetrahedral element is selected as mesh type of main blade and the element type is Solid186. Finally, the finite element model of blade has 616368 elements and 212397 nodes. The material of main blade is FRP and the material properties are shown in Table 3.

In order to simulate the connected relation between main blade and beam, a fixed constraint is added at the connection point. Then the wind load is applied on the windward surface of main blade by pressure, the main blade weight is calculated by mass, and gravity acceleration and the centrifugal force are calculated by the rotational inertia load. The loads above are applied on the model of main blade. Finally, the contours of stress and displacement under the rated operation conditions can be obtained as shown in Figures 5 and 6.

From Figure 5, the maximum stress of blade is 45.4 MPa which appears at the connection between main blade and beam. The limited stress of FRP is 320 MPa and the safety factor is 1.5 in this design. Then the ultimate allowable tensile stress of FRP is 213 MPa. According to simulation results, the structural strength of main blade meets design requirements [22]. From Figure 6, the maximum node displacement of main blade appears at the tip of the blade and the value is 15.1 mm, which is larger than the deformation of middle part. It shows that the deformation has less influence on the dynamic characteristics of the wind turbine, which means the structure meets the design requirements [23, 24].

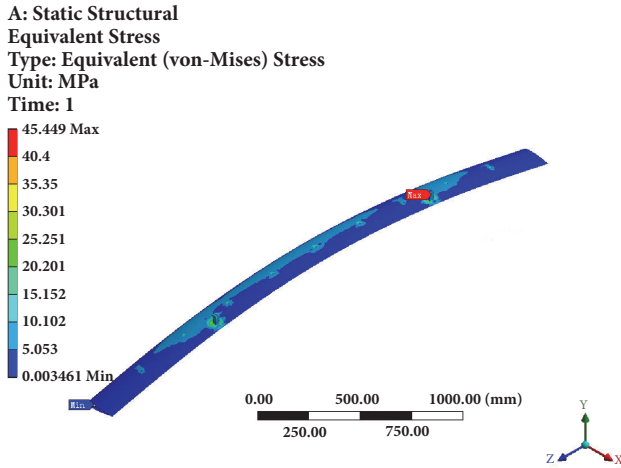


FIGURE 5: Equivalent stress contour of main blade.

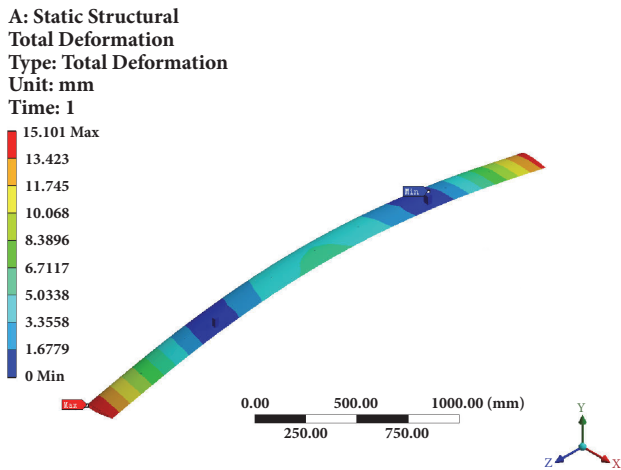


FIGURE 6: Displacement variation contour of main blade.

3.2. *Drag Rotor.* The calculating method of mechanical property of drag rotor is the same as main blade. The self-gravity  $G_D$  is 210 N, the centrifugal force  $F_{rD}$  is 1381.75 N, and the wind load  $F_{pD}$  is 56.77 N.

The solid 185 element is used to mesh and the number of elements and nodes are 457865 and 6956782, respectively. The material of drag rotor is aluminum alloy and the material properties are shown in Table 4.

In the analysis process, the nodes on the upside surface and downside surface of drag rotor are restrained. After calculation, the contours of stress and displacement under the rated condition are obtained as shown in Figures 7 and 8, respectively.

From Figure 7, the maximum stress of drag rotor is 161.4 MPa which is lower than the limit stress of aluminum alloy. Figure 8 shows that the drag rotor has a little displacement, which satisfies the design requirements.

3.3. *Beam.* The maximum load of beam happens at the rated speed 100 r/min of wind rotor. Therefore, analyses of the stress and deformation of beam are processed under the rated speed

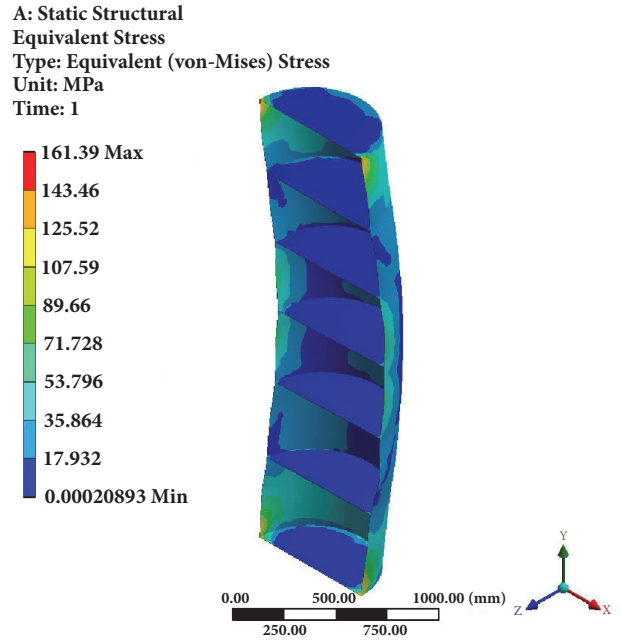


FIGURE 7: Equivalent stress contour of drag rotor.

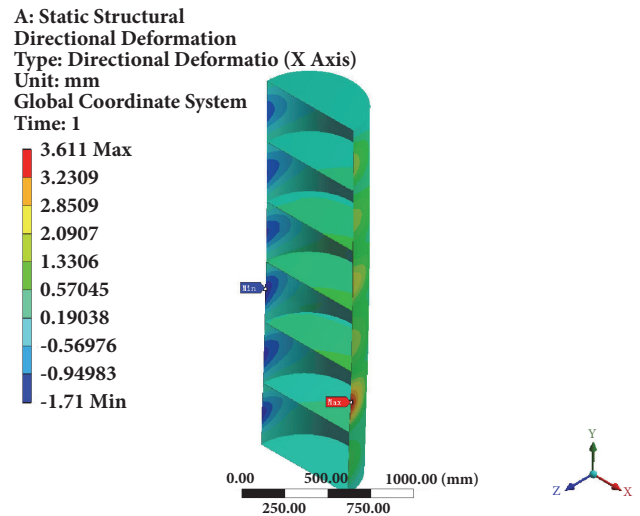


FIGURE 8: Displacement variation contour of drag rotor.

TABLE 4: Material properties of drag rotor.

Name	Value
Density [kg/m <sup>3</sup> ]	$2.7 \times 10^3$
Elastic Modulus [MPa]	$6.9 \times 10^4$
Yield limit [MPa]	276
Poisson ratio	0.33
Tensile strength [MPa]	350

condition. Force and torque can be calculated as shown in Table 5. The material of beam is Q235-A (16Mn) and the properties are shown in Table 6.

TABLE 5: Load distribution of beam.

Name	Value
Self-gravity [N]	115
Gravity of main blade [N]	156
Gravity of drag rotor [N]	105
Torque of main blade [N·m]	119.2
Torque of drag rotor [N·m]	645
Self-centrifugal force [N]	120.4
Centrifugal force of main blade [N]	3421.4
Centrifugal force of drag rotor [N]	808.5

TABLE 6: Material properties of beam.

Name	Value
Density [kg/m <sup>3</sup> ]	$7.86 \times 10^3$
Elastic Modulus [GPa]	211
Yield limit [MPa]	196
Poisson ratio	0.3
Tensile strength [MPa]	235

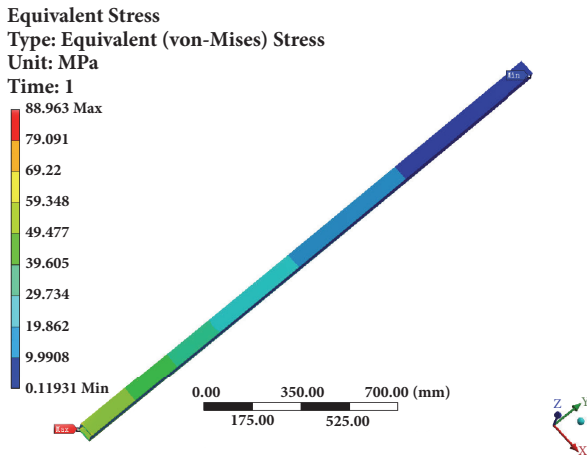


FIGURE 9: Equivalent stress contour of beam.

The Degrees of Freedom (DOF) are constrained on the displacements of X, Y, and Z directions at the end of connection position of beam and main axis. Then the gravity load, centrifugal load, and torque load are applied on the model, respectively. The contours of stress and displacement of beam under the rated condition are obtained by calculation as shown in Figures 9 and 10, respectively.

From Figure 9, the maximum stress is 89 MPa, which appears at the end of connection position between beam and main axis. Therefore the junction should be strengthened. From Figure 10, the maximum displacement happens at the tip of beam where the lift and drag force is fixed and the maximum deformation is 2.4 mm. The strength of beam needs to meet the checking formula (1)

$$\delta_{\max} < \frac{[\delta]}{S} \quad (1)$$

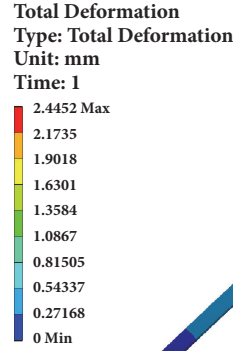


FIGURE 10: Displacement variation contour of beam.

TABLE 7: Received force of main axis.

Name	Value
Gravity of main axis [N]	630
Gravity of wind rotor [N]	3250
Torque of wind rotor [N·m]	1045
Centrifugal force of wind rotor [N]	0

TABLE 8: Material parameters of main axis.

Name	Value
Density [kg/m <sup>3</sup> ]	$7.86 \times 10^3$
Elastic Modulus [MPa]	$2 \times 10^5$
Yield limit [MPa]	400
Poisson ratio	0.3
Tensile strength [MPa]	980

where  $\delta_{\max}$  is the maximum stress,  $[\delta]$  is yield limit stress of material, in this paper  $[\delta]$  is 235 MPa, and  $[S]$  is safety factor, which is selected as 1.5.

From the calculation,  $\delta_{\max}$  is lower than allowable stress. The stiffness checking formula is shown as follows:

$$\frac{\omega_{\max}}{l} < \frac{[\omega_{\max}/l]}{S} \quad (2)$$

where  $\omega_{\max}$  is the maximum displacement of beam, 2.4 mm,  $l$  is the length of beam, 2 m, and  $[\omega_{\max}/l]$  is the allowable deflection of simply supported beam,  $l/500$ .

After calculating,  $\omega_{\max}/l = 1.2 \times 10^{-3} \text{ m} < [\omega_{\max}/l]/S = 2.6 \times 10^{-3} \text{ m}$ , the stiffness of beam under the rated speed meets the design requirements.

**3.4. Main Axis.** The main axis is mainly subjected to gravity load, centrifugal load, and aerodynamic load. The values of loads are shown in Table 7.

In the static mechanical analysis of main axis, tetrahedral element is used to mesh grids. The numbers of elements and nodes are 87536 and 159853, respectively. The material of main axis is 40Cr, and the properties are shown in Table 8.

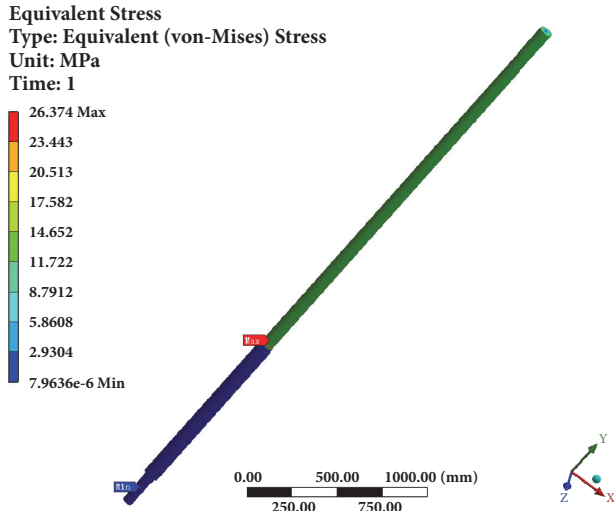


FIGURE 11: Equivalent stress contour of main axis.

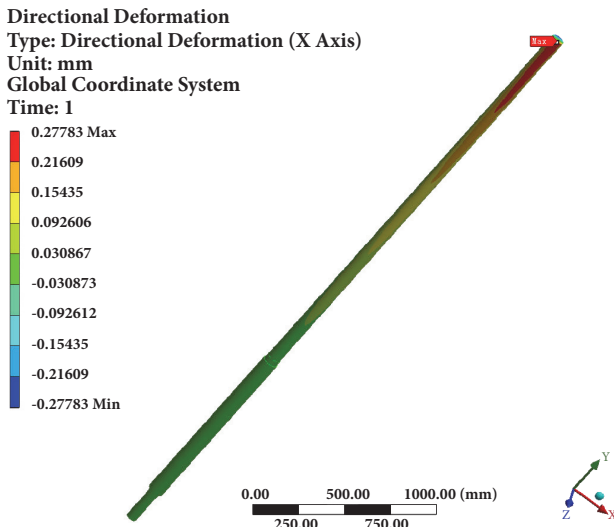


FIGURE 12: Displacement variation contour of axis.

According to the assembly relation, the end of main axis connected with generator is constrained. The self-gravity load of main axis is applied with gravity acceleration, the gravity of wind rotor is applied at mounting position of flange, and the torque of wind rotor is also applied at mounting position of flange. The simulation results are shown in Figures 11 and 12, respectively.

From Figure 11, the maximum stress of main axis is 26.3 MPa which is at the connection position between beam and main axis. From Figure 12, the maximum displacement is at the top of main axis which is 0.27 mm.

According to formula (1), maximum stress of main axis  $\delta_{\max}$  is 26.3 MPa, limit stress  $[\delta]$  is 980 MPa, and safety factor  $S$  is 3. The maximum stress  $\delta_{\max}$  is lower than allowable stress.

TABLE 9: Load distribution of tower.

Name	Value
Horizontal thrust [N]	1132.4
Gravity of wind rotor and cabin [N]	8330
Self-gravity of tower [N]	8291
Torque of cabin [N·m]	286.5
Wind pressure [N/m]	27.1

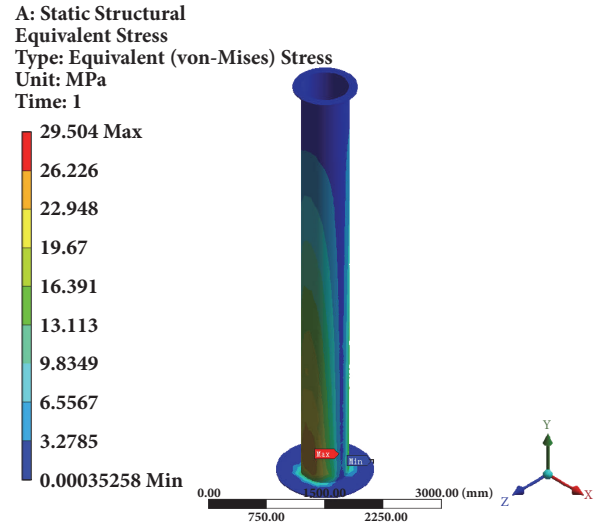


FIGURE 13: Equivalent stress contour of tower.

Similarly the stiffness of main axis needs to meet the stiffness checking formula as follows:

$$y_{\max} \leq 0.0005l \quad (3)$$

where  $y_{\max}$  is the maximum deformation of main axis and  $l$  is the length of main axis, 3400 mm.

The calculation result shows that the maximum deformation of main axis is 0.27 mm.

**3.5. Tower.** The tower is mainly subjected to horizontal thrust of the wind rotor, the gravity of wind rotor and nacelle, self-gravity, the torque of wind rotor, and the wind pressure acting on the tower. The values of loads distributing on the tower are shown in Table 9.

The material of tower is Q235 and the solid 185 is selected as element type. The numbers of elements and nodes are 15696 and 30864, respectively.

The bottom of tower is constrained. The above loads are applied on the model of tower and the contours of stress and deformation of tower are shown in Figures 13 and 14, respectively.

From Figure 13, the maximum stress of tower is 29.5 MPa which appears at the bottom of tower. From Figure 14, the maximum deformation of tower is 5.3 mm. According to the engineering experience of tower designing [25], the maximum deformation of tower should be less than 0.5~0.8% of its height for tower. The limit stress of Q235 is

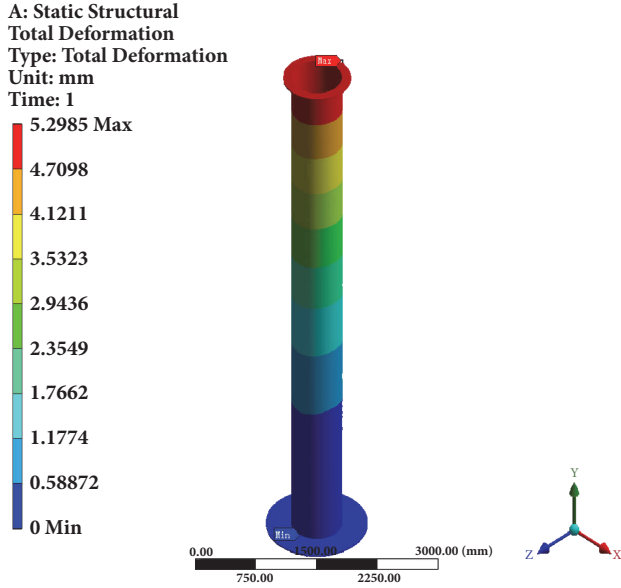


FIGURE 14: Total deformation contour of tower.

TABLE 10: The first six-order mode natural frequency of main blade.

Order	Value
First order [Hz]	18.0535
Second order [Hz]	18.0543
Third order [Hz]	28.2657
Fourth order [Hz]	75.4023
Fifth order [Hz]	80.6801
Sixth order [Hz]	80.7842

156.7 MPa which is higher than the maximum stress 29.5 MPa in Figure 14.

#### 4. Modal Analysis

When the wind turbine works in natural environment, the load is complex and changeable. The power of air, inertia force, and elasticity force applied on the blades of wind turbine can make blade and tower deform and oscillate. If the frequency of exciting force approaches the natural frequency of the structure, the resonance may lead to damage of wind turbine. In order to avoid resonance, the natural frequency of wind turbine should be different from the one of wild exciting force. Therefore, the modal analysis should be carried out during the structural design of wind turbine.

**4.1. Main Blade.** The model of main blade used in the modal analysis is the same as statistic analysis. The low-order mode of main blade has a great influence on stability and fatigue of blade, and the first six-order modes and the natural frequencies are calculated which are shown in Table 10. The vibration modes are shown in Figure 15.

TABLE 11: The first six-order mode natural frequency of drag rotor.

Order	Value
First order [Hz]	50.2653
Second order [Hz]	50.3117
Third order [Hz]	50.3735
Fourth order [Hz]	50.4092
Fifth order [Hz]	50.4428
Sixth order [Hz]	76.6961

TABLE 12: The first six-order mode natural frequency of main axis.

Order	Value
First order [Hz]	8.35907
Second order [Hz]	8.35938
Third order [Hz]	52.2301
Fourth order [Hz]	52.2319
Fifth order [Hz]	145.56
Sixth order [Hz]	145.565

From Figure 15, the frequency of first order is 18.0535Hz and the first-order critical rotational speed of main blade is calculated as following formula:

$$n_0 = 60f \quad (4)$$

The first-order critical rotational speed  $n_0$  is 1083 r/min, which is higher than rotational speed of main blade. It means that the resonance of main blade will not occur during operation.

**4.2. Drag Rotor.** The model of drag rotor used in the modal analysis is the same as the static analysis. Similarly the frequencies of first six-order modes are shown in Table 11 and the vibration modes are shown in Figure 16.

From Figure 16, the natural frequency of first-order is 50.2653Hz, and the first critical rotational speed of drag rotor calculated by the formula (4) is 3016 r/min. The rotational speed of drag rotor is far lower than the critical rotational speed, which means that the resonance of blade will not occur during the operation.

**4.3. Main Axis.** The main axis is one of the important parts of wind rotor and nacelle, which not only needs to check the strength and stiffness but also avoid resonance phenomenon. Therefore, based on the model of static mechanical property analysis, the natural frequencies of first six-order modes of main axis are shown in Table 12 and the vibration mode of main axis are shown in Figure 17.

From Figure 17, the frequency of first-order mode is 8.35907 Hz. When the wind rotor works at the rotational speed 100 r/min, the exciting frequency subjected by main axis from wind rotor is 1.667 Hz. However, the natural frequency of first-order is 8.35907 Hz and it is higher than

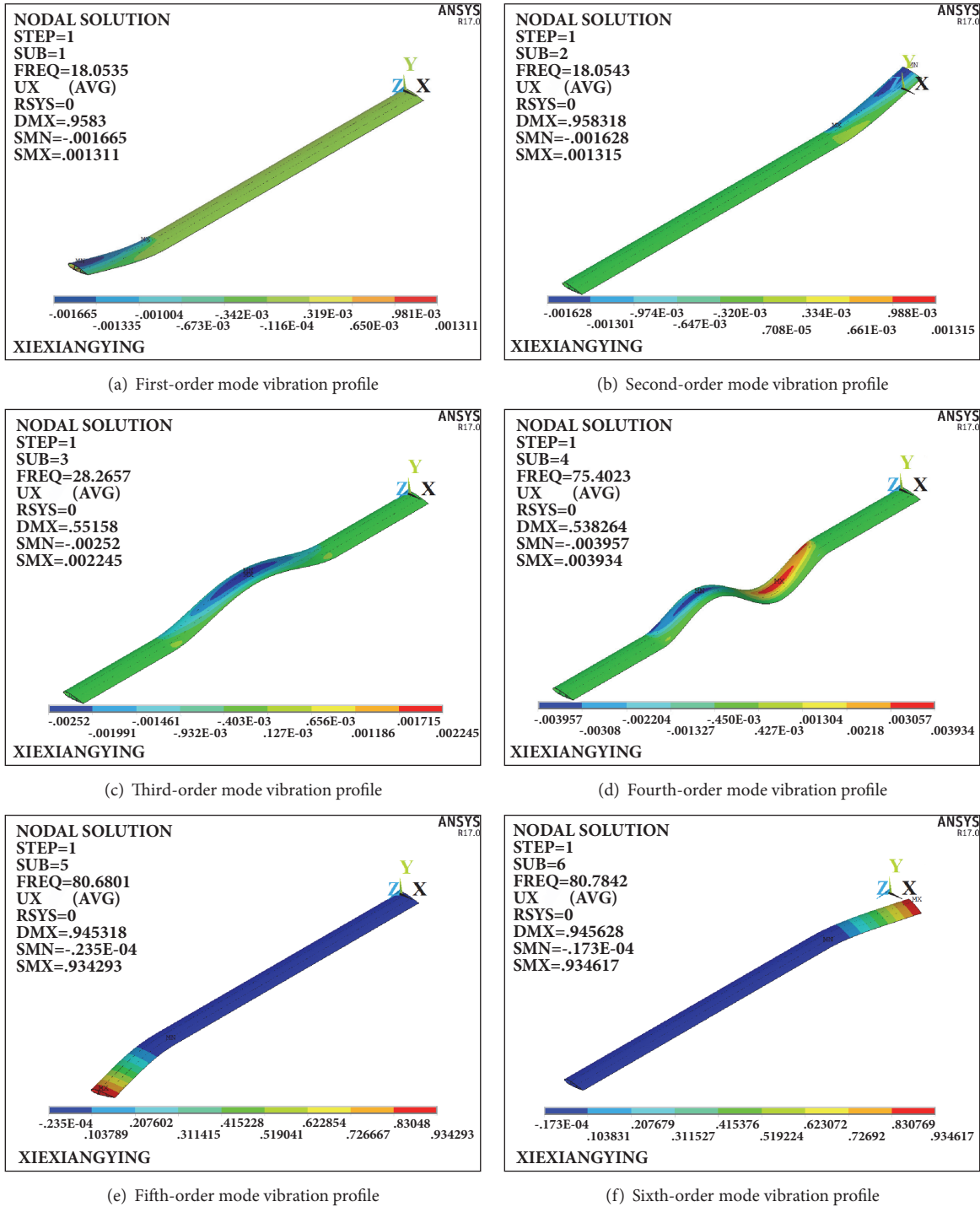


FIGURE 15: The first six-order mode vibration profile of main blade.

the work frequency, which means that the resonance will not occur during the operation.

4.4. Tower. Similarly the FEM model of tower in the modal analysis is the same as the static mechanical property analysis and the contact surfaces between tower and ground are

constrained. The natural frequencies of first six-order mode of tower are shown in Table 13, and the vibration modes of tower are shown in Figure 18.

From Figure 18, the frequency of first-order mode is 15.2166 Hz. According to what has been mentioned previously the frequency  $f_1$  of wind rotor under the rated speed is

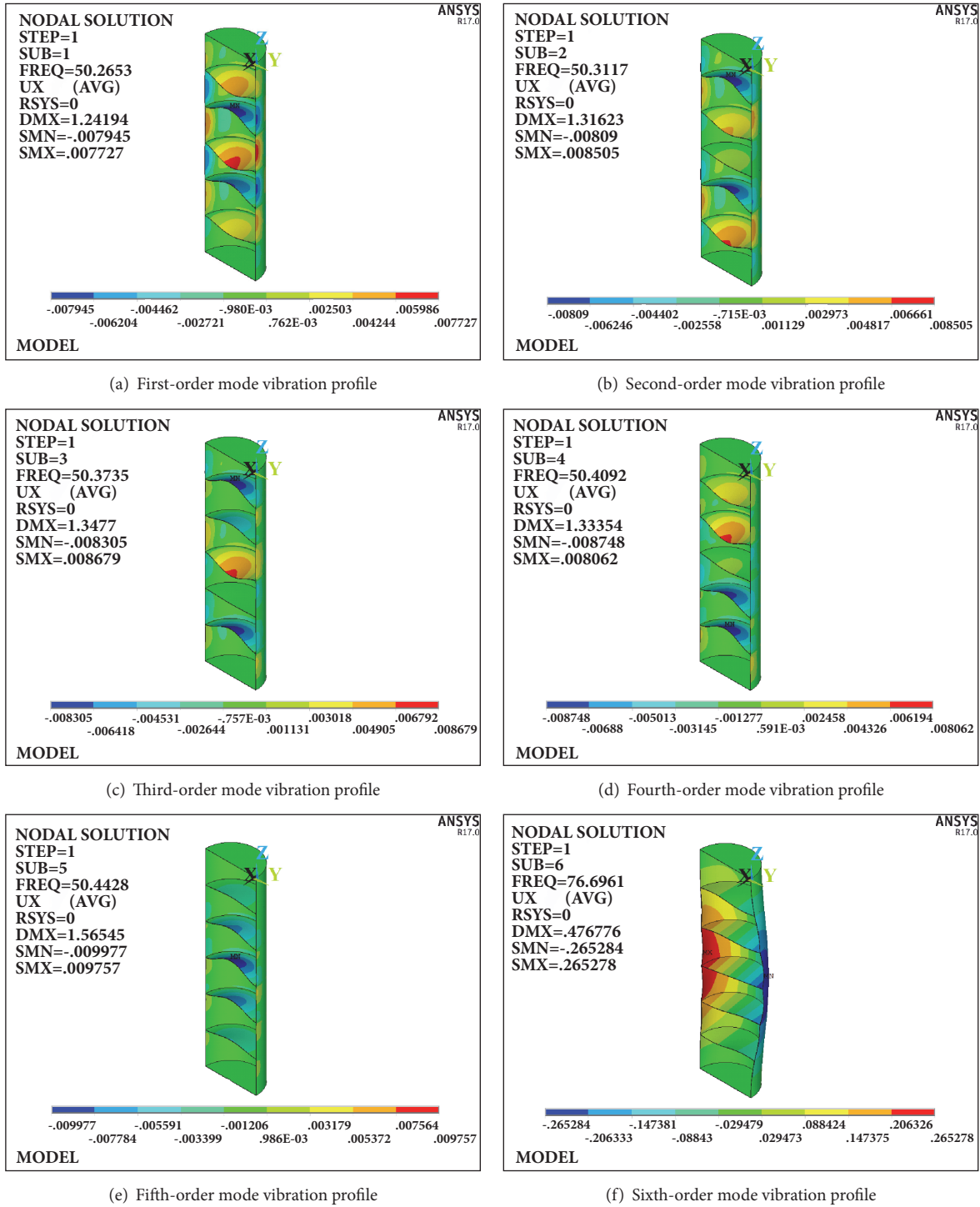
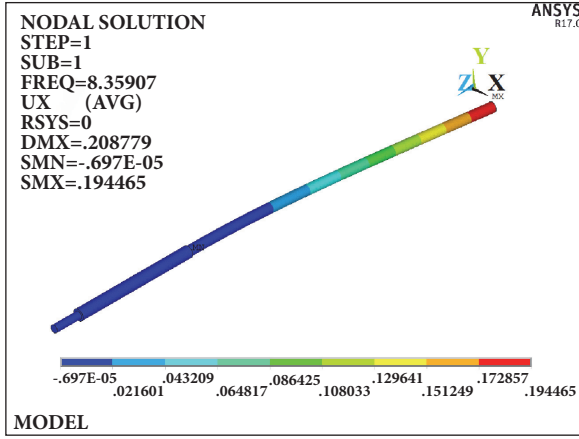


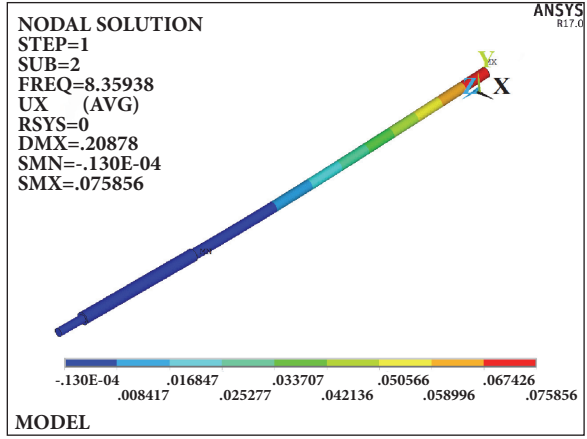
FIGURE 16: The first six-order mode vibration profile of drag rotor.

TABLE 13: The first six-order mode natural frequency of tower.

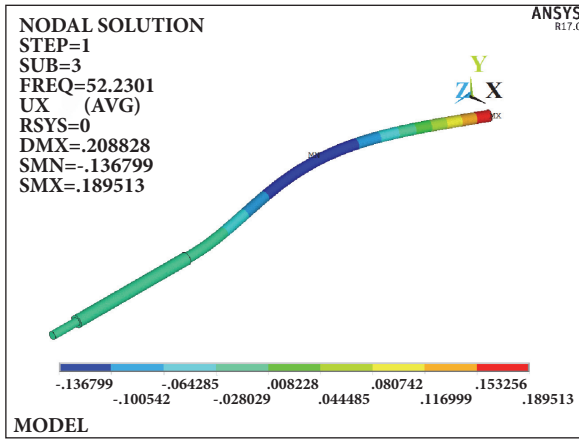
Order	Value
First order [Hz]	15.2166
Second order [Hz]	15.2166
Third order [Hz]	88.6749
Fourth order [Hz]	88.6749
Fifth order [Hz]	120.362
Sixth order [Hz]	168.738



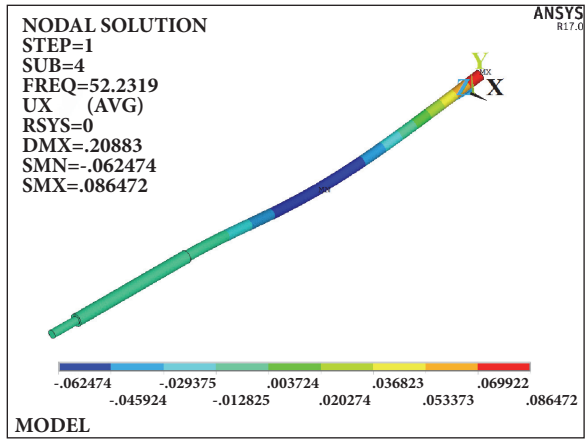
(a) First-order mode vibration profile



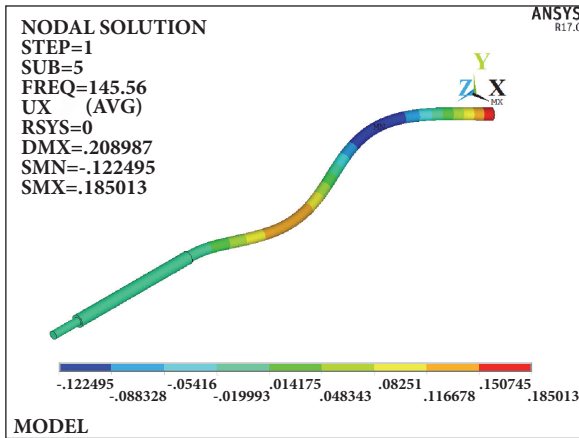
(b) Second-order mode vibration profile



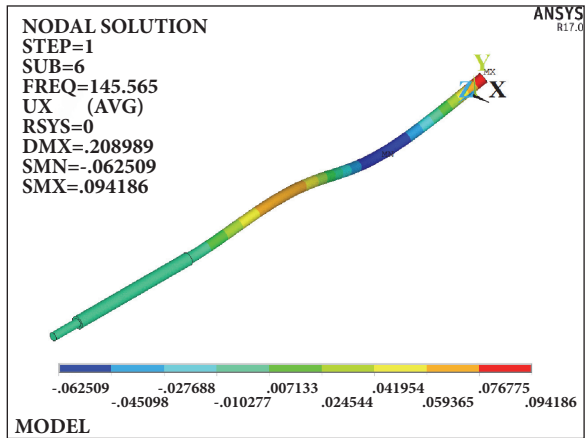
(c) Third-order mode vibration profile



(d) Fourth-order mode vibration profile



(e) Fifth-order mode vibration profile



(f) Sixth-order mode vibration profile

FIGURE 17: The first six-order mode vibration profile of main axis.

1.67 Hz. The wind rotor has three blades; therefore the passage frequency  $f_2$  of the main blades is 5.01 Hz. According to the engineering experience [26], the first-order frequency  $f_{01}$  of tower must be higher than the passage frequency  $f_2$  of the blade and meet the formula:

$$\frac{(f_{01} - f_{02})}{f_2} \geq 10\% \quad (5)$$

The calculated results meet above conditions, which means that the excitation of wind rotor will not cause the tower to resonate.

### 5. Prototype of LD-VAWT

According to the design of LD-VAWT with the static mechanical property and modal analysis, the results show

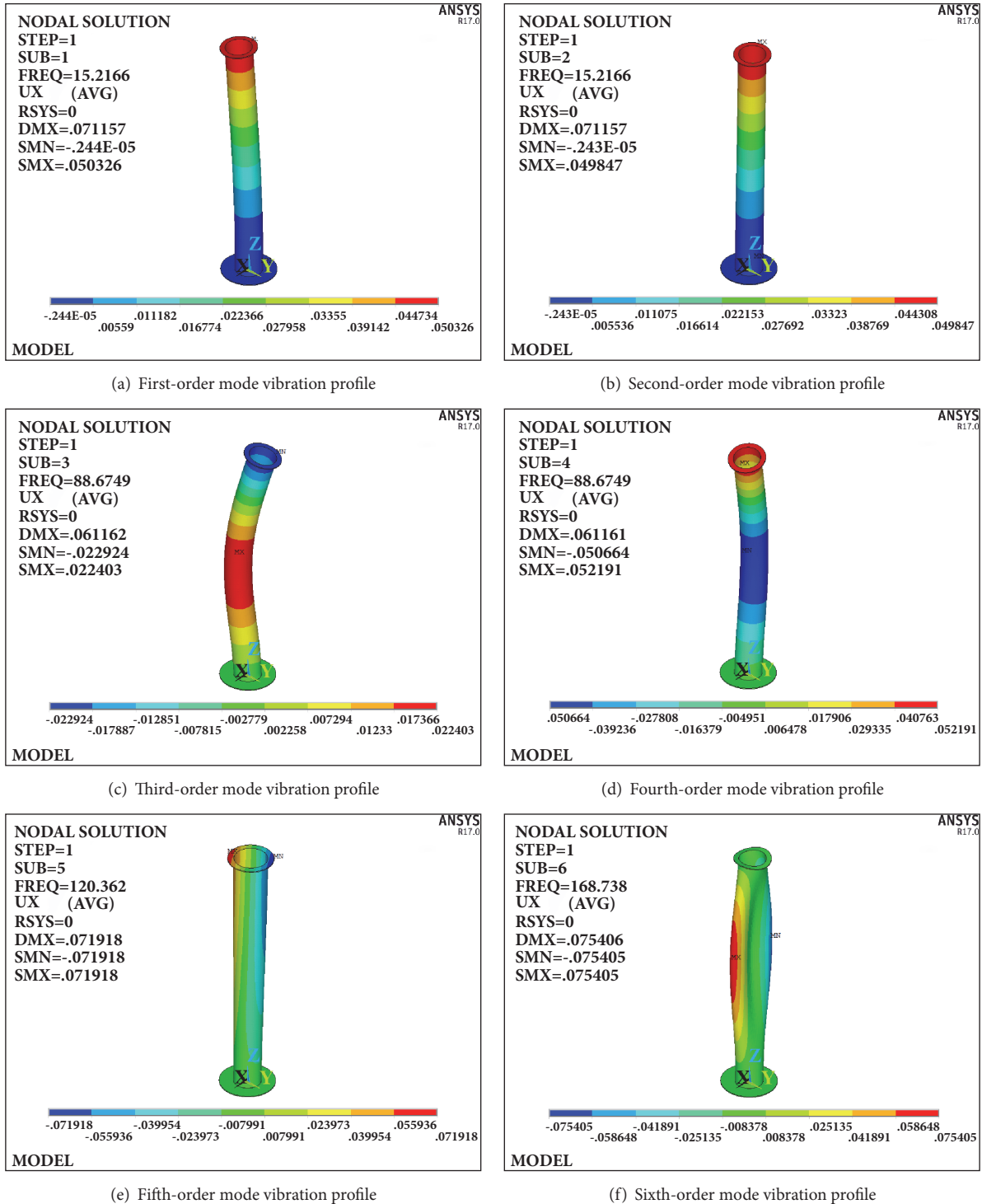


FIGURE 18: The first six-order mode vibration profile of tower.

that the design of wind turbine structure is reasonable. A prototype of LD-VAWT was designed and made. It was tested in a farm of Northeast Agricultural University of China which is shown in Figure 19.

Based on the observation of its operation situation for a period of time, the wind turbine can work safely and stably according to the design goal, which shows that the design scheme is practicable and proves that the ideas and methods

for LD-VAWT are correct. The paper provides references to analyze the structure of the LD-VAWT.

## 6. Conclusions

In order to explore a set of methods about designing and analyzing the structure of LD-VAWT, the paper took a small-scale LD-VAWT as an example and analyzes the static



FIGURE 19: Actual machine of wind turbine.

mechanical property and modal analysis by finite element method; the conclusions are as follows.

The corresponding contours of stress and deformation were obtained by using ANSYS to analyze the static mechanical property of main parts of wind turbine, which concludes that the structure of wind turbine meets the design requirements.

The first six-order mode vibration profiles of main parts were also obtained based on the modal analysis, which concludes that the resonance of each main part will not resonant during the operation.

The prototype LD-VAWT was made based on the analysis and simulation results in this study and operated steadily. The methods used in this study can be used as a reference for the static mechanical properties and modal analysis of vertical axis wind turbine.

## Conflicts of Interest

The authors declare that they have no conflicts of interest.

## Acknowledgments

This research is sponsored by the Project 2017MS02 supported by the Foundation of Key Laboratory of Wind Energy and Solar Energy Technology, Ministry of Education. The authors thank the supporter.

## References

- [1] Y. Li, Y. Zheng, S. Zhao et al., "A review on aerodynamic characteristics of straight-bladed vertical axis wind turbine," *Acta Aerodynamica Sinica*, vol. 35, no. 6, pp. 368–382, 2017.
- [2] G. Dai, Z. Xu, K. Huangfu, and Y.-J. Zhong, "Research progress in the vertical axis wind turbine," *Fluid Machinery*, vol. 38, no. 10, pp. 39–43, 2010.
- [3] Y. Li, J. Tang, K. Tagawa, and F. Feng, "Effect of frustum-shaped wind collection pattern to starting performance of VAWT," *Journal of Northeast Agricultural University*, vol. 47, no. 4, pp. 95–101, 2016.
- [4] Z.-C. Wu, *Research on Aerodynamic Characteristics of Vertical Axis Wind Turbine with Eccentric Rotor Structure*, Harbin, Northeast Agricultural University, 2017.
- [5] M. S. Hameed, S. K. Afaq, and F. Shahid, "Finite element analysis of a composite VAWT blade," *Ocean Engineering*, vol. 109, pp. 669–676, 2015.
- [6] L. Wang, A. Kolios, T. Nishino, P.-L. Delafin, and T. Bird, "Structural optimisation of vertical-axis wind turbine composite blades based on finite element analysis and genetic algorithm," *Composite Structures*, vol. 153, pp. 123–138, 2016.
- [7] T.-T. Zhang, H.-X. Wang, and Z.-B. Dai, "Research on vertical-axis wind turbines structure vibration characteristics," *East China Electric Power*, vol. 37, no. 3, pp. 452–455, 2009.
- [8] J.-Y. Wang, *Study of the Effect of Vortex Shedding on a 5 KW H-Type Vertical Axis Wind Turbine*, Harbin: Harbin Institute of Technology, 2016.
- [9] N. H. Abu-Hamdeh and K. H. Almitani, "Construction and numerical analysis of a collapsible vertical axis wind turbine," *Energy Conversion and Management*, vol. 151, pp. 400–413, 2017.
- [10] Y. Tang, Y. H. Wu, K. Zhang, J. Sun, and E. W. Song, "Finite element analysis of wind turbine lifting platform bridge structure," *Applied Mechanics and Materials*, vol. 687–691, pp. 398–401, 2014.
- [11] E. Verkinderen and B. Imam, "A simplified dynamic model for mast design of H-Darrieus vertical axis wind turbines (VAWTs)," *Engineering Structures*, vol. 100, pp. 564–576, 2015.
- [12] Z. Li and Y. Chen, "Dynamic research with drivetrain simulation and modal analysis of wind turbine gearbox," *Advanced Materials Research*, vol. 952, pp. 161–164, 2014.
- [13] I. Paraschivoiu, *Wind Turbine Design with Emphasis on Darrieus Concept*, Shanghai: Shanghai Scientific & Technical Publishers, 2013, translated by C. Li.
- [14] Y.-H. Zhu and Z.-H. Liu, "Structure and performance analysis for hybrid vertical axis wind turbines with lift and resistance leaves," *East China Electric Power*, vol. 36, no. 7, pp. 99–101, 2008.
- [15] F. Feng, Y. Li, L. Chen, W. Tian, and Y. Zhang, "A simulation and experimental research on aerodynamic characteristics of combined type vertical axis wind turbine," *Acta Energetica Sinica*, vol. 35, no. 5, pp. 855–860, 2014.
- [16] Q.-B. He, *Study on Calculation of Structure And Aerodynamic Characteristics for Vertical Axis Wind Turbine with Double-Layer Retractable Blades*, Harbin: Northeast Agricultural University, 2015.
- [17] K. Niklas, "Strength analysis of a large-size supporting structure for an offshore wind turbine," *Polish Maritime Research*, vol. 24, no. 1, pp. 156–165, 2017.
- [18] J.-F. Ji, Z.-Y. Deng, L. Jiang, and D.-G. Huang, "5kW masking the optimization design of the lift vertical axis wind turbine," *Journal of Engineering Thermal Physics*, vol. 33, no. 7, pp. 560–564, 2013.
- [19] W. Kou, B. Yuan, Q. Li, and L.-T. Fan, "The structural design of a type of vertical shaft wind generator," *Electrical and Electronic Engineering*, vol. 27, no. 5, pp. 25–28, 2011.
- [20] Z. Xu, Y.-L. Huo, Y. Chen, H.-W. Yang, and H.-F. Tan, "Optimum design and study on the properties of a new combined type vertical axis wind turbine," *Journal of Zhejiang University of Technology*, vol. 43, no. 3, pp. 261–264, 2015.
- [21] J.-J. Qu, M.-W. Xu, Z.-J. Li, and C. Zhi, "A kind of lift and drag hybrid vertical axis wind turbine," *Renewable Energy Resources*, vol. 28, no. 1, pp. 101–104, 2010.

- [22] K. Kong, X. L. Zhou, and M.-Z. Cheng, "Structural modelling analysis and testing of wind turbine rotor blade," *Mechanical Electrical Engineering Technology*, vol. 47, no. 5, pp. 45–48, 2018.
- [23] GB/T 29494-2013 Small vertical axis wind turbines [S].
- [24] GB/T 13981- Design general requirements for small wind turbine[S].
- [25] X. Sun, Y. Chen, Y. Cao, G. Wu, Z. Zheng, and D. Huang, "Research on the aerodynamic characteristics of a lift drag hybrid vertical axis wind turbine," *Advances in Mechanical Engineering*, vol. 8, no. 1, 2016.
- [26] X. Song and J.-X. Dai, "Mechanical modeling and ANSYS simulation analysis of horizontally axial wind turbine tower," *Journal of Gansu Sciences*, vol. 23, no. 1, pp. 91–95, 2011.

## Research Article

# Research on Aerodynamic Characteristics of Straight-Bladed Vertical Axis Wind Turbine with S Series Airfoils

Fang Feng <sup>1,2</sup>, Shouyang Zhao,<sup>3</sup> Chunming Qu,<sup>3</sup> Yuedi Bai,<sup>3</sup>  
Yuliang Zhang,<sup>1</sup> and Yan Li <sup>2,3</sup>

<sup>1</sup>College of Science, Northeast Agricultural University, Harbin 150030, China

<sup>2</sup>Heilongjiang Provincial Key Laboratory of Technology and Equipment for Utilization of Agricultural Renewable Resources in Cold Region, Harbin 150030, China

<sup>3</sup>College of Engineering, Northeast Agricultural University, Harbin 150030, China

Correspondence should be addressed to Fang Feng; [fengfang@neau.edu.cn](mailto:fengfang@neau.edu.cn) and Yan Li; [liyanneau@163.com](mailto:liyanneau@163.com)

Received 27 October 2017; Revised 12 January 2018; Accepted 13 February 2018; Published 16 May 2018

Academic Editor: Ahmad Sedaghat

Copyright © 2018 Fang Feng et al. This is an open access article distributed under the Creative Commons Attribution License, which permits unrestricted use, distribution, and reproduction in any medium, provided the original work is properly cited.

**Background.** In order to investigate the effect of aerodynamic characteristics of S series airfoils on the straight-bladed vertical axis wind turbine (SB-VAWT), numerical simulations and wind tunnel experiments were carried out using a small SB-VAWT model with three kinds of blade airfoils, which are asymmetric airfoil S809, symmetric airfoil S1046, and NACA0018 used for performance comparison among S series. The aerodynamics characteristics researched in this study included static torque coefficient, out power coefficient, and rotational speed performance. The flow fields of these three kinds of blade under static and dynamic conditions were also simulated and analyzed to explain the mechanism effect of aerodynamic performance. According to the results, the SB-VAWT with airfoil S1046 has better dynamic aerodynamic characteristics than other two airfoils, while the SB-VAWT with airfoil S809 is better in terms of the static characteristics. As the most suitable airfoil for SB-VAWT, the S series airfoil is worth researching deeply.

## 1. Introduction

In recent years, as one of vertical axis wind turbines (VAWT), the straight-bladed vertical axis wind turbine (SB-VAWT) has developed rapidly and attracted attention of scientists due to its advantages such as wind direction independence, simple structure, and unique shape [1]. The selection of the blade airfoil was found one of the main factors which has influenced the output characteristics of SB-VAWT. Normally, the airfoils of horizontal axis wind turbine (HAWT) are NACA series airfoils, SERL series airfoils studied by America, S8xx series airfoils, FFA-W series airfoils manufactured by FOI of Sweden, RisΦ-A-XXX series airfoils developed by Denmark, DU series airfoils developed by Delft University, and so on [2]. Common VAWT airfoils refer to NACA series, among which airfoil l0018 is widely used in SB-VAWT due to its better wind energy utilization coefficients. Researchers have great interests in the airfoils comparative analysis and selection. In 2008, Canadian researchers found that airfoils which are suitable for HAWT are not necessarily suitable for

VAWT [3]. Zhang et al. analyzed six different kinds of airfoils including NACA, FFA, and FX series and found that the maximum lift coefficient and the maximum lift-drag ratio of FFA series airfoils which are more suitable for SB-VAWT working environment are better than those of the NACA series airfoils [4]. Liao et al. researched the aerodynamic performance of small SB-VAWT based on different airfoils [5]. In 2012, Mohamed analyzed the performance investigation of VAWT using new airfoil shapes [6]. Xu et al. used nonsymmetrical airfoils DU06-W-200 as the research object to investigate the influence of installation on the performance of SB-VAWT [7]. Xu et al. analyzed the aerodynamic performance of thickened DU series airfoils [8]. Yang and Li studied an improved VAWT airfoil on the basis of airfoil 4418 of NACA series [9]. In 2016, Jia et al. studied three kinds of DU series airfoils including DU25, DU30, and DU35 and found the influence of relative thickness on aerodynamic performance [10].

Based on the past researches mentioned above, it can be found that the researches on SB-VAWT blade airfoils mainly focus on NACA series, DU series, FFA series, and

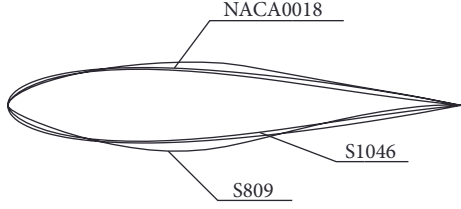


FIGURE 1: Three kinds of airfoil.

TABLE 1: Main features of the analyzed rotor.

Denomination	Value
Blade number ( $N$ )	3
Blade shape	Straight
Blades airfoil (attended)	NACA0018, S809, S1046
Height ( $H$ ) [m]	0.5
Radius ( $R$ ) [m]	0.4
Chord ( $c$ ) [m]	0.125
Solidity ( $\sigma$ )	0.149
Texture	FRP

FX series. However, there is a lack of research on S series airfoils which is widely used in HAWT. Therefore, in this study, two typical kinds of S series including S1046 and S809 were selected to investigate whether this kind of blade airfoil is suitable for SB-VAWT or not. NACA0018 airfoil was also selected for the comparison study. The aerodynamics characteristics researched in this study included static starting torque coefficient, out power coefficient, and rotational speed performance. The flow fields of three kinds of blade under both static and dynamic conditions were also simulated and analyzed. This study can provide a good reference for the blade airfoil research on SB-VAWT.

## 2. Model Design

**2.1. Airfoils.** The cross sections of airfoils NACA0018, S809, and S1046 are shown in Figure 1. NACA0018 and S1046 are symmetrical airfoils, and S809 is an asymmetric airfoil. As is shown in the figure, the leading edge of airfoil S809 is thinner than the other two. However, the middle of airfoil S809 is thicker than the other two. NACA0018 and S1046 are symmetrical airfoils. Both the leading edge and the trailing edge of airfoil NACA0018 are thicker than those of airfoil S1046 and the trailing edge of airfoil S1046 is the inner convergence.

**2.2. Main Structural Parameters.** According to the theory of hydrodynamics and the design method of VAWT, a kind of small blade SB-VAWT is designed [11–13]. For the experimental validation, the geometry considered in the study is summarized in Table 1 based on the size of experimental segment (1 m × 1 m) of the wind tunnel in the laboratory. The blade is rotating counterclockwise; the angle between blade beam and axis  $Y$  is azimuth angle  $\theta$ . The azimuth angle is shown in Figure 2.

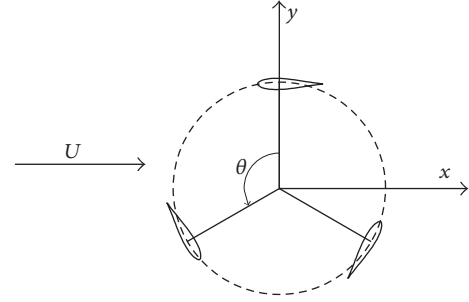


FIGURE 2: Structural parameters of wind turbine.

## 3. Research Methods

In order to explore the aerodynamic characteristics of SB-VAWT with S series airfoils, numerical simulations and wind tunnel experiments were used in this paper.

**3.1. Numerical Simulation.** A finite volume CFD solver by ANSYS was used in this work, implementing Reynolds averaged Navier-Stokes equations. Because the cross sections of wind turbine blade are exactly the same, this study adopts two-dimensional model numerical simulation method. The calculation of the structure is simplified. The turbulence model based on the pressure solver is the  $k$ - $\epsilon$  RNG model. The transport equations for  $k$  and  $\epsilon$  are shown in (1). The pressure velocity coupling is the SIMPLEC algorithm, and the flow is unsteady. The turbulent kinetic energy dissipation rate epsilon,  $K$  equation, and the momentum equation are the two-order upwind scheme.

$$\begin{aligned}
 \frac{\partial(\rho k)}{\partial t} + \frac{\partial(\rho k u_i)}{\partial x_i} &= \frac{\partial}{\partial x} \left( \alpha_k \mu_{\text{eff}} \frac{\partial k}{\partial x_j} \right) + G_k + G_b - \rho \epsilon \\
 &\quad - Y_M + S_k, \\
 \frac{\partial(\rho \epsilon)}{\partial t} + \frac{\partial(\rho \epsilon u_i)}{\partial x_i} &= \frac{\partial}{\partial x_j} \left( \alpha_\epsilon \mu_{\text{eff}} \frac{\partial \epsilon}{\partial x_j} \right) \\
 &\quad + C_{1\epsilon} \frac{\epsilon}{k} (G_k + C_{3\epsilon} G_b) \\
 &\quad - G_{2\epsilon} \rho \frac{\epsilon^2}{k} - R.
 \end{aligned} \tag{1}$$

The calculation area of the outside wind turbine is a rectangle as is shown in Figure 3, which is 10 times the width and 15 times the length of the radius of wind turbine. The flow is relatively stable before the wind turbine, and after the wind turbine, the flow field changes a lot, so the position of the wind turbine in the computation domain is far from the exit boundary, thus helping to observe the variation of the flow field behind the wind turbine. The flow from the left entry of the graph is the velocity inlet, with the calculation wind speed being 10 m/s, the right side being the pressure outlet, the rectangular upper and lower sides being stationary wall surfaces, and the blade wall moving on the wall surface. In order to guarantee the accuracy of the calculated results and

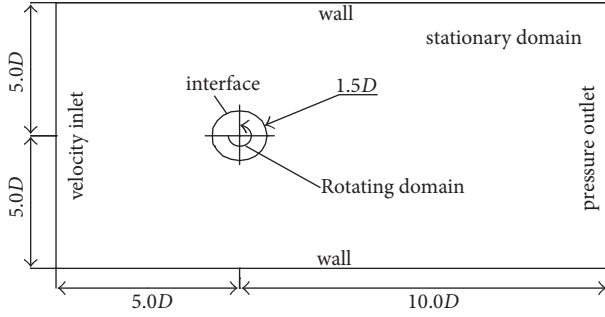


FIGURE 3: Computational region diagram and boundary conditions.

TABLE 2: Component of the experimental equipment.

Equipment	Function	Precision
Wind tunnel	Provide a stable source of wind	3%
Model of wind turbine	Experimental model	
Torque sensor	Acquisition data	$\pm 0.2\%$
Torque analyzer	Display the data	
Motor	Provide load, stable model speed	3%
Power supply	Control motor speed	
Computer	Process the data	

control the appropriate calculation time, the grid of VAWT was refined. The grid settings are shown in Figure 4.

In order to prove the independence of the mesh number, the static torque coefficient of wind turbine was studied when the azimuth is 5 degrees. Five different mesh numbers are 73765, 110647, 156971, 200432, and 248956, respectively. The fluid computational domain model is chosen for trial calculation. It clearly appears in Figure 5 that using RNG  $k-\epsilon$  as the turbulence model for the model meshed by ANSYS gives unstable solution over a wide range of a number of nodes. When the number of mesh increases from 156971 to 248956, the numerical results are not much different. Taken into consideration, the mesh number selected in this study is 156971.

**3.2. Wind Tunnel Experiment.** In order to verify the influence of eccentricity on the power characteristics of the SB-VAWT, the experiments were conducted at Northeast Agricultural University using the large-scale low-speed opening wind tunnel which is 9.1 m long and 2.3 m wide, its exit size being 1 m  $\times$  1 m wide, and the wind speed being constant at the exit from 1–20 m/s. The wind tunnel experiment system consisted of a low-speed wind tunnel, an experimental model, a speed torque tester, an induction motor, a frequency converter, and a computer. The system diagrams are shown in Figures 6 and 7 and the function of them is shown in Table 2.

In the experiment, the height of wind turbine center is consistent with that of the wind tunnel exit center. The wind turbine is driven by an induction motor, with its speed controlled by a frequency converter. The speed and torque are detected by the speed torque sensor. The speed torque sensor measuring range is 5 N·m, the accuracy is  $\pm 0.2\%$ , and the original data sampling interval is 0.1 s. The wind generated in the wind tunnel pushes the blades and applies rotation power

to rotor axis, the rotational power can be transferred to the torque meter, and the rotational speed is measured in real time by the topic sensor. When the experiment is carried out, the signal is converted to the voltage level which is used to acquire the power of the wind turbine using a data program.

## 4. Results and Discussion

The aerodynamic characteristics of the wind turbine investigated in this study are mainly output power coefficients at different tip speed ratio and static torque coefficients at different azimuth angles for SB-VAWT. The definitions of power coefficient, torque coefficient, and tip speed ratio are shown in the following equation:

$$C_P = \frac{P}{(1/2) \rho A U^3},$$

$$C_M = \frac{M}{(1/2) \rho A U^2 R}, \quad (2)$$

$$\lambda = \frac{V}{U} = \frac{\omega R}{U},$$

where  $C_P$  is the power coefficient,  $P$  is the power absorbed by a wind turbine,  $\rho$  is air density,  $A$  is the swept area of the wind turbine relative to the current,  $U$  is inflow velocity,  $C_M$  is the torque coefficient,  $M$  is the torque absorbed by a wind turbine,  $R$  is the radius of wind turbine,  $\lambda$  is the tip speed ratio,  $V$  is the linear velocity of wind turbine, and  $\omega$  is the rotation speed of wind turbine.

### 4.1. Dynamic Characteristics

**4.1.1. Power Coefficient.** In this paper, numerical simulations and wind tunnel tests were carried out, respectively, to reflect the output characteristics of the SB-VAWT with different airfoils. Figure 8 shows that power coefficients vary with the tip speed ratio when wind speed is 10 m/s. Figure 9 shows the maximum power coefficients of the three kinds of SB-VAWT at different wind speeds.

As shown in Figure 8, for simulation results, when  $\lambda$  is in the range from 0.2 to 0.8, the power coefficients are slowly increasing and the growth rate is low. When  $\lambda$  is in the range from 0.8 to 1.8, the power coefficients are obviously increasing, and the value of power coefficients reaches the maximum when  $\lambda$  is up to 1.8. The power coefficient of SB-VAWT with airfoil S809 is the lowest among the three airfoils. When  $\lambda$  is in the range from 0.2 to 1.0, the power coefficients of the SB-VAWT with airfoil S1046 are much close to NACA0018. When the tip speed ratio is in the range from 1.0 to 2.0, the power coefficient of airfoil S1046 is better than those of S809 and NACA0018. The wind tunnel test results and numerical results are in good agreement with the overall trend, except a bit difference in the value. The reasons for the difference between numerical and experimental results are mainly as below: first, there are no shafts, beams, flanges, and other components in the normal numerical simulation model, and when these factors are taken into account in the experiment, the experimental error cannot be ignored. The

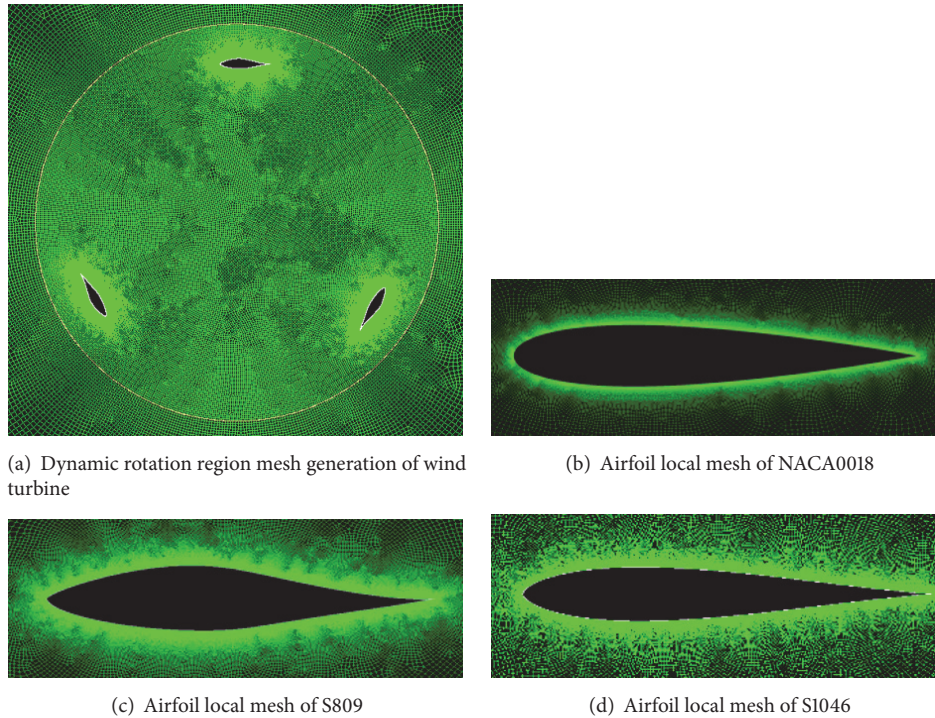


FIGURE 4: Grid mesh of computing model.

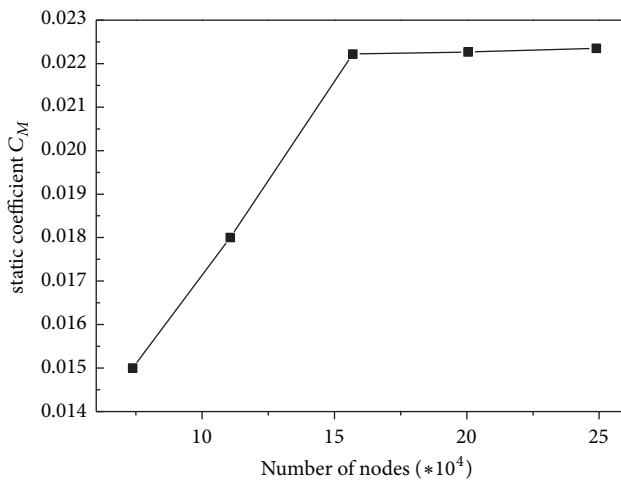


FIGURE 5: Grid independent verification.

second is that the fluid field of numerical calculation is large, and the range of the experimental wind field is relatively small, which will produce certain errors.

As can be seen from Figure 9, the maximum power coefficient of SB-VAWT increases with the increasing of wind speed. Under the same wind speed, the order of the power coefficient from high to low is S1046, NACA0018, and S809. When wind speed is 10 m/s, the maximum power coefficient of airfoil S1046 wind turbine is 0.32, which is 6.7% higher than that of NACA0018 and 7.1% higher than that of S809. Therefore, the results of Figures 8 and 9 show that, under the experimental conditions, the output characteristics of the

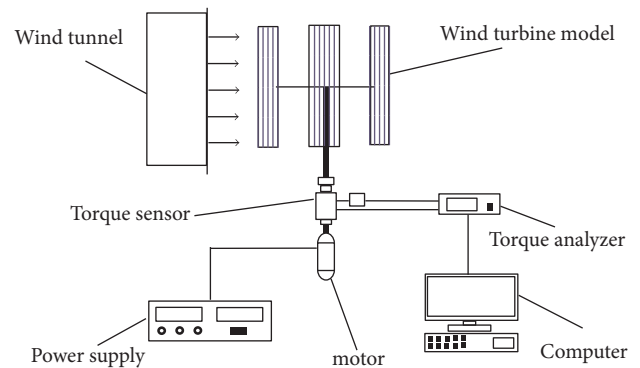


FIGURE 6: Schematic diagram of experimental system.

S1046 airfoil SB-VAWT are better than those of the other two airfoils.

**4.1.2. Dynamic Flow Field.** In order to further analyze the influence of blade airfoil selection on the output characteristics for SB-VAWT, the torque characteristics and the flow field of the blade were compared and analyzed.

It can be seen from Figure 8 that under the experiment condition of  $U = 10$  m/s the power coefficients of the three airfoils wind turbine reach the maximum value when  $C_P$  is up to 1.8 according to the results listed above. The power characteristics of the S1046 airfoil wind turbine are better than the other two. Under the experimental conditions, the torque coefficients of SB-VAWT are different from the azimuth angles when the wind turbine rotates in one circle.



FIGURE 7: Physical diagram of experimental system.

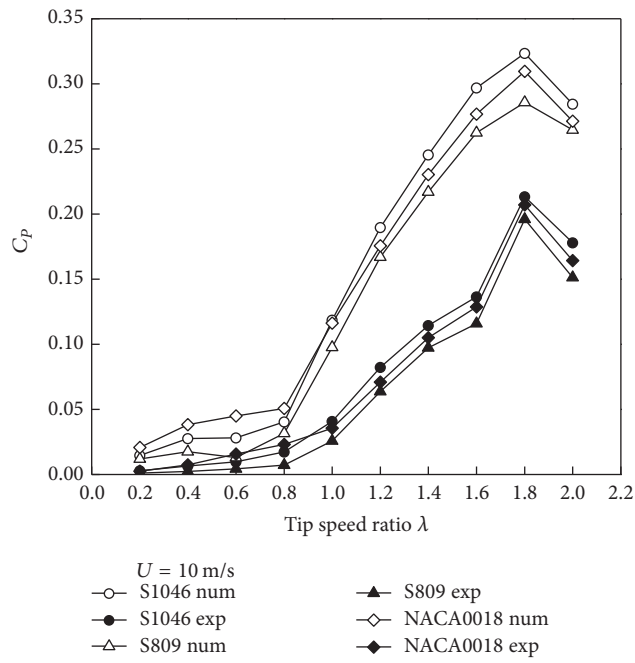


FIGURE 8: Power coefficient.

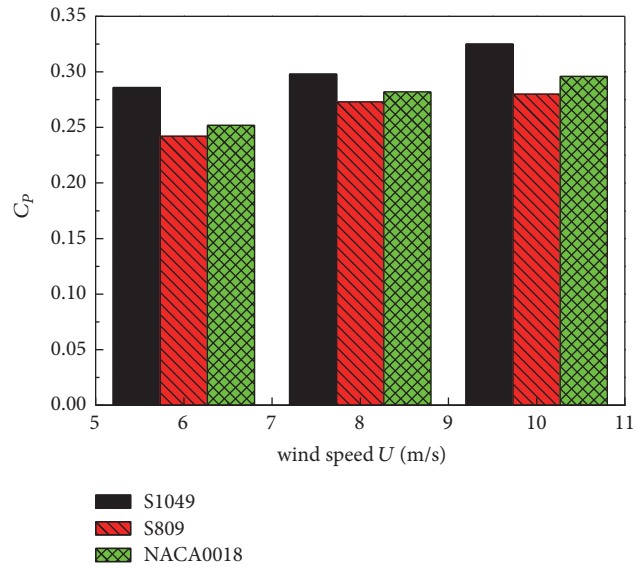


FIGURE 9: Maximum power coefficient.

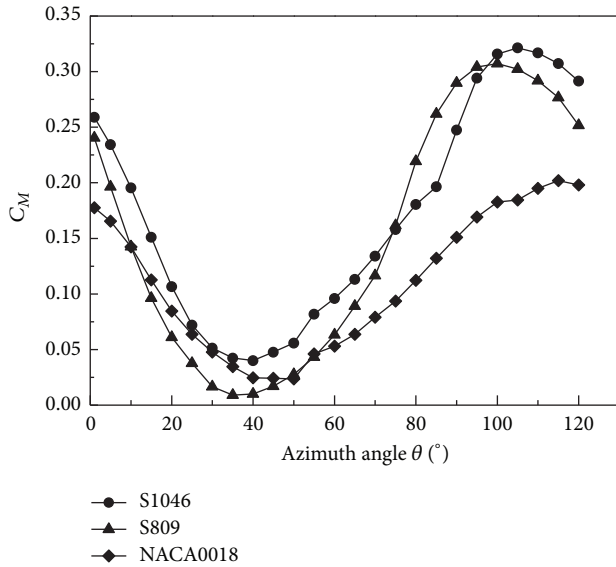


FIGURE 10: Torque coefficient at different azimuth angle ( $\lambda = 1.8$ ).

Figure 10 shows the curves of the torque coefficients at different azimuth angles when  $\lambda$  is 1.8. As we can see from Figure 10, the torque coefficients of the SB-VAWT with three airfoils have a peak value and a valley value in a circle. Airfoils S1046 and S809 have the lowest torque coefficient at 35 degrees, and the airfoil NACA0018 has the lowest torque coefficient at 45 degrees. The maximum torque coefficients of the SB-VAWT with airfoils S1046 and S809 are near 100 degrees, and the airfoil NACA0018 is near 115 degrees. In conclusion, the torque characteristics of SB-VAWT with S series airfoils are better than NACA series airfoils, the average value of the torque coefficients of airfoil S1046 is the largest, and the output characteristics is the best.

In order to analyze the reasons for the difference in output aerodynamic characteristics of three airfoils SB-VAWT in detail, velocity and pressure distribution flow charts of the blades with three different airfoils are compared when  $\lambda$  is 1.8 and the azimuth angles of 35 and 100 degrees are selected. The influence of airfoils on the flow field of the blade is shown in Figures 11 and 12.

As is shown in Figure 11, for blade, the SB-VAWTs with airfoils S1046 and NACA0018 have a small range of high pressure zone on the windward side of the leading edge. In comparison, the high pressure zone of SB-VAWT with airfoil S809 is larger and there is a wide range of negative pressure zone on the ventral of the blade. The difference on the pressure between the ventral and the back of the blade could generate more aerodynamic forces, thus driving the forward rotation of the wind turbine. Furthermore, the SB-VAWT with airfoil NACA0018 produces a large vortex at the back of the blade, which leads to the loss of energy and lower output characteristics. For blade (b), a large zone of negative pressure is found in the ventral of blades, where the low value area of S809 is more obvious. Therefore, it generates lower power coefficient. For blade (c), three wind turbines with different airfoils all have vortex in the ventral side, among which NACA0018 is the largest, and the energy loss is also greater

than those of other two turbines. In conclusion, among the SB-VAWTs with three different airfoils, the performance of airfoil S1046 is better in the aspects of the pressure difference between the ventral and back of the blade and the energy utilization, and the torque coefficient is slightly higher than the other two airfoils at 35 degrees.

As can be seen from Figure 12, when the azimuth angle is 100 degrees, the variation of the flow field of the blade is obvious. For blade (a), SB-VAWT with three kinds of airfoils has large pressure zone at the leading edge of the blade, and the vortex appears on the ventral, among which NACA0018 has the largest pressure, causing energy loss, producing a great influence on the output characteristics and leading to the smallest torque coefficient. For blade (b), both NACA0018 and S1046 (b) have vortex. However, the blade of airfoil S809 does not appear. The pressure difference between the ventral and the back of the blade is obvious, so there is a great contribution to the output characteristics of airfoil S809. For blade (c), the pressure difference of three kinds of airfoils is not obvious, so the contribution to the output characteristics is small. Comparing with S809 and S1046, the high pressure area of the blade of S809 is smaller, which causes smaller aerodynamic force, so that the torque is slightly smaller.

**4.1.3. Rotational Speed Performance.** In order to study the rotational speed characteristics and the starting characteristics of SB-VAWT with different airfoils, the change of rotational speed under different wind speeds was investigated by wind tunnel experiments, and the tested wind speed is 6–10 m/s with the interval of 1 m/s. The steady speed of the SB-VAWT and the time required to reach the steady speed were tested at each wind speed. The speed change curve with different wind speeds is shown in Figure 13. When the wind speed is under 7 m/s, the SB-VAWT with airfoil NACA0018 cannot start, so the wind speed change curves are not given.

As can be seen from Figure 13, the steady speed of three different airfoils wind turbines is on the rise with the increase of wind speed, and the time required to reach a steady rotating speed is increasing gradually. When the wind speed is certain, the steady speed from high to low is followed by S1046, NACA0018, and S809. The time required to reach a steady speed from long to short is followed by S1046, NACA0018, and S809. When the wind speed is 10 m/s, three different wind turbine airfoils steady speeds are the highest. For airfoil S1046, the steady rotational speed is 140 r/min, for NACA0018 is 120 r/min, and for S809 is 45 r/min. When the wind speed is less than or equal to 7 m/s, the SB-VAWT with airfoil NACA0018 cannot start itself, which shows that the starting performance is not good. This is one of the important reasons which restricts the development of current NACA series of SB-VAWT. This problem can be overcome to some extent by using S series airfoils.

## 4.2. Static Characteristics

**4.2.1. Static Torque Coefficient.** In order to further study different influence of blade on the starting characteristics of SB-VAWT with different airfoils, the static torque of SB-VAWT at different wind speeds was investigated by numerical

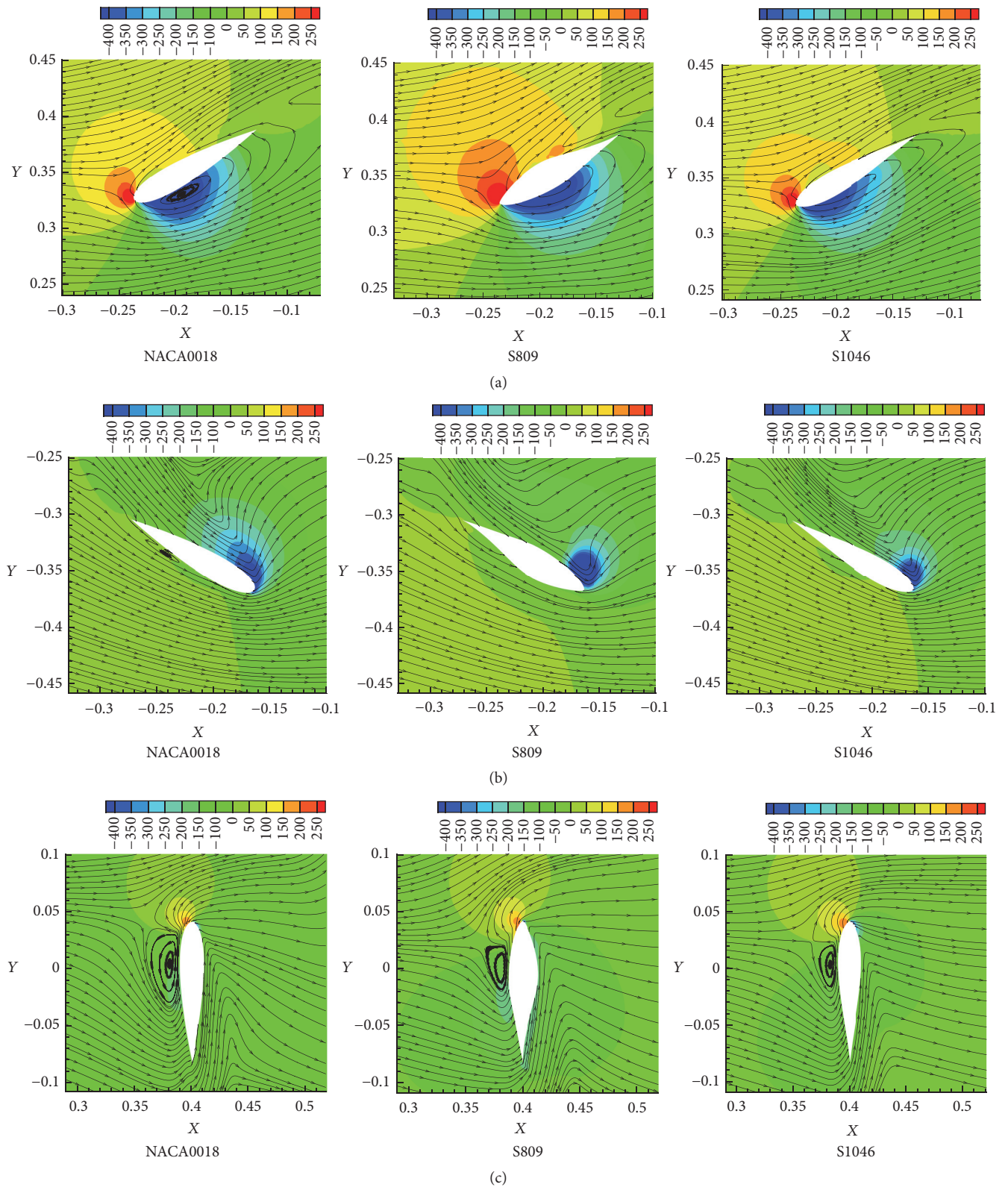


FIGURE 11: Flow fields around blade with different airfoils ( $\theta = 35^\circ$ ).

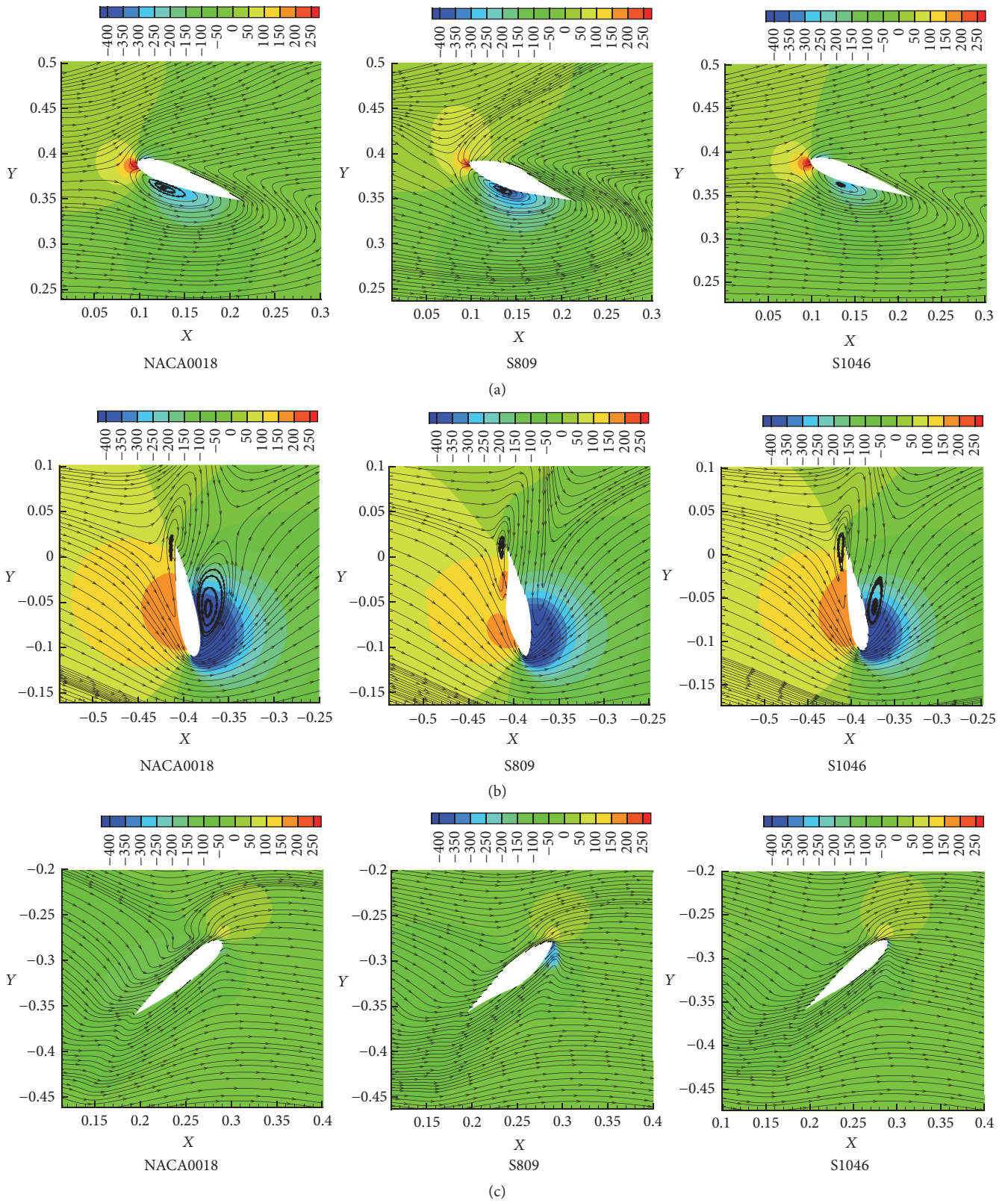


FIGURE 12: Flow fields around blade with different airfoils ( $\theta = 100^\circ$ ).

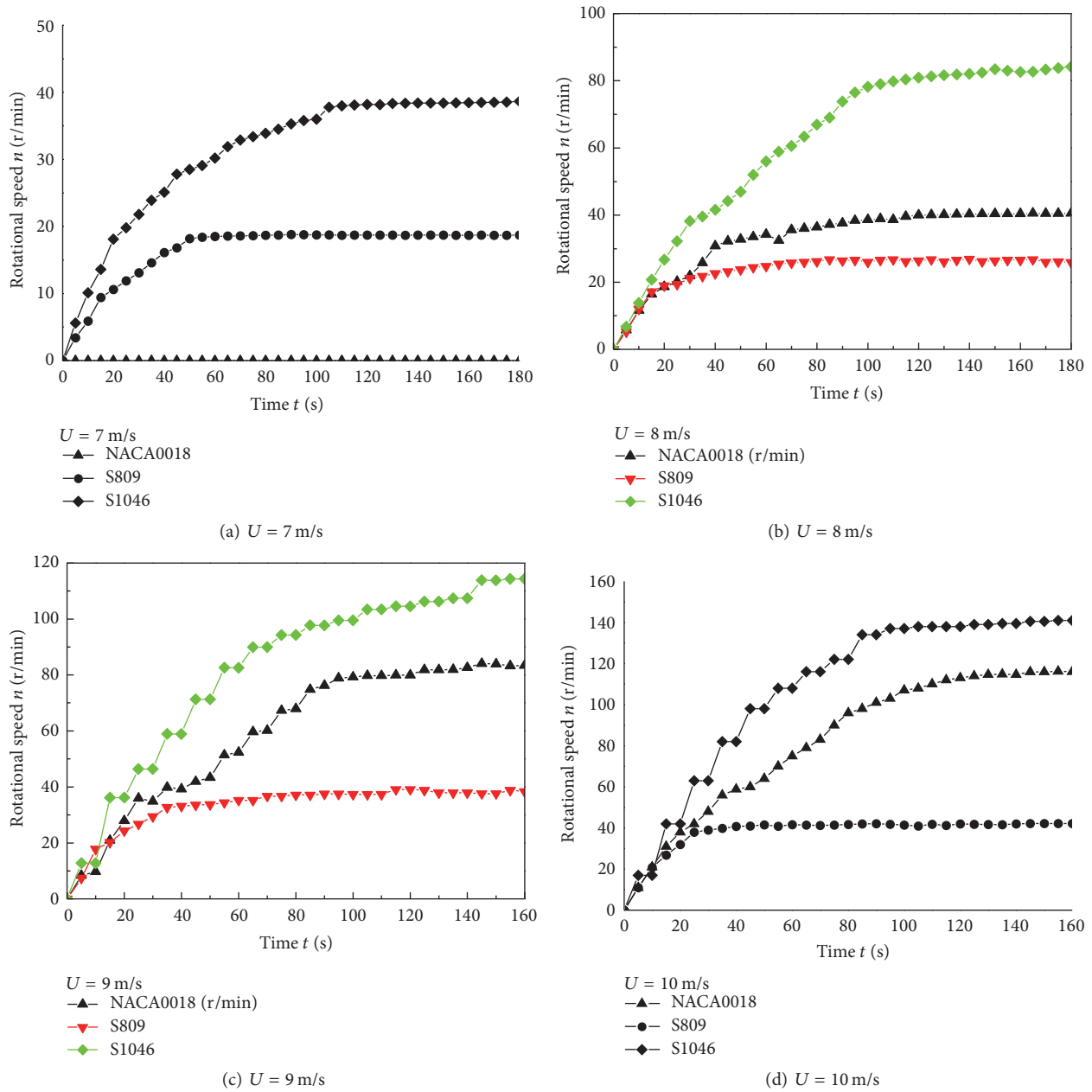


FIGURE 13: Rotational speed under different wind speeds.

simulation and wind tunnel experiments. Figure 14 shows the simulation and tests results of the curves of static torque coefficients ( $C_{ts}$ ) change with the azimuth angles when the wind speed is 10 m/s.

As can be seen from Figure 14, concerning simulation results, the torque coefficient of SB-VAWT with three different airfoils in a rotation period namely 0 to 120 degrees shows two peaks and a trough. The value of the static torque coefficient reaches the maximum when the azimuth angle is 15 degrees, the static torque coefficient of SB-VAWT with airfoil S809 is 0.062, airfoil NACA0018 is 0.054, and airfoil S1046 is 0.049. When the azimuth angle is 45 degrees, the minimum value reaches at this moment, and the static torque coefficient of airfoil S809 wind turbine is  $-0.0075$ , airfoil

NACA0018 is  $-0.0014$ , and airfoil S1046 is  $-0.0091$ . The average static torque coefficient of SB-VAWT with airfoil S809 is 0.032, the highest among the three airfoils. For experimental results, the results of wind tunnel experiments and numerical simulations have good consistency in the overall trend except being slightly lower in value, because in the process of torque transmission, there will be some friction loss between the flange and the beam, and the influence of the experimental error. In general, the asymmetric airfoil S809 has bigger static torque coefficients comparing with the other two kinds of symmetric airfoils.

4.2.2. *Static Flow Field.* In order to analyze the reason of the difference of starting characteristics in SB-VAWT with

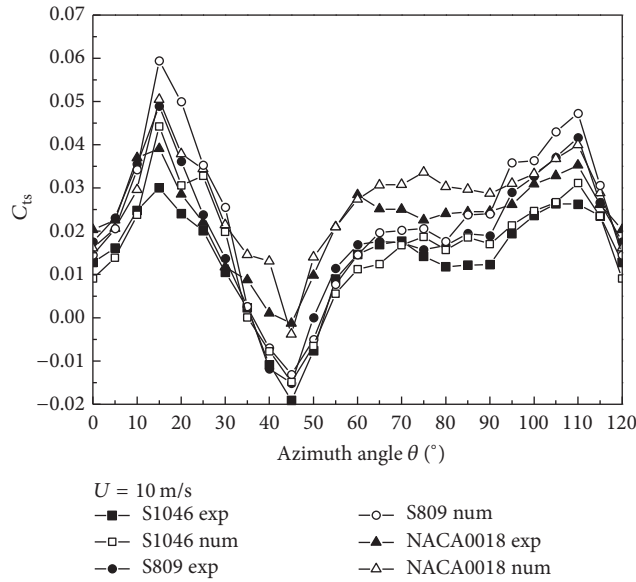


FIGURE 14: Static torque coefficients ( $U = 10 \text{ m/s}$ ).

three kinds of airfoils in detail, we selected streamlines and pressure distribution of three kinds of airfoil wind turbine at the azimuth angle of 15 and 45 degrees which are shown in Figures 15 and 16. The influence of airfoils on the flow fields of the blade was analyzed.

As can be seen in Figure 15, for blade (a), the force acting on the blades of the three airfoils is mainly at the leading edge. The negative pressure zone is found at the ventral of the blade, while the positive pressure zone is concentrated at the leading edge of the windward point. The aerodynamic force of the pressure difference causes the wind turbine to rotate counterclockwise. At the same time, the vortex appears at the trailing edge of airfoils S809 and S1046, which makes a certain energy loss on the upper blade. For blade (b), the trailing edge of the blade of the three airfoils is windward; the positive pressure zone is about 1/2 of the blade size; the back of the blade generates low pressure area; the pressure difference is more obvious than the upper blade; the aerodynamic force is greater, which is the main reason for starting coefficients of the SB-VAWT under this angle. The back of the three airfoils produces varying degrees of vortex, which also results in energy loss. The negative pressure zone of the blade in airfoil S1046 is larger than those of S809 and NACA0018, but its aerodynamic force is relatively small, which is an important coefficient for a minimum starting torque at 15 degrees. For blade (c), the positive pressure zone of three kinds of airfoil appears at the trailing edge of the blade, and the pressure difference is small, so the aerodynamic force is slightly smaller. In general, when the azimuth angle is 15 degrees, the high pressure area of non-symmetrical airfoil S809 is bigger than those of the other two kinds of airfoils. The aerodynamic force is relatively larger, and the starting torque is bigger, so the starting performance is better than those of the other two kinds of SB-VAWT.

As can be seen in Figure 16, for blade (a), three airfoils have a large positive pressure area at the trailing edge of the blade, while the negative pressure zone which generates

from the ventral of airfoil has obvious difference. The negative pressure zone around airfoil S809 accounts for 2/3 of the leeward side which results in great vortex and the energy loss is larger. For blade (b), the flow field of the three airfoils is basically the same. The pressure difference between the windward and leeward surfaces of the trailing edge is found, but the torque is small because of the aerodynamic position. For blade (c), when the positive pressure area is larger, the leeward vortex appears on the different positions of the three airfoils. The vortex appearing in the airfoil NACA0018 is smaller comparing with the other two airfoils. We found that the vortex range of the ventral side of blade S1046 is the largest and the energy loss is the largest, so the torque coefficient is the lowest at this azimuth angle. Overall, when the azimuth angle is 45 degrees, the pressure difference between ventral and the back of the three airfoils is small. The aerodynamic force is small so that the starting torque is small, which leads to the appearance of trough.

## 5. Conclusions

The main conclusions obtained under the condition of this study are as follows:

- (1) For dynamic characteristics, the power coefficient of the wind turbine model with airfoil S1046 is higher than those of the model with S809 and NACA0018 airfoils. Furthermore, the rotational speed performance of the test model with airfoil S1046 is also better than the other two kinds of airfoils.
- (2) For static characteristics, the static torque coefficient of SB-VAWT with airfoil S809 is higher than the S1046 and NACA0018. The asymmetry of the blade allows the turbine to obtain the forward torque that causes the turbine to rotate under the wide azimuth angle. Therefore, it can be said that the S series airfoils can

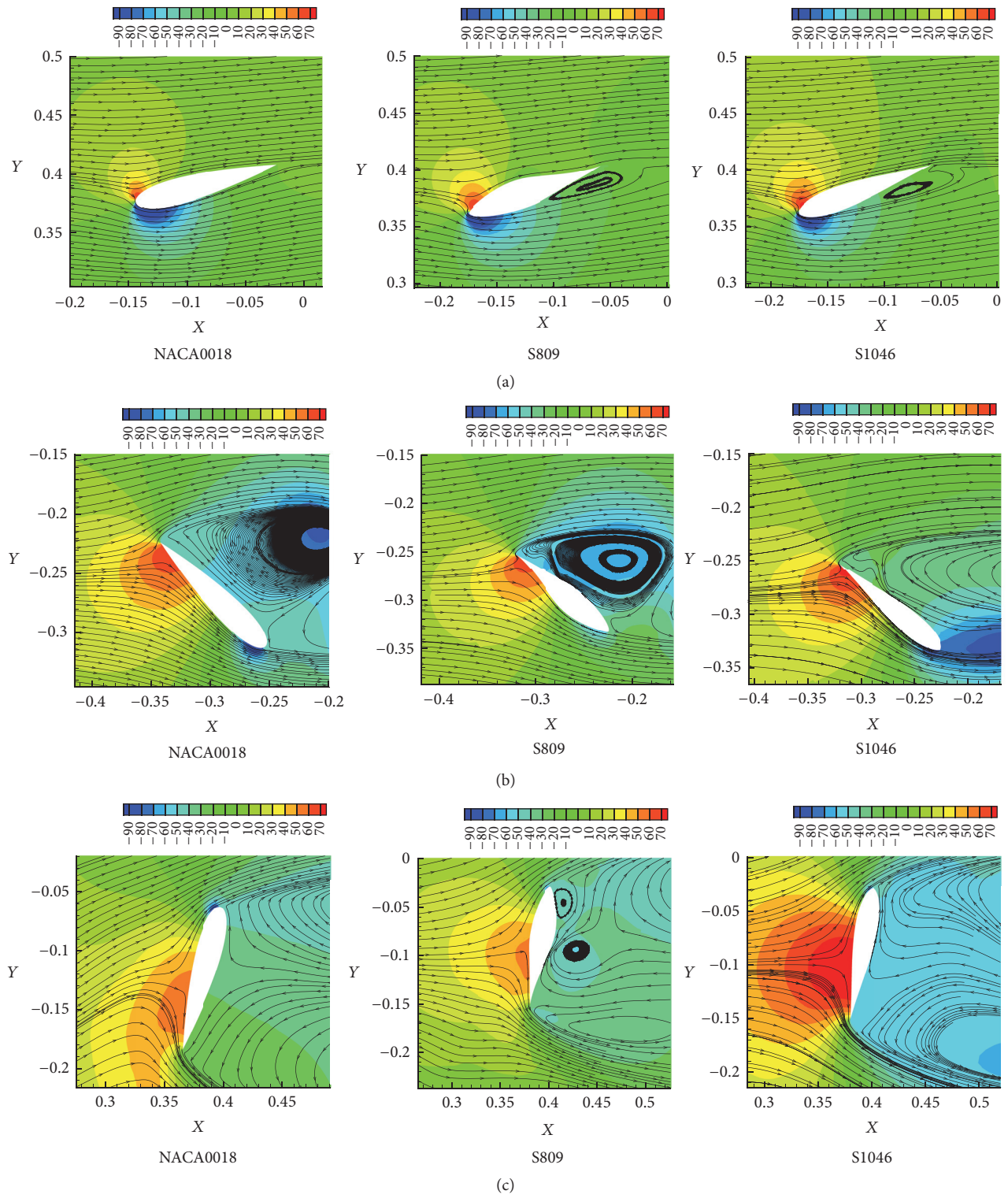


FIGURE 15: Flow fields around blade with different airfoils.

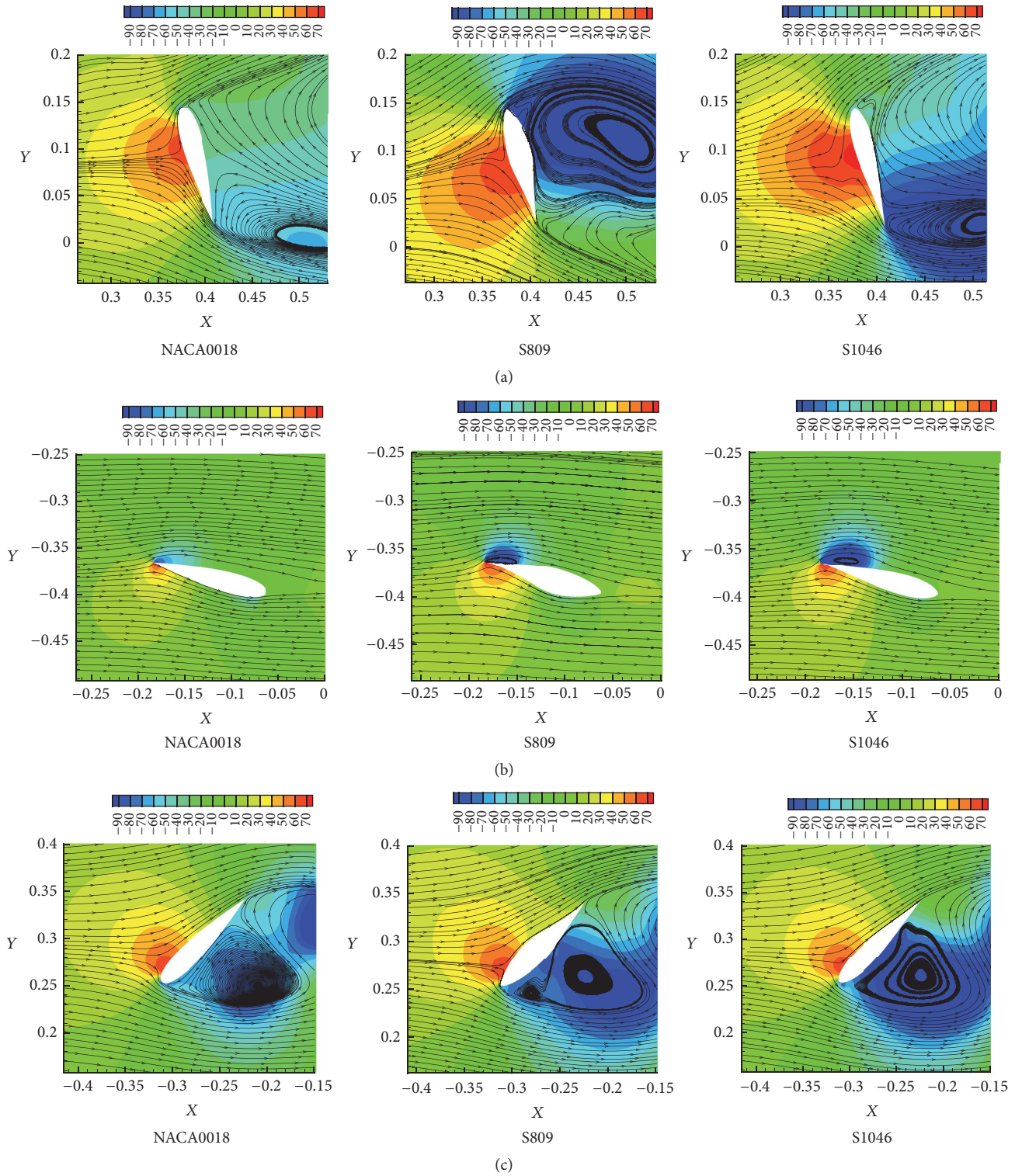


FIGURE 16: Flow fields around blade with different airfoils ( $\theta = 45^\circ$ ).

be used for SB-VAWT and as the most suitable airfoil for SB-VAWT, the S series airfoil is worth researching deeply.

## Conflicts of Interest

The authors declare that they have no conflicts of interest.

## Acknowledgments

This research is sponsored by the Project 51576037 supported by National Natural Science Foundation of China (NSFC) and Project 12541012 supported by Science and Technology Research Project of Heilongjiang Provincial Department of Education. The authors give thanks to their supporters.

## References

- [1] Y. Li, Y. Zheng, S. Zhao et al., "A review on aerodynamic characteristics of straight-bladed vertical axis wind turbine," *Acta Aerodynamica Sinica*, vol. 35, no. 6, pp. 368–382, 2017.
- [2] P. Chen, M.-Y. Du, and J.-P. Liu, "Development status and key aerodynamic problems of wind turbine dedicated airfoils," *Power System and Clean Energy*, vol. 25, no. 2, pp. 36–42, 2009.
- [3] M. Islam, M. R. Amin, R. Carriveau, and A. Fartaj, "Designing straight-bladed vertical axis wind turbine using the cascade theory," in *12th AIAA/ISSMO Multidisciplinary Analysis and Optimization Conference*, American Institute of Aeronautics and Astronautics, Reston, Va, USA, 2008.
- [4] G.-Y. Zhang, W.-M. Feng, and C.-L. Liu, "Numerical simulation on the aerodynamic performance of six kinds of aerofoil of wind turbine blade," in *Renewable Energy Resources*, vol. 2, 2009.
- [5] S.-X. Liao, C. Li, J.-B. Nie et al., "The analysis of aerodynamic performance for small H type VAWT based on different airfoils," in *Machine Design and Research*, vol. 3, 2011.
- [6] M. H. Mohamed, "Performance investigation of H-rotor Darrieus turbine with new airfoil shapes," *Energy*, vol. 47, no. 1, pp. 522–530, 2012.
- [7] Z.-H. Xu, Y. Zhang, B. Yang et al., "Effects of installation method of asymmetric airfoils on performance of H-type wind turbine," *Acta Energy Solaris Sinica*, vol. 34, no. 6, pp. 933–937, 2013.
- [8] H. Xu, H. Yang, and C. Liu, "Numerical value analysis on aerodynamic performance of DU series airfoils with thickened trailing edge," *Transactions of the Chinese Society of Agricultural Engineering*, vol. 17, 2014.
- [9] C.-X. Yang and S.-T. Li, "Study of post stalled airfoil of a H-type vertical axis wind turbine," *Journal of Lanzhou University of Technology*, vol. 41, no. 1, pp. 51–54, 2015.
- [10] Y.-L. Jia, P. Peng, Q.-J. Li et al., "Effects of relative thickness of airfoil on aerodynamics of DU airfoil," *Machinery Design & Manufacture*, vol. 3, 2016.
- [11] F. Feng, Y. Li, L. Chen, W. Tian, and Y. Zhang, "A simulation and experimental research on aerodynamic characteristics of combined type vertical axis wind turbine," *Acta Energetica Solaris Sinica*, vol. 35, no. 5, pp. 855–860, 2014.
- [12] I. Paraschivoiu, C. Li et al., *The vertical axis wind turbine principle and design*, Shanghai Science and Technology Press, 2013.
- [13] Q.-B. He, *Study on calculation of structure and aerodynamic characteristics for vertical axis wind turbine with double-layer retractile blades*, Northeast Agricultural University, Harbin, China, 2015.

## Research Article

# Fault Tolerant Control of Internal Faults in Wind Turbine: Case Study of Gearbox Efficiency Decrease

Younes Ait El Maati , Lhoussain El Bahir , and Khalid Faitah

National School of Applied Sciences, LGECOS Laboratory, Cadi Ayyad University, Marrakech, Morocco

Correspondence should be addressed to Younes Ait El Maati; [aitelmaati.younes@gmail.com](mailto:aitelmaati.younes@gmail.com)

Received 14 November 2017; Accepted 22 March 2018; Published 30 April 2018

Academic Editor: Ali Mostafaeipour

Copyright © 2018 Younes Ait El Maati et al. This is an open access article distributed under the Creative Commons Attribution License, which permits unrestricted use, distribution, and reproduction in any medium, provided the original work is properly cited.

This paper presents a method to control the rotor speed of wind turbines in presence of gearbox efficiency fault. This kind of faults happens due to lack of lubrication. It affects the dynamic of the principal shaft and thus the rotor speed. The principle of the fault tolerant control is to find a bloc that equalizes the dynamics of the healthy and faulty situations. The effectiveness decrease impacts on not only the dynamics but also the steady state value of the rotor speed. The last reason makes it mandatory to add an integral term on the steady state error to cancel the residual between the measured and operating point rotor speed. The convergence of the method is proven with respect to the rotor parameters and its effectiveness is evaluated through the rotor speed.

## 1. Introduction

The wind turbine is an electromechanical device to extract the energy from the wind and feed it to the customer through the grid. The wind turbine is composed of several interconnected components. First, the rotor transforms the aerodynamic torque defined by (1) into mechanical torque. The latter is transformed into electricity through a conventional generator. The bond between the rotor and the generator is performed by the bias of a mechanical gearbox. The role of the gearbox is to maintain the same power from rotor to generator through a transformation ratio  $N_g$  [1]. Figure 1 summarizes the different components of a modern wind turbine.

$$T_a(t) = \frac{1}{2} \rho \pi R^3 V^2 C_q(V, \Omega_r, \beta). \quad (1)$$

The wind turbine (WT) operates in two distinct regions. The first region is called moderate winds ( $<7$  s/m). In this interval, the WT is controlled through the generator torque to maximize the extraction of the energy contained in the wind. The second region is called high winds region ( $>7$  m/s) in which the objective is to maintain a constant power at the nominal value. This is achieved through controlling three actuators existing in each blade. Those actuators are called

pitch because they let the blade turn a pitch angle about its longitudinal axis. By this pitching movement, the blade is exposed ( $0^\circ$  pitch) or not ( $90^\circ$  pitch) to the wind and then the rotor speed is accelerated or decelerated [2]. An overview of the modelling and control of the wind turbine systems could be found in [3].

However, the dusty and wet environment induces degradation in some critical components such as the blades, the shafts, the sensors, the generator, and the mechanical components such as the gearbox. Moreover, the challenging situations in which the wind turbines operate (high winds and turbulences, faults on the sensors, and actuators [4]) require highly available systems. For this reason, fault tolerant control strategies [5] are elaborated to prevent the damaging effect of faults and failures on the turbine structure [6]. Most of the FTC methods are composed of two blocs. The first bloc estimates the fault and provides information about the amplitude and the shape of the fault. The last information is then provided to the FTC bloc to build a new control law suitable for the faulty situation. The production of the new control law could be performed either by changing the regulator's parameters or by adding a new term to the old control law to compensate the fault term. More details on faults in the wind turbines and their FTC could be found in [7], where different types of faults and their corresponding

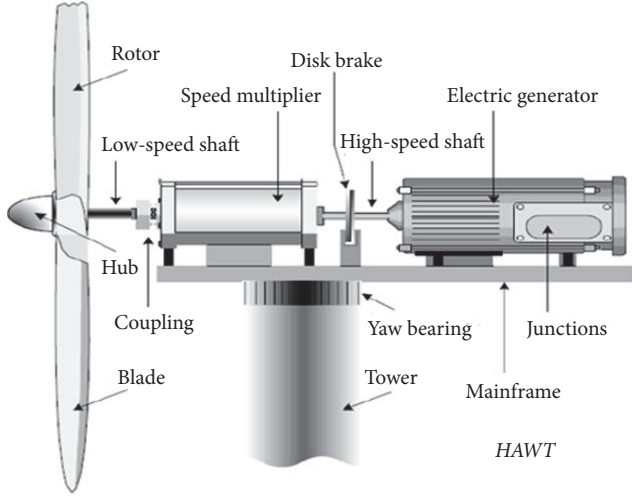


FIGURE 1: The composition of a wind turbine system.

severities are cited. Leakage fault in the hydraulic actuators which is of high severity could not be resolved and the only solution is to shut down the wind turbine for possible maintenance.

In the present paper, the considered fault is the degradation of the efficiency of the gearbox linking the rotor to the generator. It is a fault of medium severity which impacts the dynamics of the rotor and then deteriorates the result of the speed regulation. It will be demonstrated that the fault could be considered an internal fault and a suitable fault tolerant strategy is then applied.

## 2. The Wind Turbine Model

The considered nominal objective of the wind turbine control is to regulate the rotor speed about the operating value of 40 rpm. The chosen operating wind speed is 18 m/s with 30% of variations according to Kaimal distribution.

The blade pitch operating angle is  $9^\circ$ . This operating point belongs to the high wind region where the only objective is to regulate the power by regulating the rotor speed. This prevents the wind turbine from exceeding the nominal values and from being damaged due to high winds. The parameters of the wind turbine are extracted through linearization from the software FAST [8]. FAST is industrial software developed by the National Renewable Energy Laboratory in Colorado to test and validate the control laws on the wind turbines before physical implementation.

The considered control objective requires considering the rotor and the gearbox models.

**2.1. The Rotor Speed Model.** The rotor model of the wind turbine is extracted by applying the first law of mechanics to the turbine and is given by

$$\delta\dot{\Omega}_r = \frac{\gamma}{J_t}\delta\Omega_r + \frac{\xi}{J_t}\delta\beta + \frac{\alpha}{J_t}\delta\omega, \quad (2)$$

where  $\partial T_a/\partial\omega = \alpha$ ;  $\partial T_a/\partial\Omega_r = \gamma$  et  $\partial T_a/\partial\beta = \xi$ .  $T_a$  is the aerodynamic torque applied by the wind on the blades and

defined by (1).  $\delta\omega$  is the variation of the wind speed,  $\delta\beta$  is the variation of the pitch angle, and  $\delta\Omega_r$  is the variation of the rotor speed, about the operating point.  $J_t$  is the total inertia of the wind turbine. The linearization about the chosen operating point gives  $\gamma = -0.1039J_t$ ;  $\xi = -2.5727J_t$ ; and  $\alpha = 0.61141J_t$ .

**2.2. The Gearbox Model.** The gearbox is used to adapt the low speeds (40 rpm) of the rotor to the high speeds of the generator (1500 rpm) while maintaining the same power between the two nodes. This relationship could be modelled by the following equation:

$$J_g\dot{\Omega}_g = \eta_{\text{gbx}}T_{\text{ls},e} - N_gT_g. \quad (3)$$

$\Omega_g$  is the generator speed,  $J_g$  is the generator inertia,  $T_g$  is the generator torque,  $T_{\text{ls},e}$  is the principle shaft torque, and  $\eta_{\text{gbx}}$  and  $N_g$  are, respectively, the efficiency and the multiplication ratio of the gearbox. The variation of the parameter  $\eta_{\text{gbx}}$  induces a variation of the generator speed. This variation is also transmitted to the rotor due to  $N_g$ :

$$\Omega_r = \frac{\Omega_g}{N_g}. \quad (4)$$

The torque  $T_{\text{ls},e}$  is a picture of the aerodynamic torque. The torque should be carefully estimated as in [9].

**2.3. Aerodynamic Torque Estimation.** The aerodynamic torque could be estimated from the drive train model.

**2.3.1. Drive Train Model.** The drive train is composed of a low speed shaft (rotor side) interconnected with a high-speed shaft (generator side) through a mechanical gearbox with a ratio  $N_g$ . The drive train is modelled by the following differential equations:

$$\begin{aligned} \dot{\Omega}_r &= \frac{D_{\text{ls},e}}{J_r}\Omega_r - \frac{X}{J_r} + \frac{D_{\text{ls},e}}{J_r}\Omega_g + \frac{T_a}{J_r} \\ \dot{X} &= K_{\text{ls},e}\Omega_r - K_{\text{ls},e}\Omega_g \end{aligned} \quad (5)$$

$$\dot{\Omega}_g = \frac{D_{\text{ls},e}}{J_g}\Omega_r - \frac{X}{J_g} + \frac{D_{\text{ls},e}}{J_g}\Omega_g + \frac{N_gT_g}{J_g}.$$

$J_r$  is the rotor inertia,  $J_g$  is the generator inertia, and  $X$  is the restoring force applied on the low speed shaft. The shaft is driven by the aerodynamic torque. The generator torque about the equivalent low speed shaft  $N_gT_g$  is used to accelerate or decelerate the shaft.  $D_{\text{ls},e}$  and  $K_{\text{ls},e}$  are the damping and stiffness coefficients of the principle shaft.

**2.3.2. Torque Estimation Loop.** In literature, many approaches have been proposed for aerodynamic torque estimation. Authors in [10] proposed a PI based observer to estimate aerodynamic torque. In [11] authors used the Kalman filter to reconstruct the aerodynamic torque Fourier coefficients. In this paper, the proposed method is based on the transfer function between the aerodynamic torque  $T_a$  and the rotor

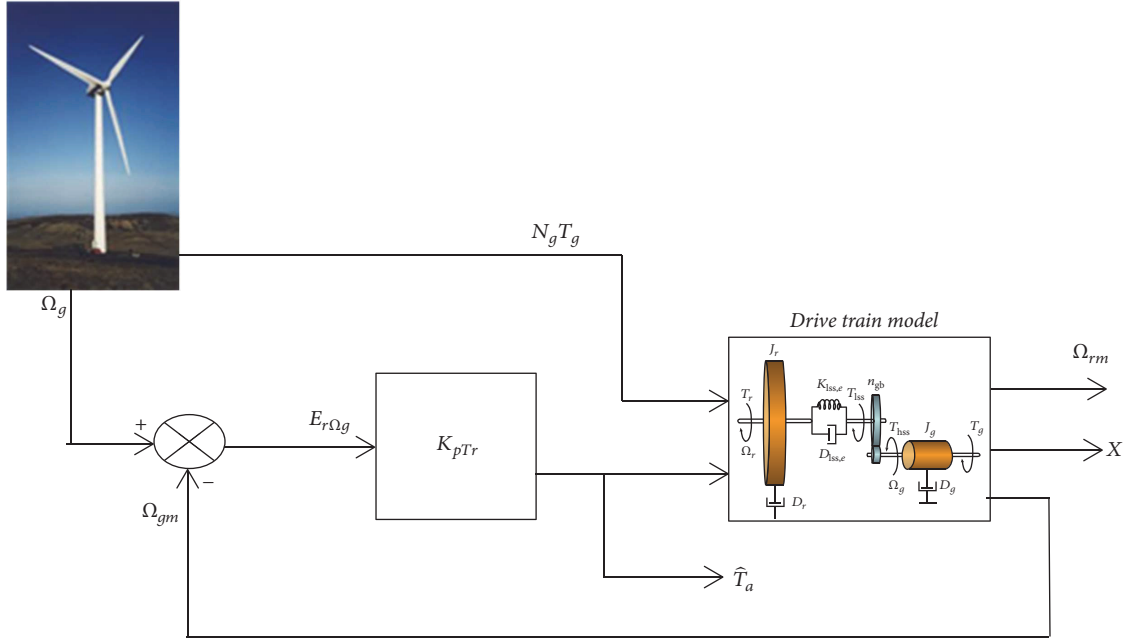


FIGURE 2: Aerodynamic torque feedback estimation loop.

speed  $\Omega_r$ . However, in most cases, the rotor speed cannot be measured; the measured generator speed about low speed shaft could be considered as a good approximation to the rotor speed. In fact, after transients, the rotor and generator speed about the equivalent low speed shaft are the same, in the case of a rigid equivalent shaft, or when damping the torsional modes of the mechanical shaft.

The transfer function  $F(s)$  between the aerodynamic torque  $T_a$  and generator speed  $\Omega_r$  is obtained after manipulations of (5) as follows:

$$F(s) = \frac{1}{s} \frac{as + b}{s^2 + cs + d}, \quad (6)$$

where  $a = D_{lss,e}/J_r J_g$ ;  $b = K_{lss,e}/J_r J_g$ ;  $c = ((J_r + J_g)/J_r J_g) D_{lss,e}$ ; and  $d = K_{lss,e}((J_r + J_g)/J_r J_g)$ .

The idea is to keep the model speed  $\Omega_{gm}$  sufficiently close to the measured one,  $\Omega_g$ , by acting on the model with an adequate aerodynamic torque  $\hat{T}_a$ . This could be performed through a feedback estimation loop as presented in Figure 2. In contrast to authors in the previous works, and since the transfer function  $F(s)$  already contains an integrator term, and assuming that the mean of  $\Omega_g$  is sufficiently low frequency, only a proportional action is needed to estimate  $T_a$ . After transients, the model output  $\Omega_{gm}$  converges to  $\Omega_g$  and its input  $\hat{T}_a$  converges to the actual torque  $T_a$ . Finally,  $\hat{T}_a$  can be considered as an estimation of the actual aerodynamic torque  $T_a$ . The proportional torque estimator gain is chosen in such way that the slowest pole of the closed loop of the transfer function  $F(s)$  is cancelled.

Figure 3 shows the actual and estimated aerodynamic torque. The actual aerodynamic torque represented in Figure 3 by the blue color is obtained for comparison by the following equation:

$$T_a = \text{Rotor}_{\text{Acceleration}} * J_r * \frac{\pi}{180} + \text{Shaft}_{\text{Torque}} * 1000. \quad (7)$$

$J_r$  is the rotor inertia about the shaft of the turbine. The shaft torque (KNm) and the rotor acceleration ( $\text{deg}/\text{sec}^2$ ) can be obtained from FAST software as outputs. In the industrial wind turbines, a strain gauge is installed on the mechanical shaft of the wind turbine to measure the shaft torque. The rotor acceleration is measured by an accelerometer.

Note that  $K_p T_r$  is the proportional torque estimator gain;  $E_r \Omega_g$  is the speed tracking error,  $T_g$  is the generator torque about the high-speed shaft,  $N_g$  is the gearbox ratio, and the term  $N_g T_g$  is the generator torque about the low speed shaft;  $\Omega_{gm}$  is the model generator speed about low speed shaft;  $\Omega_g$  is the measured generator speed;  $X$  is the restoring force of the low speed shaft;  $\Omega_{rm}$  is the model rotor speed;  $\hat{T}_a$  is the estimated aerodynamic torque.

Define the mean convergence error between actual aerodynamic torque  $T_a$  and estimated aerodynamic torque  $\hat{T}_a$  along  $N$  samples of data:

$$\text{error} (\%) = \frac{100}{N} \sum_{i=1}^N \left| \frac{T_{a,i} - \hat{T}_{a,i}}{T_{a,i}} \right|. \quad (8)$$

In the present case of simulation, we obtain a relative error of 1.8%. The torque estimation could then be considered sufficiently accurate.

**2.4. Estimated Aerodynamic Torque Filtering.** In this section, a spectral analysis is performed to identify the frequencies of the wind speed transmitted to the torque and those resulting from the mechanical vibration. The objective is to reconstruct the frequencies specific to the wind speed. Figures 4 and 5 show the power spectral density of the wind profile and aerodynamic torque, respectively.

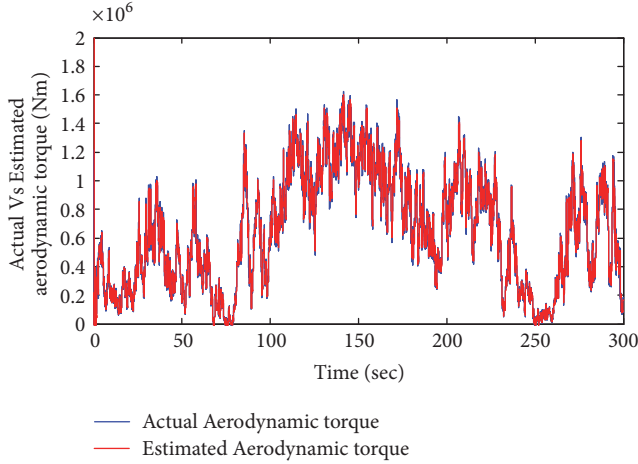


FIGURE 3: The actual and estimated aerodynamic torque.

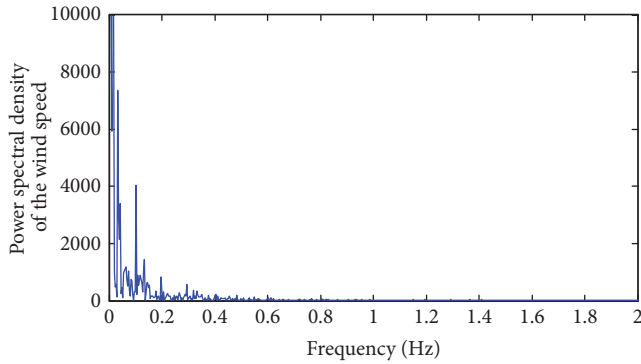


FIGURE 4: Power spectral density of the wind.

One can notice that the frequencies contained in the wind and having a significant effect on the torque of the rotor resides in the low frequency range ( $<0.12$  Hz). The peaks that occur beyond this area are the result of vibrations of the mechanical structure as a result of excitations caused by the wind. The estimated aerodynamic torque, which will be used for reconstitution of the wind speed, should therefore be filtered according to the previous remark. In the case of our system, we chose a low pass filter of 0.4 Hz bandwidth. Figure 6 shows the power spectral density of filtered and the unfiltered torque.

From Figure 6, one can notice that frequencies above 0.4 Hz have been attenuated and filtered.

**2.5. Gearbox Efficiency Estimation.** After estimation of the principal shaft torque, the gearbox efficiency variations  $\eta_{\text{gbx}}$  could be estimated through (3) as in [12] by the following manipulations:

$$\begin{aligned}
 sJ_g\Omega_g &= \eta_{\text{gbx}}T_{\text{Iss},e} - N_gT_g \\
 sJ_g\Omega_g + N_gT_g &= T_{\text{Iss},e}\eta_{\text{gbx}} \\
 \underbrace{\Omega_g + \frac{N_gT_g}{sJ_g}}_Y &= \frac{T_{\text{Iss},e}}{sJ_g}\eta_{\text{gbx}}.
 \end{aligned} \tag{9}$$

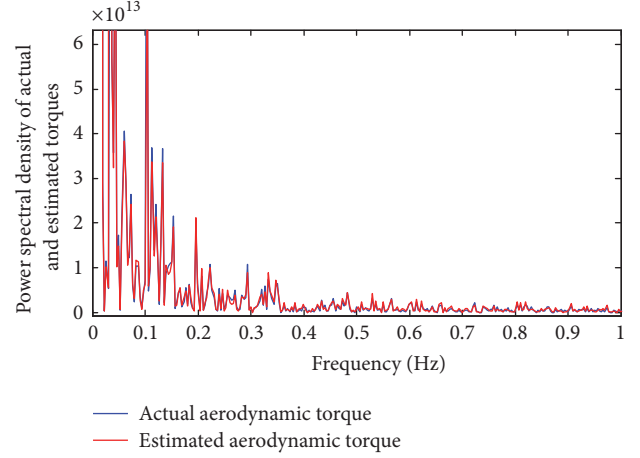


FIGURE 5: Power spectral density of the actual and estimated shaft torque.

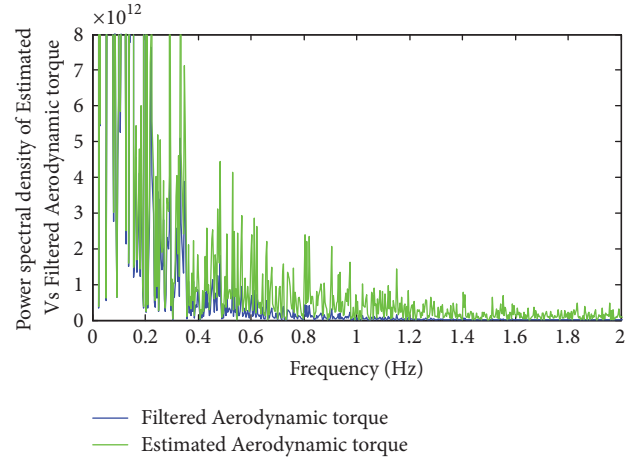


FIGURE 6: The power spectral density of the estimated and filtered aerodynamic torque.

Figure 7 shows the fault detection scheme of the gearbox efficiency.

$\Omega_g$  is the measured generator speed,  $E_Y$  is the tracking error loop,  $\eta_{\text{gbxm}}$  is the estimated drive train efficiency,  $N_gT_g$  is the generator torque about the low speed shaft, and  $T_{\text{Iss},e}$  is the previously estimated shaft torque.  $Y$  is the measured variable to be tracked by the model's output.  $C_n(s)$  is the proportional action transfer function used for the estimation.  $C_n(s)$  is a constant gain  $M$ .

In the present case, the proportional gain  $M$  is fixed at lower values and progressively increases until we have got good estimation results. For this turbine, we found optimal  $K$  at 0.9.

Figure 8 represents different results of estimation for different gearbox efficiencies. The estimate of  $\eta_{\text{gbx}}$  constitutes a fault residual, given by (10), used in the activation of the fault tolerant control if a gearbox fault happens. In fact, when  $r \neq 1$ , it means that the efficiency of the gearbox

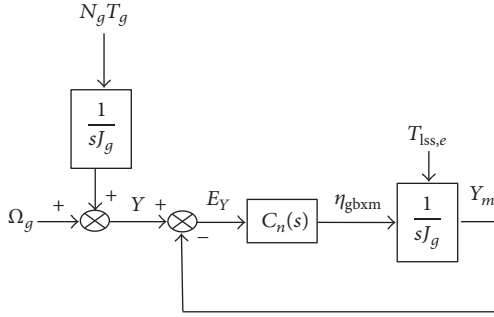


FIGURE 7: Gearbox efficiency detection scheme.

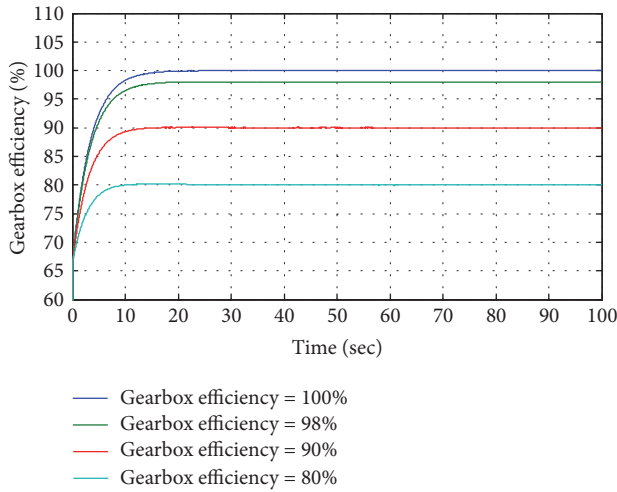


FIGURE 8: Estimation of gearbox efficiency 100%, 98%, 90%, and 80%.

decreases and the fault tolerant control bloc should be activated.

$$r = 100\% - \eta_{gbx}. \quad (10)$$

Since the fault in  $\eta_{gbx}$  affects the generator speed as in (3), and the generator speed is linked to the rotor speed through (4), it can be concluded that this fault affects only the dynamics of the rotor represented by the parameter  $\gamma/J_t$  in (3). This conclusion is verified only under the assumption that no actuator fault neither sensor faults are present at the same time with the gearbox loss of efficiency fault.

**2.6. Gearbox Efficiency Impact on the Eigenvalues of the Dynamic Matrix.** Figure 9 illustrates the variation of the eigenvalues of the dynamic matrix with respect to the gearbox efficiency. For efficiencies less than 20%, the variations of the eigenvalues are fast with a gradient of 0.62 in absolute values. This gradient becomes slower with 0.1633 for values more than 20% of efficiencies. This means that, for values less than 20%, it is easy to reach eigenvalues near the instability (near 0) than for values more than 20%. The algebraic equation representing the curve in Figure 9 is given by

$$f(\eta_{gbx}) = a \times \eta_{gbx}^b + c, \quad (11)$$

where  $a = -0.3203$ ;  $b = 0.0604$ ;  $c = 0.3124$ .

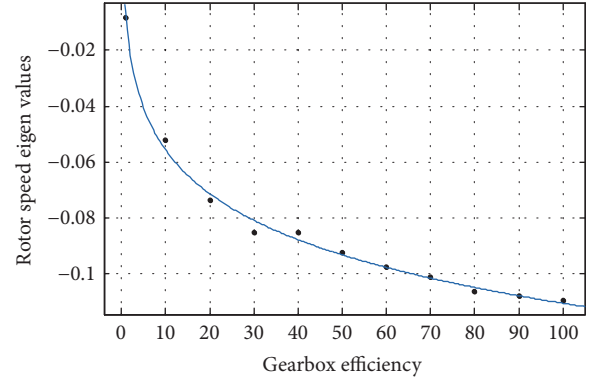


FIGURE 9: The variations of the eigenvalues of the dynamics matrix of the rotor speed with respect to the gearbox efficiency.

This paragraph shows that the efficiency fault impacts the stability of the system. Hence, the fault tolerant control becomes necessary.

### 3. The Fault Tolerant Control Strategy

**3.1. Dynamics Equalization Gain.** The fault tolerant bloc to be computed should satisfy the following condition:

$$A_f + BKC \xrightarrow{t \rightarrow \infty} A, \quad (12)$$

where  $A$ ,  $B$ , and  $C$  represent the dynamic, input action, and measurement matrix of the healthy system.  $A_f$  represents the dynamic matrix affected by the fault and  $K$  is the bloc to be computed, where

$$\begin{aligned} A_f &= \frac{\gamma_f}{J_t}; \\ A &= \frac{\gamma}{J_t}; \\ B &= \frac{\xi}{J_t}; \\ C &= 1. \end{aligned} \quad (13)$$

The resolution of (12) with respect to  $K$  while applied on the model of the wind turbine in (2) gives the value of  $K$ :

$$K = \frac{\gamma - \gamma_f}{\xi}, \quad (14)$$

where  $\gamma$  and  $\xi$  are turbine dependent coefficients defined in (2) of the healthy model of the rotor.  $\gamma_f$  is the coefficient  $\gamma$  but in the faulty situation.

The new control law is then given by

$$\beta_f = \beta + K\Omega_{rf}. \quad (15)$$

3.2. *Convergence of the Dynamics Equalization Method.* Let us define the healthy system by (2) and the faulty system by

$$\begin{aligned}\delta\dot{\Omega}_{rf} &= \frac{\gamma_f}{J_t}\delta\Omega_{rf} + \frac{\xi}{J_t}\delta\beta_f + \frac{\alpha}{J_t}\delta\omega \\ \delta\beta_f &= \delta\beta + K\delta\Omega_{rf}.\end{aligned}\quad (16)$$

And the error between the faulty rotor speed and the healthy rotor speed is defined by

$$e = \delta\Omega_{rf} - \delta\Omega_r. \quad (17)$$

The dynamics of the error are given by

$$\dot{e} = \delta\dot{\Omega}_{rf} - \delta\dot{\Omega}_r = \frac{\gamma_f}{J_t}\delta\Omega_{rf} + \frac{\xi}{J_t}K\delta\Omega_{rf} - \frac{\gamma}{J_t}\delta\Omega_r. \quad (18)$$

By taking  $K$  as in (14), the error dynamics become

$$\begin{aligned}\dot{e} &= \frac{\gamma_f}{J_t}\delta\Omega_{rf} + \frac{\xi}{J_t}\frac{\gamma - \gamma_f}{\xi}\delta\Omega_{rf} - \frac{\gamma}{J_t}\delta\Omega_r \\ &= \frac{\gamma_f + \gamma - \gamma_f}{J_t}\delta\Omega_{rf} - \frac{\gamma}{J_t}\delta\Omega_r = \frac{\gamma}{J_t}\delta\Omega_{rf} - \frac{\gamma}{J_t}\delta\Omega_r \\ &= \frac{\gamma}{J_t}(\delta\Omega_{rf} - \delta\Omega_r) = \frac{\gamma}{J_t}e.\end{aligned}\quad (19)$$

Since  $\gamma/J_t$  is negative (by the nature of the rotor), the error dynamics converges to zero as the time evolves. It can be concluded that the stability of the method depends on the stability of the initial system and any deviation from the healthy speed will be caused only by the imperfections of the model.

3.3. *Steady State Reconfiguration by Residual Integration.* The gearbox efficiency impacts also the steady state of the rotor speed. For this, an integral part is needed to cancel the static error between 40 rpm and the real time measured rotor speed. The global fault tolerant control law is given by

$$\delta\beta_f = \delta\beta + K\delta\Omega_{rf} + N \int (\delta\Omega_{rf} - \delta\Omega_r). \quad (20)$$

In this simulation, a good value of  $N$  is  $-0.03$ .

3.4. *Convergence of the Integrated Strategy.* We take  $K$  as in (14), the error dynamics using control law in (20) becomes

$$\dot{e} = \frac{\gamma}{J_t}e + \frac{\xi N}{J_t} \int e. \quad (21)$$

This means that

$$\begin{bmatrix} \dot{e} \\ e \end{bmatrix} = \begin{bmatrix} 0 & 1 \\ \frac{\xi N}{J_t} & \frac{\gamma}{J_t} \end{bmatrix} \begin{bmatrix} e \\ \int e \end{bmatrix}. \quad (22)$$

The dynamics in (22) are stable, if the eigenvalues of the matrix  $\begin{bmatrix} 0 & 1 \\ \xi N/J_t & \gamma/J_t \end{bmatrix}$  are of negative real parts. The eigenvalues of the matrix are given by  $\lambda_1$  and  $\lambda_2$  in (23) as

$$\lambda_{1,2} = \frac{\gamma \pm \sqrt{\gamma^2 + 4J_t N \xi}}{2J_t}. \quad (23)$$

To obtain eigenvalues with negative real parts, one should resolve inequality  $\lambda_{1,2} < 0$ .

$$\begin{aligned}\gamma &< \sqrt{\gamma^2 + 4J_t N \xi} \implies \\ \gamma^2 &< \gamma^2 + 4J_t N \xi \implies \\ 0 &< 4J_t N \xi.\end{aligned}\quad (24)$$

While  $\xi$  is negative and  $J_t$  is positive,  $N$  should be fixed negative  $N < 0$  to have stability of the integrated method.

3.5. *Robustness Considerations.* Let define a robustness level  $\theta$  which should robustify the method (represented by the error  $e$ ) against the wind disturbance  $\omega$ . The inequality to be verified is given by

$$|e| < \theta |\omega|, \quad (25)$$

where  $e = \delta\Omega_{rf} - \delta\Omega_r$  and  $\delta\Omega_r = \delta\Omega_{r,ref} = 0$  rpm deviation from the operating rotor speed. After applying the FTC method, the closed loop rotor system becomes

$$\begin{aligned}\delta\dot{\Omega}_{rf} &= \left(\frac{\gamma_f}{J_t} + K\right)\delta\Omega_{rf} + \frac{\xi}{J_t}\delta\beta_f + \frac{\alpha}{J_t}\delta\omega + N \int \delta\Omega_{rf} \\ &\quad - N \int \delta\Omega_r.\end{aligned}\quad (26)$$

In the present paper, the desired rotor speed reference  $\delta\Omega_{r,ref}$  is 0 rpm deviation from the operating speed 40 rpm. Equation (26) could be simplified to

$$\begin{aligned}\delta\dot{\Omega}_{rf} &= \left(\frac{\gamma_f}{J_t} + K\right)\delta\Omega_{rf} + \frac{\xi}{J_t}\delta\beta_f + \frac{\alpha}{J_t}\delta\omega \\ &\quad + N \int \delta\Omega_{rf}.\end{aligned}\quad (27)$$

And the error becomes equivalent to  $e = \delta\Omega_{rf}$ . So the inequality to be verified becomes

$$|\delta\Omega_{rf}| < \theta |\omega|. \quad (28)$$

The objective is to extract the transfer function between the turbulence  $\delta\omega$  and the rotor speed  $\delta\Omega_{rf}$ . For this aim, the Laplace transform is applied to

$$\begin{aligned}s\delta\Omega_{rf} &= \left(\frac{\gamma_f}{J_t} + K\frac{\xi}{J_t}\right)\delta\Omega_{rf} + \frac{\xi}{J_t}\delta\beta + \frac{\alpha}{J_t}\delta\omega + \frac{N}{s}\frac{\xi}{J_t}\delta\Omega_{rf} \implies \\ \delta\Omega_{rf} &\left(s - \frac{\gamma_f}{J_t} - K\frac{\xi}{J_t} - \frac{N}{s}\frac{\xi}{J_t}\right) = \frac{\xi}{J_t}\delta\beta + \frac{\alpha}{J_t}\delta\omega.\end{aligned}\quad (29)$$

If the disturbance effect is considered, the transfer function could be obtained by

$$\begin{aligned}\frac{\delta\Omega_{rf}}{\delta\omega} &= \frac{\alpha/J_t}{\left(s - \gamma_f/J_t - K(\xi/J_t) - (N/s)(\xi/J_t)\right)} \\ &= \frac{(\alpha/J_t)s}{\left(s^2 - (\gamma_f/J_t + K(\xi/J_t))s - N(\xi/J_t)\right)}.\end{aligned}\quad (30)$$

If the Laplace operator  $s$  is replaced by  $j\tau$ , where  $j$  is the complex number and  $\tau$  is the pulsation ( $2\pi f$ ). The module of the transfer function is then given by

$$\begin{aligned} \left| \frac{\delta\Omega_{rf}}{\delta\omega} \right| &= \frac{|(\alpha/J_t) j\tau|}{|(j\tau)^2 - (\gamma_f/J_t + K(\xi/J_t)) j\tau - N(\xi/J_t)|} \\ &= \frac{|(\alpha/J_t) j\tau|}{|-(\tau)^2 - (\gamma_f/J_t + K(\xi/J_t)) j\tau - N(\xi/J_t)|} \\ &= \frac{(\alpha/J_t) \tau}{\sqrt{((\tau)^2 + N(\xi/J_t))^2 + (\tau(\gamma_f/J_t + K(\xi/J_t)))^2}} \end{aligned} \quad (31)$$

By replacing (31) in (28), inequality (28) becomes equivalent to

$$\begin{aligned} \frac{(\alpha/J_t) \tau}{\sqrt{((\tau)^2 + N(\xi/J_t))^2 + (\tau(\gamma_f/J_t + K(\xi/J_t)))^2}} < \theta &\implies \\ \frac{\alpha}{J_t} \tau < \theta \sqrt{(\tau^2 + N \frac{\xi}{J_t})^2 + (\tau(\frac{\gamma_f}{J_t} + K \frac{\xi}{J_t}))^2} &\implies \\ \frac{\alpha}{J_t} \theta > \sqrt{\left(1 + N \frac{\xi}{J_t \tau^2}\right)^2 + \left(\frac{\gamma_f}{J_t} + K \frac{\xi}{J_t}\right)^2} &\implies \\ \left(\frac{\alpha}{J_t} \theta\right)^2 > \left(1 + N \frac{\xi}{J_t \tau^2}\right)^2 + \left(\frac{\gamma_f}{J_t} + K \frac{\xi}{J_t}\right)^2 &\implies \\ \left(1 + N \frac{\xi}{J_t \tau^2}\right)^2 < \left(\frac{\alpha}{J_t} \theta\right)^2 - \left(\frac{\gamma_f}{J_t} + K \frac{\xi}{J_t}\right)^2 &\implies \\ 1 + N \frac{\xi}{J_t \tau^2} < \sqrt{\left(\frac{\alpha}{J_t} \theta\right)^2 - \left(\frac{\gamma_f}{J_t} + K \frac{\xi}{J_t}\right)^2} &\implies \\ N \frac{\xi}{J_t \tau^2} < \sqrt{\left(\frac{\alpha}{J_t} \theta\right)^2 - \left(\frac{\gamma_f}{J_t} + K \frac{\xi}{J_t}\right)^2} - 1 &\implies \\ N > \frac{J_t \tau^2}{\xi} \sqrt{\left(\frac{\alpha}{J_t} \theta\right)^2 - \left(\frac{\gamma_f}{J_t} + K \frac{\xi}{J_t}\right)^2} - 1 \end{aligned} \quad (32)$$

The inequality symbol change between the two last lines of (32) comes because the term  $\xi/J_t \tau^2$  is inferior to 0.

Finally,

$$\frac{J_t \tau^2}{\xi} \sqrt{\left(\frac{\alpha}{J_t} \theta\right)^2 - \left(\frac{\gamma_f}{J_t} + K \frac{\xi}{J_t}\right)^2} - 1 < N < 0. \quad (33)$$

Then, to ensure robustness level  $\theta$ , and given a pulsation  $\tau = 2\pi f$  (rad/s) the design parameter  $N$  should verify inequality (33). It is recommended to take the maximal frequency contained in the wind equal to 1 Hz as in Section 2, Figure 4.

#### 4. Results and Discussions

Figure 10 illustrates the rotor speed in the nominal, faulty, and fault tolerant cases. In order to evaluate the effectiveness

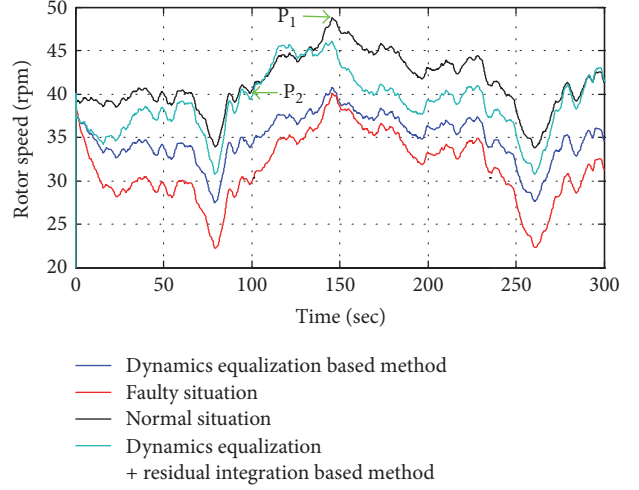


FIGURE 10: The rotor speed in the normal, faulty, and fault tolerant situation.

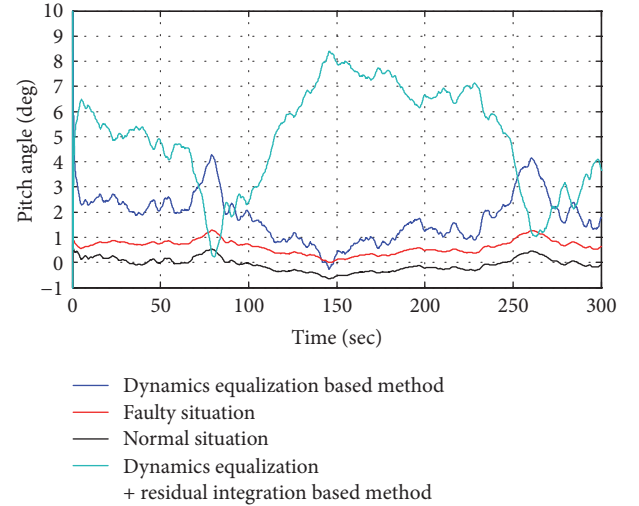


FIGURE 11: The pitch angles (control effort) in the normal, faulty, and fault tolerant situation.

of the method, the distance (according to the ordinates axis) between two points on the curve is considered. The first point is P1 with abscissa 143 seconds and the second point P2 with 90.34 seconds of abscissa. In the nominal situation, the difference between the ordinates of P1 and P2 is of 8.1 rpm; this value becomes 11.5 rpm in the faulty situation. By using the fault tolerant control strategy, this value is reduced to 9.2 rpm. As shown in the same Figure 10, not only the dynamics are impacted but also the steady state value of the rotor speed which become closer to 40 rpm operating point due to the integral term  $N \int (\delta\Omega_{rf} - \delta\Omega_r)$  in the control law.

Figure 11 illustrates the pitch angle in the three situations. It can be stated that, in the faulty situation (red), the nominal regulator “tries” to beat the deviation in the speed by generating some pitch angles but without satisfactory results. By adding the term  $K\delta\Omega_{rf}$  to the old control signal, the efforts become bigger and the difference between the points P1 and

P2 is reduced. In the integrated method, the efforts become bigger and the integral part is evidently impacting the pitch angles to cancel the steady state error.

Compared to other methods, the proposed strategy reconstructs the rotor speed while keeping the generated power constant as before the fault occurrence. In fact, another way to do is to decrease the operating point generator torque in (3) to maintain the same generator speed variations and then the same rotor speed variations  $\delta\Omega_r$ . This could be done by multiplying the generator torque input by the estimated gearbox efficiency. This method helps keeping the rotor speed as it was but impacts the generator torque and then the generated power whose expression is given by

$$\delta P_g = \delta\Omega_r \times \delta T_g. \quad (34)$$

The method of this paper uses pitch actuators instead of generator torque and this helps keeping the generated power constant and then satisfies continuously the customer demand of electricity.

## 5. Conclusion

In this paper, a fault tolerant control method composed of several steps is proposed to deal with the loss of gearbox efficiency. This fault occurs due to the dusty environment of the modern large scale wind turbines. The first step is to estimate the shaft torque through a suitable transfer function between the rotor speed and the shaft torque. The last torque is used to estimate in real time the gearbox efficiency through a suitable loop. The estimated efficiency is used to select a corresponding eigenvalue from Figure 9. A design coefficient  $K$  is computed so the dynamics of the pre-fault and post-fault cases are equalized. The rotor speed steady state is reconstructed by adding an integral part of the residual between the measured and reference rotor speed (zero deviation from operating point is desired).

On the other hand, a performance based conditions were given to help choosing the design integration parameter  $N$ . Based on the fact that the residual should not be impacted by the wind disturbance; a performance level  $\theta$  has been proposed to verify  $|e| < \theta|\omega|$ . The last inequality helps to give a negative (because  $\xi$  is by construction negative) inferior limit to  $N$  function of  $\theta$  as  $(J_t \tau^2 / \xi) \sqrt{((\alpha/J_t)\theta)^2 - (\gamma_f/J_t + K(\xi/J_t))^2} - 1$ .

The method is characterized by its ease of elaboration and parameters design and especially helps keeping a continuous production of the power in contrast to the generator torque based method.

## Conflicts of Interest

The authors declare that there are no conflicts of interest regarding the publication of this paper.

## References

[1] H. P. Wang, A. Pintea, N. Christov, P. Borne, and D. Popescu, "Modelling and recursive power control of horizontal variable

speed wind turbines," *Control Engineering and Applied Informatics*, vol. 14, no. 4, pp. 33–41, 2012.

- [2] K. T. Magar, M. J. Balas, and S. A. Frost, "Smooth transitioning of wind turbine operation between region II and region III with adaptive disturbance tracking control," *Wind Engineering*, vol. 38, no. 3, pp. 337–348, 2014.
- [3] Y.-D. Song, P. Li, W. Uu, and M. Qin, "An overview of renewable wind energy conversion system modeling and control," *Measurement + Control*, vol. 43, no. 7, pp. 203–208, 2010.
- [4] J. Ribrant and L. M. Bertling, "Survey of failures in wind power systems with focus on Swedish wind power plants during 1997–2005," *IEEE Transactions on Energy Conversion*, vol. 22, no. 1, pp. 167–173, 2007.
- [5] V. Rezaei and F. R. Salmasi, "Robust adaptive fault tolerant pitch control of wind turbines," *Wind Engineering*, vol. 38, no. 6, pp. 601–612, 2014.
- [6] P. F. Odgaard, J. Stoustrup, and M. Kinnaert, "Fault-tolerant control of wind turbines: A benchmark model," *IEEE Transactions on Control Systems Technology*, vol. 21, no. 4, pp. 1168–1182, 2013.
- [7] P. Li, Y. Song, W. Liu, and M. Qin, "Monitoring of Wind Turbines: A Bio-Inspired Fault Tolerant Approach," *Measurement + Control*, vol. 44, no. 4, pp. 111–115, 2011.
- [8] J. M. Jonkman and M. L. Buhl, "FAST User's Guide - Updated August 2005," Tech. Rep. NREL/TP-500-38230, 2005.
- [9] Y. Ait Elmaati, L. El Bahir, and K. Faitah, "An integrator based wind speed estimator for wind turbine control," *Wind and Structures, An International Journal*, vol. 21, no. 4, pp. 443–460, 2015.
- [10] K. Z. Østergaard, P. Brath, and J. Stoustrup, "Estimation of effective wind speed," *Journal of Physics: Conference Series*, vol. 75, no. 1, Article ID 012082, 2007.
- [11] G. Hafidi and J. Chauvin, "Wind speed estimation for wind turbine control," in *Proceedings of the 2012 IEEE International Conference on Control Applications, CCA 2012*, pp. 1111–1117, Croatia, October 2012.
- [12] Y. Ait Elmaati, L. El Bahir, and K. Faitah, "Residual generation for the gearbox efficiency drop fault detection in the NREL 1.5WindPact turbine," in *Proceedings of the 1st International Conference on Electrical and Information Technologies, ICEIT 2015*, pp. 77–81, Morocco, March 2015.

## Research Article

# Time-Dependent Effects of Glaze Ice on the Aerodynamic Characteristics of an Airfoil

Narges Tabatabaei <sup>1</sup>, Michel J. Cervantes,<sup>1</sup> and Chirag Trivedi<sup>2</sup>

<sup>1</sup>University of Technology, Luleå, Sweden

<sup>2</sup>Department of Energy and Process Engineering, Faculty of Engineering, Norwegian University of Science and Technology (NTNU), Trondheim, Norway

Correspondence should be addressed to Narges Tabatabaei; [narges.tabatabaei@ltu.se](mailto:narges.tabatabaei@ltu.se)

Received 29 September 2017; Accepted 30 January 2018; Published 7 March 2018

Academic Editor: Mamdouh H. Assad

Copyright © 2018 Narges Tabatabaei et al. This is an open access article distributed under the Creative Commons Attribution License, which permits unrestricted use, distribution, and reproduction in any medium, provided the original work is properly cited.

The main objective of this study is to estimate the dynamic loads acting over a glaze-iced airfoil. This work studies the performance of unsteady Reynolds-averaged Navier-Stokes (URANS) simulations in predicting the oscillations over an iced airfoil. The structure and size of time-averaged vortices are compared to measurements. Furthermore, the accuracy of a two-equation eddy viscosity turbulence model, the shear stress transport (SST) model, is investigated in the case of the dynamic load analysis over a glaze-iced airfoil. The computational fluid dynamic analysis was conducted to investigate the effect of critical ice accretions on a 0.610 m chord NACA 0011 airfoil. Leading edge glaze ice accretion was simulated with flat plates (spoiler-ice) extending along the span of the blade. Aerodynamic performance coefficients and pressure profiles were calculated and validated for the Reynolds number of  $1.83 \times 10^6$ . Furthermore, turbulent separation bubbles were studied. The numerical results confirm both time-dependent phenomena observed in previous similar measurements: (1) low-frequency mode, with a Strouhal number  $St_l \approx 0.013$ – $0.02$ , and (2) higher frequency mode with a Strouhal number  $St_l \approx 0.059$ – $0.69$ . The higher frequency motion has the same characteristics as the shedding mode and the lower frequency motion has the flapping mode characteristics.

## 1. Introduction

Ice accretion on aerodynamic surfaces leads to significant deterioration of the blade performance and operation [1]. Heavy icing disrupts the continual power generation from the wind turbines and the disruption may be prolonged in severe cold conditions. The database published by “Statistics Sweden” showed 161,523 hours of total downtime for the period 1998–2003 where 7% of the downtime was related to icing condition and resulted in over 5% production loss in the country [2].

In 1958, the effects of ice formation on different airfoil sections were studied by NACA [3]. They measured lift, drag, and pitching moment coefficients of an NACA 65A004 airfoil section. The icing on the airfoil caused a rapid increase of the drag coefficient, a drop of the lift coefficient, and change in the pitching moment coefficient. In 2012, Villalpando et al. [4] conducted numerical simulations over a two-dimensional ice-accreted NACA 63-415 airfoil at various angles of attack.

They validated the load coefficients with experimental data at one angle of attack and extracted the modified pressure distribution due to the ice accumulation. The ice accumulated over the airfoil modified the pressure distribution ( $C_p$ ) affecting considerably the aerodynamic performances. Further, in 2014 [5] experimental and numerical investigations demonstrated that with increasing angle of attack the degradation of the instantaneous lift coefficient increases with a linear process.

Ice accretion is a phenomenon where super-cooled water droplets impinge and accrete on a body. Icing occurs on the leading edge of wind turbine blades [6]. The ice likely to form on wind turbine blades is of two kinds [7]. The first is called “rime ice,” which is generated at very low temperature, below  $-10^\circ\text{C}$ . In rime ice conditions, the droplets in the air freeze instantly at the impingement point. The second is called “glaze ice,” which is generated in the temperature range  $-10$  to  $0^\circ\text{C}$ . On glaze ice conditions, droplets gradually freeze while moving along the body, so-called runback [8].

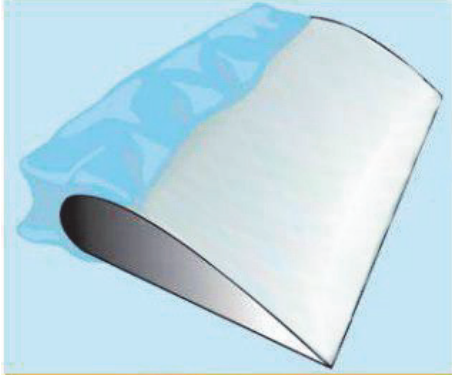


FIGURE 1: Double-horn glaze ice.

Glaze ice accretion is often characterized by the presence of large protuberances, commonly known as glaze horns (Figure 1), which can cause flow separation downstream of the horns [9]. On iced airfoils, the boundary layer separates near the top of the horn, due to the pressure gradient produced by the large discontinuity in the surface geometry. This is a reason why CFD prediction is more challenging in the case of airfoil/blade with glaze ice than with rime ice [10].

In 1986 [11] experiments were conducted to study the aerodynamic characteristics of the NACA 0012 airfoil under glaze ice accretion. Lift and drag penalties due to the ice shape were found and the surface pressure showed the presence of large separation bubbles. A large flow separation region was observed and correlated to the pressure measurements. The iced cases were also analyzed numerically at angles of attack below stall [12]. In 2018, the ice accretion transient phenomenon and its effect on turbine performance was studied by coupling 2D steady state CFD, with a blade momentum and an ice accretion code [13].

As the specification of the horn is determinative in the subsequent vortices structure, a parametrization of these horns is desired. Although the exact size and shape of the ice formations are found to be complex functions of both the operating and icing conditions, a horn shape can be characterized by its height, the angle it makes with respect to the chord line, and its location [14]. In the mentioned studies ([11, 12]), the simulated ice shapes were constructed to approximately duplicate an actual measured ice accretion. The ice was accreted in an Icing Research Tunnel on a NACA 0012 airfoil. In an experimental study [15], glaze ice shapes were simulated by means of spoilers attached on the upper surface of an airfoil near the leading edge as a single-horn glaze ice. The spoilers modeled in this work were sized to simulate 22.5-minute glaze ice accretions for the NACA 0011 airfoil. Leading edge glaze ice accretions characteristically may consist of an upper and lower surface horns, called double-horn ice. In 2000, experimental data were provided for the NACA 0011 airfoil with simulated glaze ice shapes on both upper and lower surfaces [9]. The ice accretions can also be simulated with wooden forward-facing quarter-round shapes. Lee and Bragg [16, 17] have tested some geometries consisting of

backward facing quarter-round, half-round, and forward-facing ramp. In [18], the simulated glaze horn-type ice accretions were determined from averaging geometry data from a set of actual ice accretions collected in a test at an Icing Research Tunnel. Single-horn simulations were used for that research by means of a 3 by 3 matrix of ice shape size and radius which was designed to parametrically vary these parameters. In [19] a single-horn glaze ice was placed on the upper surface of the airfoil which was a combination of a semicircle and a rectangle. In the previous study [20], steady state simulations were performed to investigate the mean flow characteristics. The aerodynamic performance coefficients and pressure profile were determined with CFD and compared with the available measurements in [9]. The steady state simulations were not found to be reliable to calculate the loads in the case of iced airfoil. Time-dependent simulations were conducted to determine the vortices structure. It was concluded that the thickness of the leading edge glaze ice should be taken as an effective parameter of an ice shape. Although it does not change the formed vortices on the airfoil downstream of the spoiler tip, it can affect the acting forces on the spoilers. As a matter of fact, the main part of the total lift force on the airfoil was found to be on the spoilers where the ice shape may significantly affect the lift and drag.

The leading edge ice accretion not only may be detrimental to aerodynamic performance but also can be a concern in terms of large unsteady loads associated with the flow separation [21]. Generally, the steady state effects of the separation bubbles on the airfoil performance are characterized by large increases in drag, reductions in lift, and changes in airfoil pitching moment characteristics. The separation occurs at the tip of the horn ice shape (Figure 1) and immediately a shear layer forms, which separates the recirculation region from the freestream flow. The shear layer begins to roll as it moves downstream, and vortices within the shear layer merge, forming larger vortical structures.

Understanding the behavior of the separation bubble is critical to understand the effect of ice accretion on airfoil aerodynamics. Laminar separation bubbles on airfoil have been widely studied [22–26]. The bubble forms when a laminar boundary layer encounters an adverse pressure gradient of sufficient strength to cause separation. The separated flow may be divided into two main regions: The free shear layer and the recirculation bubble. These two regions may then be further subdivided into parts, upstream and downstream of the transition point. After transition, the magnitude of the reverse flow increases and a vortex type flow is seen in the bubble. Before the transition, the reverse flow is very slow and this area is sometimes referred to as a dead-air region.

Flows at high Reynolds number with separation and reattachment have long been a subject of many studies [27]. In 1983, the structure of a turbulent separation bubble was studied by Kiyama and Sasaki [28]. In their measurements, they observed a large-scale unsteadiness accompanied by an enlargement and shrinkage of the bubble and a flapping motion of the shear layer near the separation line. At a turbulent separation bubble, the flow is characterized by two separate time-dependent phenomena: flapping and shedding [29]. One mode is associated with a global breathing motion of the

separation bubble, described as “flapping motion” in the literature. The other mode is associated with the roll-up of spanwise vortices in the shear layer above the recirculating region and their shedding downstream of the separated zone. The regular mode includes the presence of vortical motion in the separated shear layer and vortex shedding from the separation bubble. The source of the regular mode has been attributed to the Kelvin-Helmholtz instability, where the difference between the velocity within the recirculation region of the separation bubble and the external flow causes a roll-up and shedding of vortices within the shear layer [30]. The shear layer flapping is characterized by low frequencies at certain locations in the separation bubble downstream of the separation onset. The oscillations tend to operate across different frequency scales compared with those of the regular mode [30].

As the shear layer vortices are formed and shed, the height and length of the separation bubble tend to change as a function of time [11]. The boundary layer events produce variations in lift, drag, and moment coefficients [31]. It has been found that the frequency of the oscillating flow can be nondimensionalized with the Strouhal number  $St$  based on the momentum thickness ( $St_\theta = f\theta/U_\infty$ ) [31], airfoil projected height ( $St_h = fc \sin \alpha/U_\infty$ ) [21, 26, 30], or separation bubble length ( $St_L = fL/U_\infty$ ) [30], where  $f$  is the flow oscillation frequency,  $L$  is the separation bubble length,  $c$  is the airfoil chord,  $\theta$  is the boundary layer momentum thickness,  $\alpha$  is the angle of incidence, and  $U_\infty$  is the freestream mean velocity. Most results from the literature identify the effects of shear layer flapping as occurring at a Strouhal number on the order of  $St_h = 0.02$  or  $St_L = 0.1$ . The regular mode reported in the literature consistently corresponds to a Strouhal number in the range of 0.5 to 0.8 [30].

In 1987, Rumsey [32] used a numerical method to predict unsteady flow over different airfoil geometries at high angles of attack. Using a compressible, two-dimensional, Navier-Stokes code, Rumsey computed the flow over a NACA 0012 airfoil, without any imposed perturbation, at a Reynolds number  $Re = 10^6$  and a Mach number  $M = 0.3$ . A low-frequency oscillation ( $St_h \approx 0.02$ ) in the flow was encountered, if a turbulent boundary layer near the leading edge was assumed. For laminar flow at  $Re = 3000$ ,  $St_h$  was found to be independent of the angle of attack over 20 degrees at a constant value of about 0.155.

In 1989, Zaman et al. [33] studied the low-frequency oscillations in the flow over NACA 0012 before stall. A turbulent boundary layer was resolved in a two-dimensional Navier-Stokes code. Details of the flow field and unsteady forces compared reasonably well with the experimental data. This study was explored experimentally as well as computationally for NACA 0012 airfoil with a “glaze ice accretion” at the leading edge [21]. With a Navier-Stokes computation, “limit-cycle” oscillations in the flow and in the aerodynamic forces were observed at low Strouhal number. They found that the occurrence of the oscillation depended on the turbulence model. With respect to the computations, questions remain in the application of turbulence models to separated flows. Nevertheless, they concluded that the essence of the phenomenon can be captured computationally with certain combinations

of the turbulence model, Reynolds number, and airfoil shape [21].

The separation bubble on an airfoil at low Reynolds number behind a simulated leading edge glaze ice accretion was studied experimentally in 1992 [26]. Time-dependent measurements of the flow field were performed for a laminar separation bubble. In 2002 [34], unsteady pressure measurements were performed on NACA 0012 airfoil with two- and three-dimensional leading edge glaze ice accretions. The mean and fluctuating lift coefficients at different angles of attack were presented. Gurbacki noticed the formation of additional vortices in the separated shear layer due to the jaggedness of the three-dimensional ice shapes. The unsteady content of the iced airfoil flow field was further analyzed [35]. The iced airfoil performance and distributed surface pressure were found to be like the unsteady 2D separation bubble in simple geometries. The NACA 0012 airfoil was tested at a high Reynolds number in 2013 [36]. In addition to the clean configuration, the airfoil model was also tested with a set of boundary layer trips, a two-dimensional extrusion of a horn ice shape casting, and an array of simulated icing configurations created using simple geometries. The resulting values of Strouhal number exhibited a dependence on the airfoil angle of attack and corresponded to a range that was consistent with the Strouhal number values reported in prior studies of the low-frequency mode in the literature.

With the above background, the various aspects of the separated flow over a glaze ice have been explored experimentally from 1986 until recently, while the capacities of the numerical computational methods in this area need more clarification. This work studies the performance of URANS simulations in predicting the oscillations over an iced airfoil. It is of interest to see how accurate URANS models estimate the structure and the size of the formed time-averaged vortices in comparison to the measured ones. Furthermore, the accuracy of a two-equation eddy viscosity turbulence model, the SST model, coupled with a URANS model to determine the dynamic load over a glaze-iced airfoil needs to be investigated.

The work presented in this paper is a continuation of a previous work [20], which aimed to determine the aerodynamic performances of wind turbines in icing condition. The main objective of this study is to develop a numerical model to observe and quantify the effect of the unsteady flow over the modeled iced airfoil in the presence of glaze ice. It will help to understand the mechanism by which the dynamic loads are initiated and sustained and their magnitude. The numerical simulations capture the separated shear layer and the structure of large-scale vortices in a turbulent separation bubble.

To this purpose, time-dependent simulations of the spoiler-ice test are performed at different angle of attack [9]. The results are validated with experimental data. Then, the load fluctuations are analyzed at different angle of attack. The frequency of the load cycle is studied as well as the extreme values of the loads acting on the airfoil.

## 2. Materials and Methods

The geometry and boundary conditions are considered from the literature [9, 15]. The experiments were conducted in

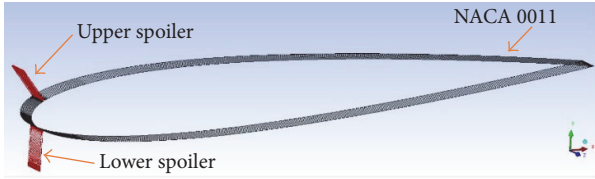


FIGURE 2: Simulated spoiler-ice shapes for NACA 0011.

a single-return closed circuit wind tunnel for a chord Reynolds numbers of  $1.83 \times 10^6$ . The test case was a 0.610 m NACA 0011 airfoil with the spoilers on the upper and lower surfaces.

The experimental mean pressure distribution over the blade surfaces is available for different angles of attack and different spoiler installed angles as well as the lift coefficient, drag coefficient, and pitch moment coefficient.

The fluid problem is solved with the finite volume technique using the CFD code ANSYS CFX 15.0 solver in which the set of equations are the unsteady Navier-Stokes equations in their conservation form [37]. Transient simulations were conducted on the 2D geometry of the NACA 0011 previously described.

High-resolution advection scheme was selected for the spatial discretization and second-order backward Euler scheme was applied for the temporal discretization of the equations. The time step size is set to  $3.5e-5$  seconds based on a time step size analysis prescribed in [20].

SST model with automatic wall function was activated to model the turbulent flow. The  $k-\omega$  SST model appears to be an accurate turbulence model for boundary layer detachment prediction [31, 38]. Symmetric boundaries in a 2D model, as used for these computations, limit the application of more detailed model such as Detached Eddy Simulation model or Scale-Adaptive Simulation [39].

The computational domain has the same dimensions as the test section of the wind tunnel, 2.13 m high, 3.05 m wide, and 3.66 m long. The spoiler angle is set to  $-40^\circ$  and  $0^\circ$  for the upper ( $\theta_U$ ) and lower ( $\theta_L$ ) one, respectively (Figure 2). To approximate the horn heights of 22.5 min glaze ice accretions, the spoilers are 3.81 cm. Because the blade geometry and the spoilers have a constant cross-test section, symmetry boundary conditions are used at both sides of the created 2D model. The spoiler walls boundary conditions are defined as no-slip walls as well as the top and bottom walls of the wind tunnel. Flow is assumed to have a uniform velocity at the inlet and is allowed to move backward at the outlet.

The convergence criterion was set to a root-mean-squared value of  $10^{-6}$ . The simulation continued until a periodic variation was achieved for the drag, lift, pitching moment, and surface pressures. Due to the lift force fluctuations with time, a large number of iterations for the convergence of the mean value are needed. Computations were performed in order to assess the ability of the present method to accurately predict steady and unsteady airfoil behavior both below and above maximum lift conditions.

The surface pressure is computed on the upper and lower surfaces of the airfoil, from the leading edge to the trailing edge. In one cycle of the load oscillations, the pressure

distribution is recorded, and the averaged value is used as the mean pressure distribution. The dynamic pressure ( $P_d = 0.5\rho U_\infty^2$ ) is used to nondimension the mean pressure and to define the pressure coefficient ( $C_p = P/P_d$ ), where  $P$  is the static pressure.

For each time step, lift and drag forces are calculated as the loads over the iced airfoil, including the spoilers. The lift and drag coefficients ( $C_L$  and  $C_D$ ) are defined by dividing the respective force by the reference area ( $A$ ) and  $P_d$ . The reference area is calculated from the airfoil chord length ( $c$ ) and the span thickness, which in a 2D case is the thickness of the layer cell that is modeled. The pitching moment  $C_M$  is calculated with respect to the quarter chord location as reported in the experimental tests. The moment is normalized using  $P_d$ ,  $A$ , and  $c$ .

In the calculation of the Strouhal number, the spoiler-iced airfoil projected height at each angle of attack is considered as " $h$ " in  $St_h$ . Because the separation bubbles cover almost the entire blade surface from the spoilers to the trailing edge, the chord length is also considered as a rough magnitude of the bubble length " $L$ " in  $St_L$ .

**2.1. Mesh Analysis.** A multiblocking mesh consisting of hexahedral elements is generated. Grid topology of C-type was used to generate high quality structured hexahedral grid using the code ICEM CFD. The value of  $y^+$  corresponding to the first grid point above the walls is set below one. The mesh is denser on the spoilers and the airfoil surface to resolve the boundary layer formed on these parts.

Before the simulations were performed at different angles of attack, mesh scaling tests and mesh performance tests were carried out. After the mesh scaling test, a total of 1.7 million hexahedral mesh elements were created. A preliminary mesh containing 0.41 million hexahedral elements was generated and refined around the airfoil and spoilers to maintain  $y^+ < 1$ . Both sides of each spoiler need a different level of refinements as the dimensionless distance  $y^+$  depends on the wall shear stress as well as the size of the first cell normal to the wall. The wall shear stress value is found different at each side of the spoilers as the flow is different on each side.

The mesh analysis is performed keeping the initial condition and the number of processors used. However, these parameters have shown some effect on the numerical solution. The mesh resolution is studied by resolving the mesh uniformly in all directions. Load coefficients have been considered as the key parameters. Four grids were used consisting of 0.41, 0.93, 1.7, and 3.9 million elements.

The simulation results are plotted in Figure 3. The accumulated value of the lift converges after a large number of iterations. The drag value was not found sensitive to the mesh density, not plotted here. The numerical uncertainty due to the mesh density is calculated based on three mesh densities (Table 1) as suggested in [40]. Three different grid densities (fine,  $N_1$ ; medium,  $N_2$ ; and coarse,  $N_3$ ) were used for the scaling test.

Table 1 shows the computed parameters based on the procedure described in [40] to determine the GCI. 2% difference between the medium and fine grid results was observed. The

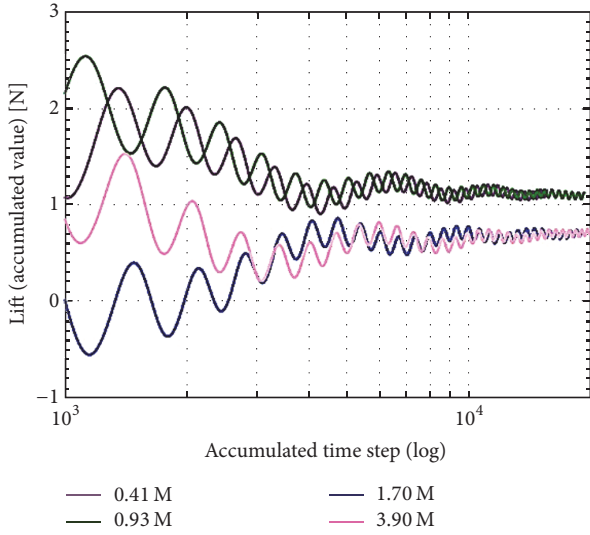


FIGURE 3: Accumulated mean values of the lift force for 4 different mesh densities consisting of 0.41, 0.93, 1.7, and 3.9 million elements.

TABLE 1: Discretization error for iced airfoil in a transient simulation.

Simulation type	Transient (2D)
Criteria parameter	Lift coefficient ( $L$ )
The number of elements in the mesh ( $N_1, N_2, N_3$ )	0.41, 1.7, 3.9
The refinement factor ( $r_{21}, r_{32}$ )	1.32, 1.61
The relative error ( $e_a^{21}, e_a^{32}$ ) (%)	40, 2
Numerical uncertainty in the fine grid solution (GCI) (%)	$1.02E - 4$

converged solution obtained using the medium grid (1.7 M) was used in the subsequent simulations at different angle of attack.

### 3. Results and Discussion

**3.1. Mean Value Study.** Mean pressure distributions are shown in Figure 4 and compared to the experimental results of Papadakis et al. [9]. At the leading edge ( $x/c = 0$ ), the pressure coefficient is greater than one (1.06) for the simulations in all angles of attack. The 6% extra amount of energy comes from the content of static pressure at the inlet, in addition to the dynamic pressure. Assuming a zero-pressure flow at the exit of the experimental test section, a nonzero pressure ( $\sim 150$  pa) is necessary to overcome the viscous losses with a uniform velocity of 45 m/sec.

In a clean airfoil at  $\alpha = 0^\circ$ , just after the stagnation point the flow speeds up on both upper and lower surfaces. The maximum pressure is reached at the leading edge as the stagnation point, and then the pressure switches to the suction passing through the nose of the airfoil. The term ‘‘suction’’ is used to indicate a pressure lower than the reference pressure. Regarding the airfoil camber, the maximum suction occurs around  $x/c = 0.1$  in which the flow has the highest velocity. Then, the velocity decreases, restoring the pressure

at 85% of the chord length, and leaves the trailing edge with a positive pressure.

When it comes to the iced airfoil, the flow acceleration is different at the nose of the airfoil. Since the pressure distribution does not follow the pattern of the pressure distribution on the clean airfoil, the flow is not following the curvature of the airfoil; that is, it is separated. Comparing to the clean case, more suction emerges on both sides (upper and lower surfaces). It also confirms that the flow is following a path with a bigger curvature than the airfoil nose, which is a vortex perimeter. Based on the experiments, the flow speeding continues up to  $x/c = 0.08$  and 0.1 for upper and lower surfaces, respectively. The pressure distributions are not symmetrical anymore and the upper surface is under higher suction. Then the suction magnitude of the flow starts to remain constant. It shows that the flow has just passed the corner of the oval shape vortex and is going to traverse the above part of the vortex. As long as the pressure coefficient is constant, the thickness of the oval vortex is unchanged.

Although the flow reaches almost the same amount of suction as the experiments, the simulated flow separates immediately at  $x/c = 0.02$ , where the flow encounters the spoilers. It can be concluded that the simulation captures accurately the height of the vortex but the maximum thickness of the vortex is obtained closer to the leading edge. As the pressure remains constant, the vortex shape does not have any curvature and the flow is passing over a straight path. At around 35% of the chord length, the flow starts to decelerate on the airfoil upper surface. This shows that the flow is descending the right-side curvature of the oval vortex which is getting thinner. In the simulations, this phenomenon occurs at around 45% of the chord which means the width of the vortex is overpredicted. Experiment shows that the flow is reattached at around  $x/c = 0.7$  as it is following the same slope of the pressure distribution on the clean airfoil. In the simulated model, the flow does not reattach completely before getting to the trailing edge. Close to the trailing edge, the flow follows a similar path to the airfoil that shows the separated region has become narrow though not reattached yet.

On the lower surface, the flow reattaches at around  $x/c = 0.75$ , while in the simulation a long bubble extends to the airfoil trailing edge with a constant pressure coefficient. The simulated vortex is like a wide oval with a uniform height from leading edge up to 80% of the chord length. The uniform shape of the vortex can relate to the zero angle of the spoiler on the lower surface ( $\theta_L = 0$ ), while on the upper surface the vortex tends to follow the bend of the spoiler to the left ( $\theta_U = -40$ ) and so the pressure coefficient does not remain constant. In the last 3-4% of the chord length ( $x/c \sim 0.96$ ), a vortex emerges just close to the trailing edge on both sides of the airfoil surface. That is the vortex shedding which transmits downstream and will be discussed later in this paper (see Figure 10).

At  $\alpha = 4^\circ$ , more suction magnitude is seen on the lower surface than the upper surface. It is in opposite to the flow at  $\alpha = 0^\circ$ . For the clean airfoil at a positive angle of attack, the lower surface is windward. So, the leeward flow on the upper surface has more suction. But in the case of iced airfoil, the separated flow reaches more suction on the lower surface

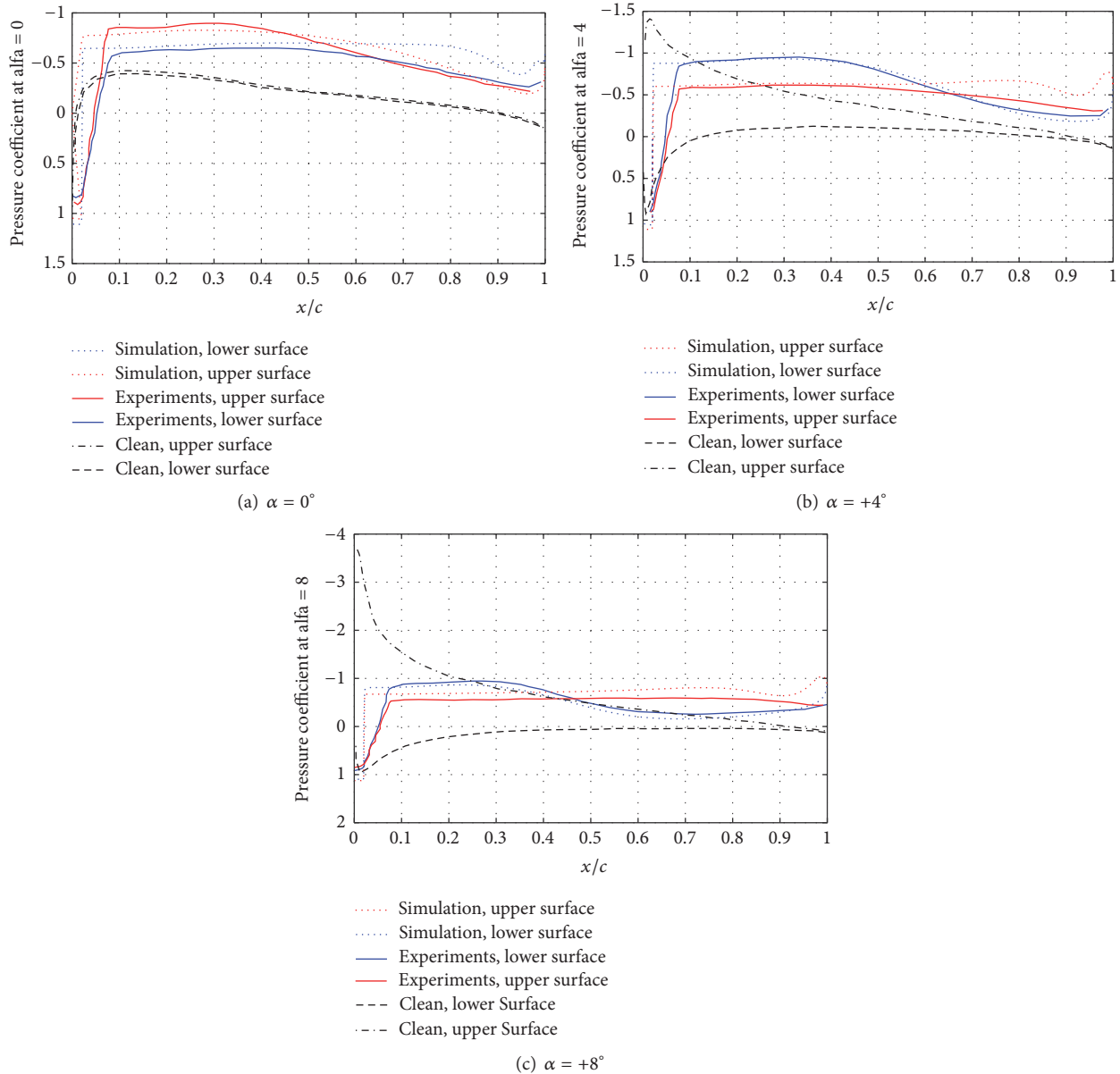


FIGURE 4: Surface pressures from leading edge to the trailing edge at different angles of attack (the experimental data of pressure distribution is available for only the three mentioned angles of attack) (scale of y-axis is different to enable clarity in slope).

at the separated region. Therefore, a negative lift is produced at 58% of the chord length based on the experiments (from  $x/c = 0.08$  to  $0.65$ ). The lift is then positive until the last 4% ( $x/c = 0.96$ ) where the trailing edge vortex is formed. The simulated vortex on the lower surface starts further than in the experiments but has the same form when it continues. The vortex on the upper surface is reattached at  $x/c \cong 0.65$  while it extends to the trailing edge in the simulated flow.

At  $\alpha = 8^\circ$ , there is no suction on the lower surface of the clean airfoil, while a high suction is seen on the leeward upper surface. That is the source of a large positive lift at this angle of attack. When it comes to the iced airfoil, there is a negative lift from the leading edge up to  $x/c = 0.45$  and then the lift direction changes to positive, which is further discussed later.

At  $\alpha = 8^\circ$ , the flow on the lower surface does not reach the same suction as in the experiments. It means that a smaller vortex is modeled in the simulation. Although it is formed further down and its thickness is smaller than the experiments, the form and the curvature of the oval vortex are modeled similarly. Regarding both experiments and simulation results, the flow will not reattach on the lower surface and it extends to the trailing edge. On the upper surface, there is a wide uniform bubble that extends almost all over the airfoil length up to the trailing edge vortex. More suction is seen in the simulated vortex which means the vortex size is overestimated. Furthermore, it turns at  $x/c = 0.8$  and then the trailing edge vortex forms at  $x/c = 0.9$  which is also much bigger than the experimental results.

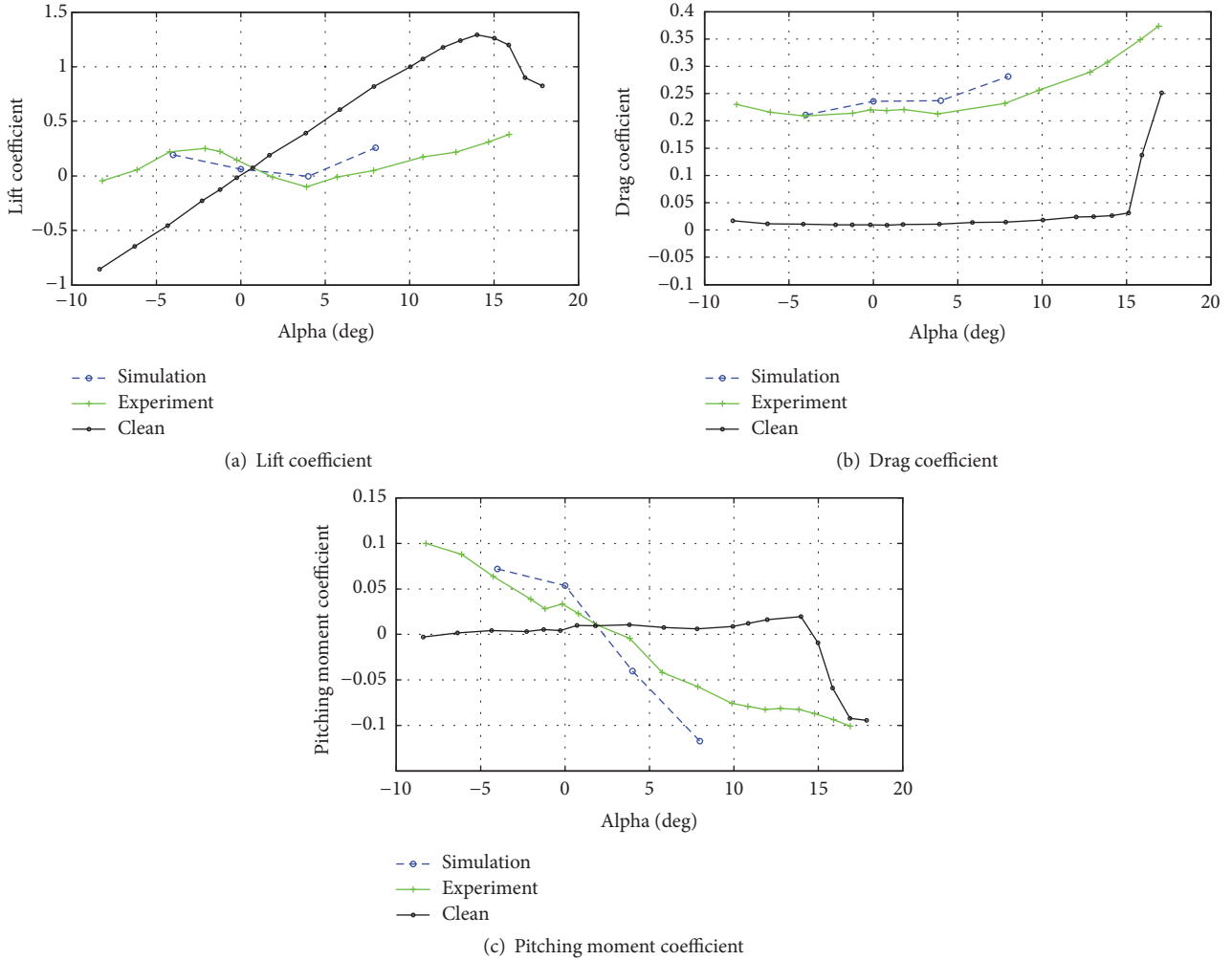


FIGURE 5: Load coefficient of the iced airfoil in different angles of attack.

The load coefficients are shown in Figure 5 regarding the mean value of the loads. It will be discussed in the following section.

**3.1.1. Lift Coefficient.** Lift performance for the clean and iced airfoil is presented in Figure 5(a). Although in a clean airfoil, a higher angle of attack results in more lift; a different trend is seen in the case of glaze-iced airfoil.

For the clean airfoil, the angle of stall is  $15^\circ$  with corresponding maximum lift coefficients of 1.4 for Reynolds number of 1.83 million. The lift coefficient remains linear with the angle of attack up to approximately  $10^\circ$  [9]. The 3.81 cm spoiler-ice shapes at 2% chord on the upper and lower surfaces result in a considerable change in the lift coefficient. These changes include lift sign reversal at low angles of attack while large reductions in the lift and a reduction in the lift slope are observed at higher angles of attack.

The lift sign reversal can be explained by the pressure distribution presented in Figure 4. At  $\alpha = 0^\circ$ , regarding the experiments, in most of the chordwise parts there is more suction on the upper surface than the lower surface which

results in a positive lift (Figure 4(a)). From  $x/c \cong 0.65$  to the trailing edge, although there is more suction on the lower surface, the difference between the lower and upper surfaces is very small. So, there would be a positive lift on the entire airfoil (Figure 5(a)). In the simulated flow, the bubble on the lower surface has an oval shape with almost uniform height since the suction magnitude is almost constant ( $C_p \cong 0.6$ ), while in the experiments the oval-shaped bubble seems to be thinner near the extremities. It leads to a higher negative lift on the later 35% of the chord length compared to the experiments. In summary, the lift on the airfoil is around zero based on the simulations, though still positive (Figure 5(a)).

At  $\alpha = +4^\circ$ , there is a negative lift in the first 57% of the chord length based on the experiments (Figure 4(b)). Then, the reattachment process on the lower surface decreases the suction magnitude and a positive lift is obtained, while the negative part is dominant and the net lift on the airfoil is negative (Figure 5(a)). In the simulated flow, the bubble on the upper surface is more flat compared to the experiments and it keeps the constant suction of  $C_p \cong 0.6$ . Thus, more positive lift is obtained over the later 40% of the airfoil length that compensates for the negative lift over the rest of the airfoil

and the net lift is around zero. The curvature of the clean airfoil is designed to generate a very low suction on the lower windward side at  $\alpha = +4^\circ$  (Figure 4(b)), which is increased due to the accreted ice. Also, the slope of suction decrease is different on the upper leeward side at the iced airfoil. It shows that the flow does not follow the curvature of the airfoil; that is, it is detached. It results in more lift loss comparing to zero angle of attack. At  $\alpha = +8^\circ$ , the high pressure on the windward side of the clean airfoil (Figure 4(c)) results in a big lift magnitude (Figure 5(a)).

At the iced airfoil, flow separation leads to lift sign reversal on the first 47% of the airfoil (Figure 4(c)). Then the flow reattachment processes on the lower side decrease the suction. Since the upper surface is still on a constant suction, a positive lift is obtained over this part of the airfoil which dominates the negative lift, and the net lift is positive. More lift in the simulated flow (Figure 5(a)) comes from the fact that the vortex on the upper surface is overestimated leading to a higher level of suction ( $C_p \cong -0.67$ ) compared to the experiments ( $C_p \cong -0.56$ ) (Figure 4(c)). It results in a larger difference between the upper and lower surface suctions, that is, more positive lift.

It seems that although the lift is increasing with increasing the angle of attack above  $4^\circ$  in both clean and iced airfoil, lift loss is too much due to the spoilers.

**3.1.2. Drag Coefficient.** For the clean 0.61 m NACA 0011, the lowest drag coefficient was in the range of 0.008–0.009 near  $\alpha = 0^\circ$ . Near stall, the drag coefficient reached a value of about 0.03 as shown in Figure 5(b). For the iced airfoil, the increase in drag was in the range of 1000% to 2000% with respect to the clean airfoil for angles of attack between 0 and 14 degrees [9]. In the simulated flow, the drag is even larger due to the overestimation of the bubble sizes as described.

In both the iced airfoil and the clean airfoil, the drag increases when the angle of attack becomes larger than  $4^\circ$ . However, the slope is higher in the situation of the iced airfoil. Therefore, it is not justified to have an iced airfoil operating at a higher angle of attack because the gain in the lift implies a rapidly increasing drag. In the case of the clean airfoil, a higher angle of attack (up to the stall) would be recommended since it would provide more lift without extra drag.

The drag coefficient is almost the same at  $\alpha = 4^\circ$  and  $\alpha = 0^\circ$ , while it increases at  $\alpha = 8^\circ$ . Looking at Figure 4, it can be seen that in all of the three cases there is a bubble extending all through the airfoil surface (with a constant suction) and another bubble that becomes thinner in the reattachment process. Considering the curvatures of the pressure distributions, the first bubble is similar at  $\alpha = 4^\circ$  and  $\alpha = 0^\circ$ , while it is less elongated and reattaches faster in the case of  $\alpha = 8^\circ$ .

**3.1.3. Pitching Moment Coefficient.** Clean airfoil pitching moment coefficients at 25% of the chord length location are presented in Figure 5(c). Positive pitching moment was observed for angles of attack in the range 0 to 15 degrees, indicating that lift force was acting ahead of the 25% chord point [9]. The variations are very small when the angle of attack is increasing. The effects of the spoiler-ices on the

pitching moment characteristics of the airfoil are presented in Figure 5(c). A large deviation from the clean airfoil pitching moment is observed, including a sign reversal throughout the range of angle of attack.

The gap between the simulated flow and the experiments comes from the different positions of the vortices as previously described. Based on the pressure distributions, the different positions of the formation and reattachments of the vortices lead to a different force distribution with respect to the quarter chord point. This is the reason for the gap between the experiments and the simulations, while both the experiments and simulation results show that a higher angle of attack leads to a large pitching moment coefficient which is not desired.

From all the investigated cases, the simulation performed for the largest angle of attack,  $\alpha = 8^\circ$ , showed the least agreement to the experimental data. Figure 7 helps to understand the flow behavior at this angle of attack. The turbulence kinetic energy ( $k$ ) is shown for  $\alpha = 0^\circ$  and  $\alpha = 8^\circ$  as it is a representative of the turbulence intensity or turbulence level ( $I$ ). Both plots are extracted at a time step in which a high positive lift occurs (6.7 [N] for  $\alpha = 0^\circ$  and 5.9 [N] for  $\alpha = 8^\circ$ ). The turbulence level looks higher at a higher angle of attack. It is seen that a large turbulent wake arises at the trailing edge which is originated from the upper surface of the blade at  $\alpha = 8^\circ$ . This wake is not damped at the modeled downstream domain.

The pressure distribution also confirms the presence of a large turbulent wake (Figure 4(c)). The trailing edge vortex shedding forms at  $x/c \cong 0.92$  which is farther from the trailing edge compared to the cases ( $x/c \cong 0.95$  at  $\alpha = 0^\circ$  and  $x/c \cong 0.94$  at  $\alpha = 4^\circ$ ). The vortex induces a suction magnitude of  $C_p \cong -1.06$  that is twice the suction magnitude of the trailing edge flow at  $\alpha = 0^\circ$ , for instance. Therefore, the shedding vortex is wider and thicker for this case which leads to a higher turbulence intensity at the trailing edge and consequently downstream.

The presented computational versus experimental mean flow analysis enables validating the current simulation. The following results are from computations only and are assumed to reproduce flow physics correctly. The general characteristics are validated towards the features of similar iced airfoils reported in the literatures.

**3.2. Time-Dependent Study.** Usually, flow field studies of separation bubbles are focused on the time-averaged characteristics. However, the bubble flow fields are known to have strong unsteady characteristics that also play a role in the aerodynamic characteristics [14]. These unsteady features are now discussed.

The streamlines around the iced airfoil illustrate that the vortices form and move over the airfoil surface. Consequently, the pressure on each point of the airfoil surface changes with time as the vortices are formed and convected. It causes the lift to oscillate from positive to negative repeatedly, leading to a dynamic loading of the airfoil.

The instantaneous pressure values are shown in Figure 7 for some random points on the lower and upper surfaces of the airfoil upstream and downstream of the spoilers. The plots

represent the pressure on these points on the airfoil at a zero angle of attack during 0.07 s of the simulation time, consisting of around 2000 iterations (the simulation time is normalized by the time step value, i.e.,  $3.5 \times 10^{-5}$ ). The frequency of the pressure is almost the same for all the points. This frequency is illustrative of the roll-up of spanwise vortices in the shear layer above the recirculating region and their shedding downstream of the separated zone. Closer to the trailing edge the amplitude of the pressure increases. This can be related to the vortices shedding downstream of the trailing edge.

Upstream of the spoilers (points 1, 2), there is a high positive pressure which is almost constant during the time. As it will be later shown in Figure 11, these points are located in the upstream quasi-stagnant vortices; thus the pressure is high and the time variations of the pressure are very small. Downstream of both spoilers, the pressure is negative as there is a suction underneath the formed vortices.

It is observed that for each pair of points with the same chordwise location, that is, 3-4 and 2-5, the pressure oscillations are out of phase. This indicates that the vortices are forming and leaving the airfoil surface in a periodic manner.

Because of the pressure fluctuations on the airfoil, the loads fluctuate. The integrated load time history is shown in Figure 8 for the simulated cases. The drag variation is smaller than the lift variation. It indicates that the vortices distribution is shifting more frequently between the upper and lower surfaces, affecting mostly the vertical loads. However, both drag and lift oscillate at a similar frequency.

At  $\alpha = 0^\circ$ , a bimodal frequency pattern is seen in the drag force, with the maximum drag varying cyclically between two values (at two directions), while there is a quasi-sinusoidal trend of the variations for the other cases; that is,  $\alpha = -4, +4$ , and  $+8^\circ$ .

The drag time history indicates that, for  $\alpha = 0^\circ, +4^\circ$ , and  $+8^\circ$ , the maximum drag corresponds almost to the maximum lift and the minimum drag occurs near the minimum lift. At  $\alpha = -4^\circ$  the trend of the variations is inverted; that is, increasing in the lift is related to a decrease in the drag and vice versa. The pitching moment oscillations follow the lift variations not the drag, because the lift variations amplitudes are bigger than the drag fluctuations. Thus, the lift is the determinative component of the pitching moment direction.

The computed mean values of the load coefficients are replotted in Figure 9 with corresponding range of the variations and the Strouhal numbers. Only the mean experimental load values are available for the modeled geometry. As previously observed, the calculated frequency of the fluctuations is similar for the vertical and horizontal forces. The amplitudes do, however, differ between the cases.

As mentioned,  $St_h$  is calculated based on the spoiler-iced airfoil projected height  $h$ . The slight difference between the  $St_h$  number of different angles of attack relates to different projected heights higher in  $\alpha = 8^\circ$ , though the frequency is almost the same. Then, there is a direct relationship between the air-projected height of the iced airfoil and the  $St_h$ , while the amplitude of the oscillations does not correlate. Considering the separation bubble length as the length scale, the mentioned Strouhal number ( $St_h$ ) converts to  $St_L$  ranging from 0.59 to 0.69 for different angles of attack. This

corresponds to the shedding motion of the separation shear layer. It is consistent with the Strouhal number of regular mode for the same airfoil with a horn ice reported by Ansell [30]. Gurbacki [35] also reported similar range of  $St_L$  (0.53–0.73) with a 3D horn ice shape.

Bigger “ $h$ ” value can be the source of more turbulent flow, that is, higher  $k$  magnitude, at  $\alpha = 8^\circ$  (Figure 6). It led to a larger trailing edge vortex shedding that was discussed before. It can be concluded that a higher turbulence intensity does not result in a higher amplitude of the oscillations.

The maximum amplitude of the lift fluctuations corresponds to zero angle of attack (Figure 9(a)). As mentioned, the lift force fluctuates between the negative and positive values at  $\alpha = 0^\circ$ . Flow behavior is analyzed in the following paragraphs for each case of negative, positive, and zero lift values. For the simulation of the flow at zero angle of attack, the vortices shapes at two time steps are shown in Figure 10. The time steps are selected with a half-period interval, in which the lift coefficient switches from a maximum positive to a minimum negative value.

Near the leading edge, a stagnation region arises, at which the flow is split into two bunches going to the upper and lower surfaces of the airfoil. They reach each other again near the trailing edge. Since the airfoil surface is covered thoroughly by the vortices, the streamlines on the upper and lower surfaces should traverse over the borders of the rotating flow regions. When there are two rotating bubbles on one side of the airfoil, the dead flow occupies a larger area. Consequently, the first active streamline should pass through a longer path. This path is considered from the splitting point upstream to the stagnation point downstream of the airfoil. Longer path leads to a higher velocity for the flow.

When the single bubble is on the upper surface (Figure 10(a)), the flow is slower at that side. This results in a higher pressure compared to the lower surface. The consequent higher pressure (less suction) on the upper surface justifies the negative lift. The reverse process happens in the case of positive lift (Figure 10(b)). The bubble configuration shifts and the stagnation point moves resulting in a shorter path for the lower streamline at another instant.

With similar arguments, the lift force becomes positive. These variations repeat periodically inducing a periodic variation of the lift force (Figure 8).

Previously, in this paper, the flow path was described regarding the pressure distribution and the approximate form of the separated region. Figure 10 indicates that the prescribed oval shape of the separated region may consist of more than one vortex.

Moreover, there are some fluctuations in the flow velocity downstream of the airfoil due to the shape and the location of the upstream vortices; that is, the vortices movement at the separation region affects the downstream flow where they are shedding. A similar period is obtained far downstream; that is, the fluctuations in the pressure and the velocity propagate at least four chord lengths downstream the iced airfoil which is modeled in this simulation. So, in practice, it can cause a periodic inlet velocity upstream of a neighbor wind turbine at wind farms. Therefore, for a wind farm in which the distance between the wind turbines is designed to be 3–10

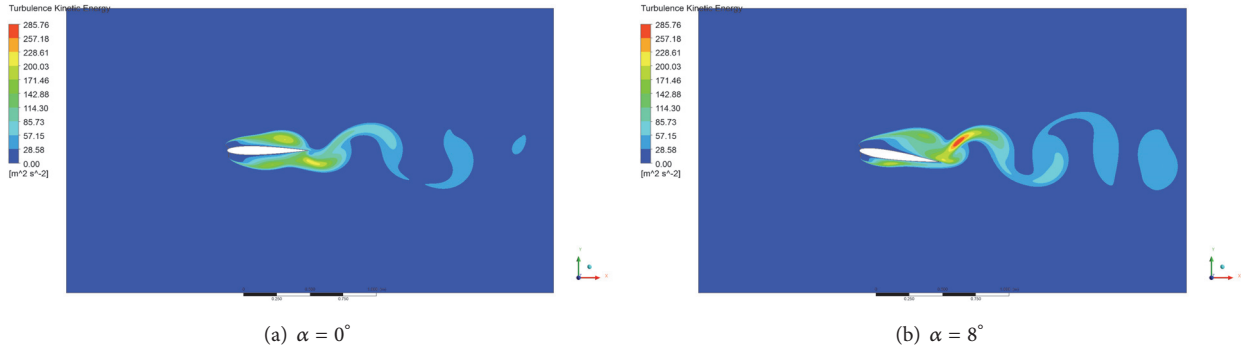


FIGURE 6: Turbulence kinetic energy contour in zero- and eight-degree angle of attack.

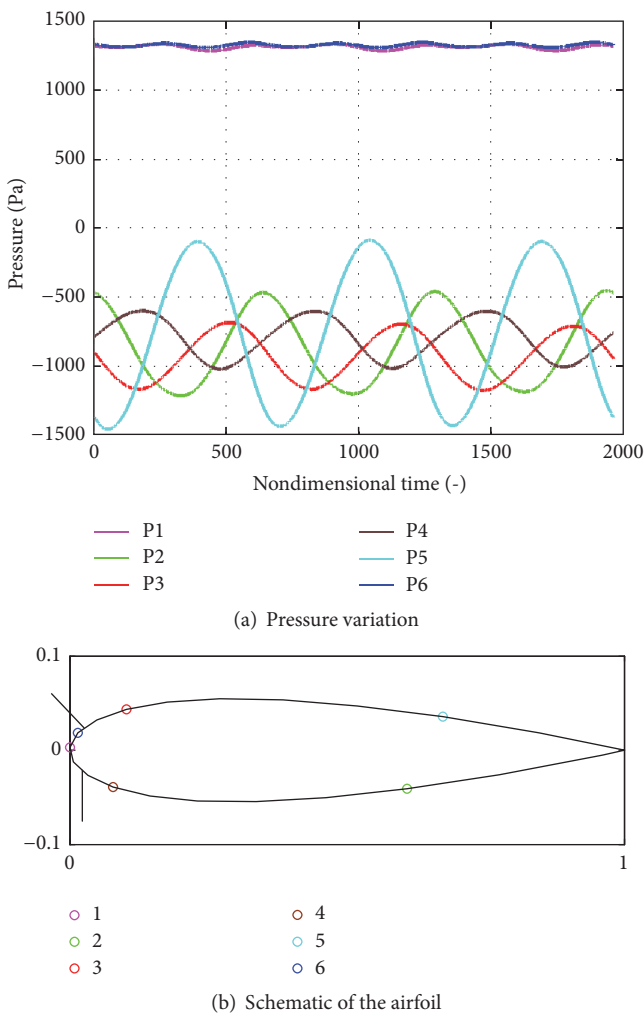


FIGURE 7: Instantaneous pressure variation of points on the pressure and suction sides.

rotor diameters, the icing effect should be considered as it may make time-varying instabilities downstream of the rotor.

Figure 11 shows streamlines in the proximity of the spoiler-ice, highlighting a multitude of vortices. It is an instant at which almost no lift is generated. The flow upstream

of the spoilers forms a bubble in the corner between the spoiler-ice and the airfoil surface.

With the application of a RANS turbulence model these vortices are captured at the upstream of both upper and lower spoilers. The flow divides at the upstream face of the spoiler-ice and part of the flow is diverted to the upper spoiler while the remaining flow goes over the tip of the lower spoiler-ice and forms shear layers. These shear layers play a significant role in the generation of the downstream primary and secondary vortices as these vortices are clearly seen.

As the low speed rotating flows fill the region downstream of the spoilers, the airfoil surface is covered thoroughly by the vortices. Thus, the axial flow which was supposed to act on the airfoil surface to generate the lift force does not meet the airfoil surface at all. With the existing ice horn height, the designed curvature of the NACA0011 does not create any lift, as the flow is following the path formed at the boundary of the vortices instead.

Furthermore, although the integrated value of the vertical force on the iced airfoil is zero at the illustrated moment, there is a shedding vortex that initiates upward from the trailing edge (not shown here). Therefore, it is observed that even with a zero lift there is no symmetrical load distribution on the airfoil, and the downstream flow is oscillating.

As described in the literature, shear layer flapping is typically observed at very low frequencies, when compared to the characteristic frequencies of most other flow phenomena. A lower frequency cycle beside the main oscillations was observed when considering a long-time history. The related frequency is about 1/7 of the regular mode frequency, with the value giving  $St_h \approx 0,02$  at  $\alpha = 8^\circ$  that is in consistent with the range of values reported in the literature for the simulated glaze ices [21, 26, 30].

#### 4. Conclusions

The main objective of this paper is to estimate the dynamic loads acting over an iced airfoil, as well as studying the structure and dynamics of the turbulent separation bubbles. Ice profile is simulated with the help of spoilers. The simulated separated flow over the sharp spoilers can be considered as a worst test case of load loss due to the icing. It is shown that a glaze ice effect is not limited to a decrease in the lift; it also

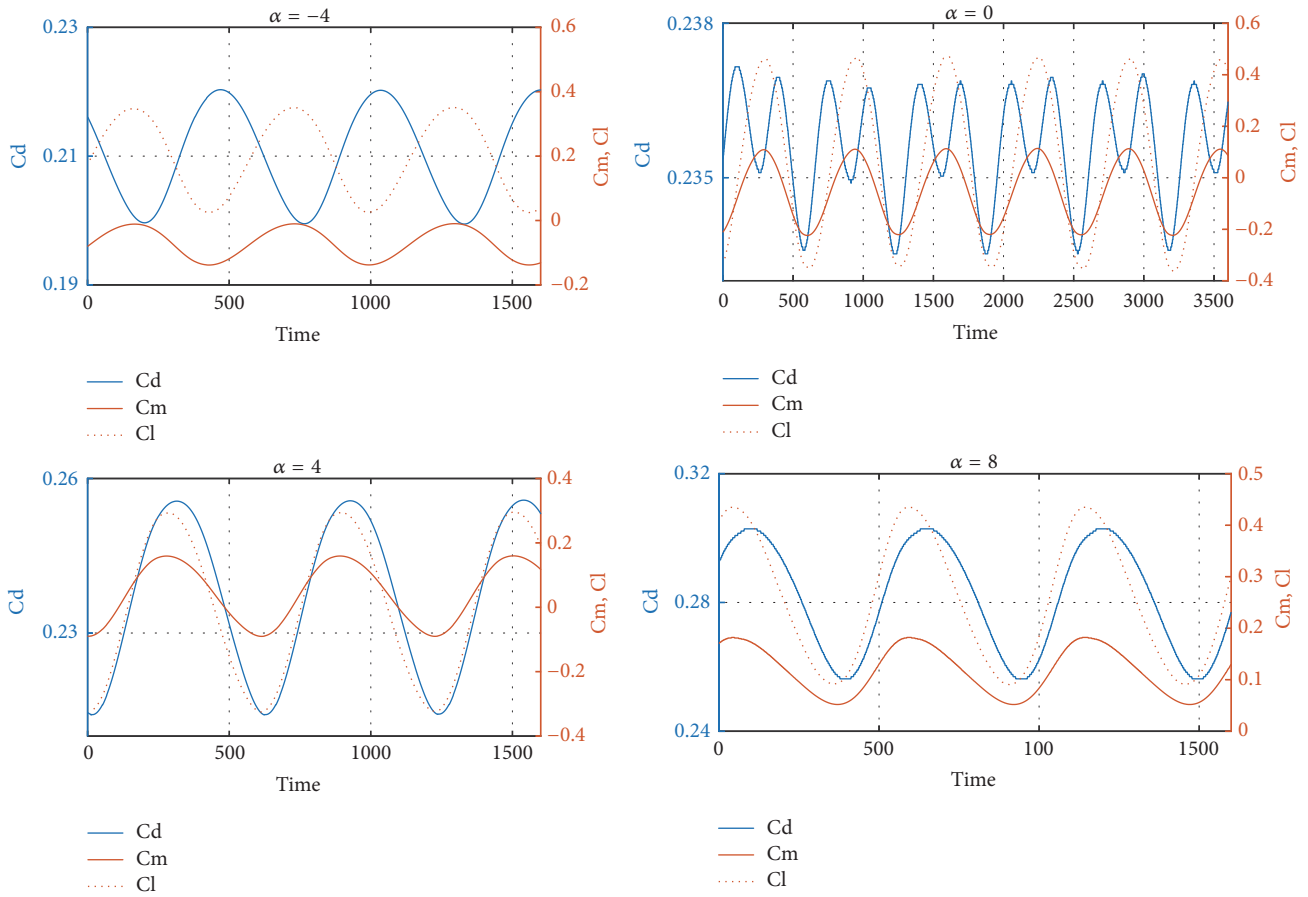


FIGURE 8: Time histories of load coefficients at different angles of attack (a part of the simulation time is shown, and the simulation time is normalized by the time step value, i.e.,  $3.5 \times 10^{-5}$ ).

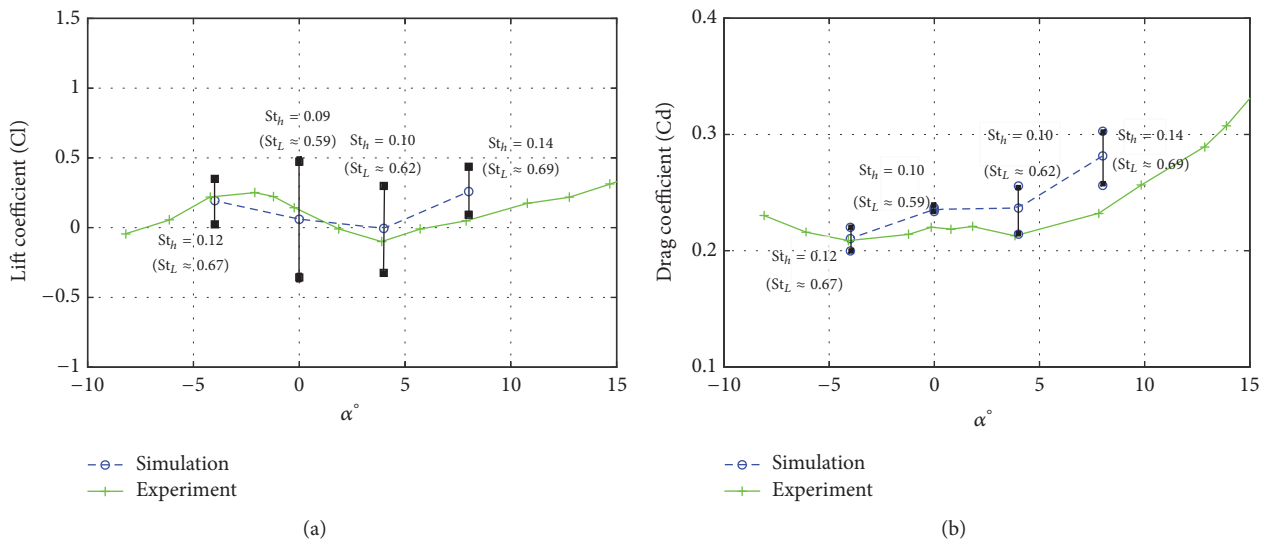


FIGURE 9: Lift (a) and drag (b) coefficient including the amplitude of oscillations (black vertical bars) and Strouhal number of shedding mode.

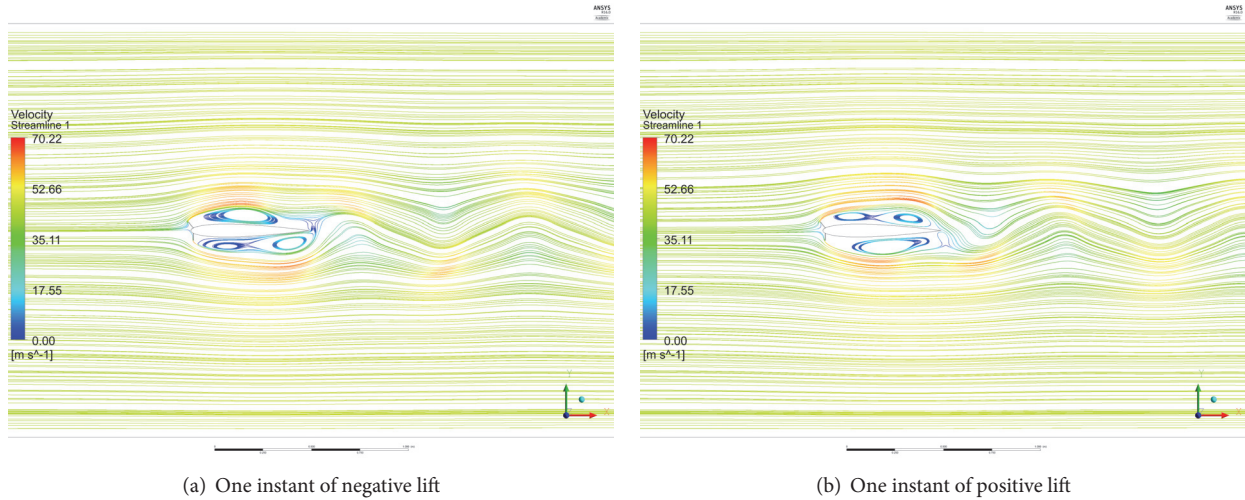


FIGURE 10: Vortices shape at two moments with an interval of half period at zero angle of attack.

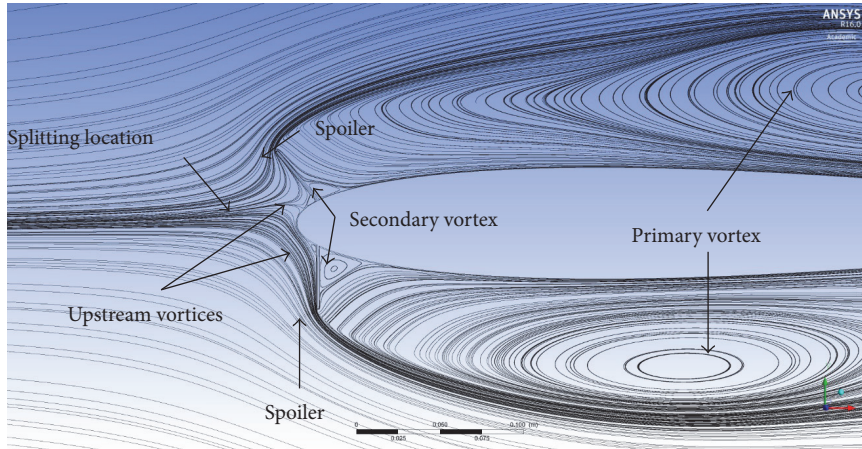


FIGURE 11: Flow streamlines near leading edge at  $\alpha = 0^\circ$ .

imposes some dynamic forces that should be considered in a wind farm, for instance.

Aerodynamic performance coefficients and pressure profiles are calculated and compared with the available measurements for a chord Reynolds number of  $1.83 \times 10^6$  [9, 15]. The separation bubbles formed on an airfoil behind a simulated leading edge glaze ice accretion are studied by URANS. The details of the flow field and the vortex shapes at different angles of attack are investigated based on the mean pressure distributions as well as the instantaneous streamlines. The main conclusions can be summarized as follows:

- (i) The numerical results confirm both time-dependent phenomena observed in previous similar measurements [30]: a low-frequency mode, with a Strouhal number  $St_h \approx 0,013-0,02$ , and a higher frequency mode with a Strouhal number  $St_L \approx 0,059-0,69$ . The higher frequency motion has the same characteristics as the shedding mode and the lower one corresponds to the flapping mode.
- (ii) A greater pitching moment is a consequence of glaze ice beside the decrease of lift. Therefore, a higher angle of attack does not seem to be a good choice of operation in the presence of horn ice as changing the angle of attack to compensate lift loss can increase the pitching moment at the same time. Furthermore, the drag increases considerably.
- (iii) It is seen that the frequencies of the oscillations are almost the same for all angles of attack. There is a direct relationship between the iced airfoil projected height and the Strouhal number  $St_h$ , while the amplitude of the oscillations does not correlate with that.
- (iv) A higher angle of attack leads to a higher turbulence intensity in the flow field, as the airfoil projected height increases.
- (v) The downstream oscillations propagate further downstream at higher angle of attacks.
- (vi) The drag variations in time are much smaller than the lift variation. It means that the vortices distribution is

shifting more frequently between the upper and lower surfaces affecting mostly the vertical loads. However, both drag and lift oscillate at a similar frequency.

- (vii) Considering the load time histories of the simulated cases, maximum lift and maximum drag occur almost at the same time and the variations are in the same direction, while they are reverse at the negative angle of attack.
- (viii) The separated bubbles on both upper and lower surfaces are appearing closer to the leading edge compared to the experiments. In the experiments, the oval shape bubbles seem to be thinner near the extremities, while URANS modeling results in the vortices extending wider over the surfaces with small variation in the suction magnitude.
- (ix) A vortex arises close to the trailing edge at 10% of the chord length. The related vortex shedding is the source of the fluctuations downstream. Reaching more suction in that vortex leads to more fluctuations in the flow downstream.

## Conflicts of Interest

The authors declare that they have no conflicts of interest regarding the publication of this paper.

## References

- [1] S. Barber, Y. Wang, S. Jafari, N. Chokani, and R. S. Abhari, "The impact of ice formation on wind turbine performance and aerodynamics," *Journal of Solar Energy Engineering*, vol. 133, no. 1, Article ID 011007, 2011.
- [2] N. Dalili, A. Edrisy, and R. Carriveau, "A review of surface engineering issues critical to wind turbine performance," *Renewable & Sustainable Energy Reviews*, vol. 13, no. 2, pp. 428–438, 2009.
- [3] V. H. Gray and U. H. Von Glahn, "Aerodynamic effects caused by icing of an unswept NACA 65A004 airfoil," Tech. Rep. 4155, Rep, Washington, 1958.
- [4] F. Villalpando, M. Reggio, and A. Ilinca, "Numerical study of flow around iced wind turbine airfoil," *Engineering Applications of Computational Fluid Mechanics*, vol. 6, no. 1, pp. 39–45, 2012.
- [5] A. Hudecz, *Icing Problems of Wind Turbine Blades in Cold Climates; Icing Problems of Wind Turbine Blades in Cold Climates [Ph.D. thesis]*, Department of Wind Energy, Technical University of Denmark, 2014.
- [6] Z. Wang and C. Zhu, "Numerical simulation for in-cloud icing of three-dimensional wind turbine blades," *SAGE journal*, 2017.
- [7] A. Lacrix and J. F. Manwell, *Wind Energy: Cold Weather Issues*, University of Massachusetts at Amherst, 2000, *Wind Energy: Cold Weather Issues*, University of Massachusetts at Amherst.
- [8] T. Matsuura, M. Suzuki, M. Yamamoto, S. Shishido, T. Murooka, and H. Miyagawa, "Numerical simulation of ice accretion phenomena on rotor blade of axial blower," *Journal of Thermal Science*, vol. 21, no. 4, pp. 322–326, 2012.
- [9] M. Papadakis, S. Alansatan, and S.-C. Wong, "Aerodynamic characteristics of a symmetric NACA section with simulated ice shapes," in *Proceedings of the 38th AIAA Aerospace Sciences Meeting and Exhibit*, 2000.
- [10] X. Chi, B. Zhu, T. Shih, H. Addy, and Y. Choo, "CFD Analysis of the Aerodynamics of a Business-Jet Airfoil with Leading-Edge Ice Accretion," in *Proceedings of the 42nd AIAA Aerospace Sciences Meeting and Exhibit*, 2004.
- [11] M. B. Bragg, "Experimental aerodynamic characteristics of a naca 0012 airfoil with simulated glaze ice," *Journal of Aircraft*, vol. 25, no. 9, pp. 849–854, 1988.
- [12] M. G. Potapczuk, "Numerical analysis of an NACA 0012 airfoil with leading-edge ice accretions," *Journal of Aircraft*, vol. 25, no. 3, pp. 193–194, 1988.
- [13] A. Zanon, M. De Gennaro, and H. Kühnelt, "Wind energy harnessing of the NREL 5 MW reference wind turbine in icing conditions under different operational strategies," *Journal of Renewable Energy*, vol. 115, pp. 760–772, 2018.
- [14] M. B. Bragg, A. P. Broeren, and L. A. Blumenthal, "Iced-airfoil aerodynamics," *Progress in Aerospace Sciences*, vol. 41, no. 5, pp. 323–362, 2005.
- [15] M. Papadakis, S. Alansatan, and M. Seltmann, "Experimental study of simulated ice shapes on a NACA 0011 airfoil," in *Proceedings of the 37th Aerospace Sciences Meeting and Exhibit*, 1999, usa, January 1999.
- [16] S. Lee and M. Bragg, "Effects of simulated-spanwise-ice shapes on airfoils - Experimental investigation," in *Proceedings of the 37th Aerospace Sciences Meeting and Exhibit*, American Institute of Aeronautics and Astronautics, 1999.
- [17] S. Lee and M. B. Bragg, "Investigation of factors affecting iced-airfoil aerodynamics," *Journal of Aircraft*, vol. 40, no. 3, pp. 499–508, 2003.
- [18] A. Broeren and M. Bragg, "Effect of Airfoil Geometry on Performance with Simulated Intercycle Ice Accretions," in *Proceedings of the 41st Aerospace Sciences Meeting and Exhibit*, Reno, Nevada.
- [19] Z.-Y. Jin, Q.-T. Dong, and Z.-G. Yang, "The effect of single-horn glaze ice on the vortex structures in the wake of a horizontal axis wind turbine," *Acta Mechanica Sinica*, vol. 31, no. 1, pp. 62–72, 2015.
- [20] N. Tabatabaei, M. J. Cervantes, C. Trivedi, and J.-O. Aidanpää, "Numerical Study of Aerodynamic Characteristics of a Symmetric NACA Section with Simulated Ice Shapes," *Journal of Physics: Conference Series*, vol. 753, no. 2, Article ID 022055, 2016.
- [21] K. B. Zaman and M. G. Potapczuk, "The Low Frequency Oscillation in the Flow Over a NACA0012 Airfoil with an "Iced" Leading Edge," in *Low Reynolds Number Aerodynamics*, vol. 54 of *Lecture Notes in Engineering*, pp. 271–282, Springer Berlin Heidelberg, Berlin, Heidelberg, 1989.
- [22] W. B. Roberts, "The Effect of Reynolds Number and Laminar Separation on Axial Cascade Performance," *Journal of Engineering for Power-Transactions of the ASME*, vol. 97, no. 2, p. 261, 1975.
- [23] N. D. Sandham, "Transitional separation bubbles and unsteady aspects of aerofoil stall," *The Aeronautical Journal*, vol. 112, no. 1133, pp. 395–404, 2008.
- [24] M. Ahanmiri, *Laminar Separation Bubble: Its Structure, Dynamics and Control*, Chalmers University of Technology, 2011.
- [25] W. B. Roberts, "Calculation of Laminar Separation Bubbles and Their Effect on Airfoil Performance," *AIAA Journal*, vol. 18, no. 1, pp. 25–31, 1980.
- [26] M. B. Bragg, A. Khodadoust, and S. A. Spring, "Measurements in a leading-edge separation bubble due to a simulated airfoil ice accretion," *AIAA Journal*, vol. 30, no. 6, pp. 1462–1467, 1992.

- [27] C. Cuvier, J. M. Foucaut, C. Braud, and M. Stanislas, "Characterisation of a high Reynolds number boundary layer subject to pressure gradient and separation," *Journal of Turbulence*, vol. 15, no. 8, pp. 473–515, 2014.
- [28] M. Kiya and K. Sasaki, "Structure of a turbulent separation bubble," *Journal of Fluid Mechanics*, vol. 137, pp. 83–113, 1983.
- [29] J. Weiss, A. Mohammed-Taifour, and Q. Schwaab, "Unsteady behavior of a pressure-induced turbulent separation bubble," *AIAA Journal*, vol. 53, no. 9, pp. 2634–2645, 2015.
- [30] P. J. Ansell, *Unsteady modes in the flowfield about an airfoil with a leading-edge horn-ice shape [Ph.D. thesis]*, University of Illinois at Urbana-Champaign, 2013.
- [31] A. Ducoin, J. A. Astolfi, F. Deniset, and J.-F. Sigrist, "Computational and experimental investigation of flow over a transient pitching hydrofoil," *European Journal of Mechanics - B/Fluids*, vol. 28, no. 6, pp. 728–743, 2009.
- [32] C. Rumsey, "A computational analysis of flow separation over five different airfoil geometries at high angles-of-attack," in *Proceedings of the 25th AIAA Aerospace Sciences Meeting*, American Institute of Aeronautics and Astronautics, 1987.
- [33] K. B. M. Q. Zaman, D. J. McKinzie, and C. L. Rumsey, "A Natural Low-Frequency Oscillation of the Flow over an Airfoil Near Stalling Conditions," *Journal of Fluid Mechanics*, vol. 202, no. 403, pp. 403–442, 1989.
- [34] H. M. Gurbachi and M. B. Bragg, "Unsteady aerodynamic measurements on an iced airfoil," in *Proceedings of the 40th AIAA Aerospace Sciences Meeting and Exhibit*, 2002.
- [35] H. M. Gurbachi, *Ice-induced unsteady flowfield effects on airfoil performance [Ph.D. thesis]*, University of Illinois at Urbana-Champaign, 2003.
- [36] P. J. Ansell and M. B. Bragg, "Characterization of ice-induced low-frequency flowfield oscillations and their effect on airfoil performance," in *Proceedings of the 31st AIAA Applied Aerodynamics Conference*, 2013.
- [37] ANSYS *CFX-Solver Theory Guide Release 15.0*, ANSYS, Inc., 2013.
- [38] F. R. Menter, "Improved Two-equation K-omega Turbulence Models for Aerodynamic Flows," 1992.
- [39] ANSYS *CFX-Solver Modeling Guide Release 15.0*, ANSYS, Inc., 2013.
- [40] I. B. Celik, "Procedure for estimation and reporting of uncertainty due to discretization in CFD applications," *Journal of Fluids Engineering*, vol. 130, no. 7, pp. 0780011–0780014, 2008.

## Research Article

# Axial Fan Performance under the Influence of a Uniform Ambient Flow Field

Till Heinemann  and Stefan Becker

*Institute of Process Machinery and Systems Engineering, University of Erlangen-Nuremberg, Cauerstr. 4, 91058 Erlangen, Germany*

Correspondence should be addressed to Till Heinemann; [tillheinemann@web.de](mailto:tillheinemann@web.de)

Received 6 July 2017; Accepted 18 January 2018; Published 1 March 2018

Academic Editor: Tareq S. Z. Salameh

Copyright © 2018 Till Heinemann and Stefan Becker. This is an open access article distributed under the Creative Commons Attribution License, which permits unrestricted use, distribution, and reproduction in any medium, provided the original work is properly cited.

In their application to air-cooled condensers, axial fans are often subject to the detrimental influence of ambient flow fields at their inlet or outlet. While effects have been investigated mostly under perpendicular cross-flow conditions on fans operating as part of an array in their target design point, this study aims at examining the integral influence of uniform ambient flow fields on a single axial fan over a wide operating range. For this purpose, a wind tunnel fan test rig has been designed and assessed. Multiple angles between uniform ambient flow field and fan axis are examined in their integral influence on the characteristic curve of two distinct industrial axial fans with varying inlet modifications. Increasingly with the fan flow rate, perpendicular inlet cross-flow was found to always have a detrimental influence on fan performance. The straight bladed fan reacted less sensitively than the forward skewed fan, and the adverse cross-flow influence could be reduced with an inlet guard grille and with short conical shroud extensions. Cross-flow at the fan outlet showed potential static fan pressure increases at low flow rates.

## 1. Introduction

With rising global energy demands and a growing use of solar power around the globe, thermal power plants are increasingly built in arid locations. For a steam turbine cycle process, water scarcity often yields air-cooled condensers (ACC) to be more sensible economically and ecologically than standard water-cooled condensers [1, 2]. Different ACC designs exist [3] and the most standard solution bases on an A-type frame of condenser tubes mounted above a horizontal platform of large diameter axial fans [4]. Arrays of dozens or hundreds of ACC modules are usual [5].

Adequate and reliable cooling of the condenser is essential to optimum plant performance, and so is fan energy consumption itself [6]. Owen and Kröger computed a reduction of the overall ACC cooling flow rate of over 15% at 8 m/s wind velocities, which increased the steam turbine backpressure by over 20% [7], which signifies a serious reduction of total plant power generation. It has been shown that flow detachment at the periphery of the ACC banks is caused by cross-flow under the platform, which is induced by the center fans' intake and natural ambient winds [8–16]. This reduces volumetric

effectiveness of the cooling fans of down to 70% at the ACC perimeter [6, 15, 17–22].

Most of the available experimental and numerical research on the phenomenon is carried out for the applied technical case of an A-frame ACC array [10–12, 14, 22–25]. Early research on a single wall mounted fan was carried out by Thiart and von Backström [23, 24] and on a single fan mounted with its inlet to a pipe section at different angles by Stinnes and von Backström [26].

Although most of the cited works investigate the influence of induced cross-draft on perimeter fans at different platform heights, a comparison can be made of their findings to the uniform ambient flow field of the present work. Based on the Salta model [8], Fourie et al. [22] suggest an empirical curve for the influence of ACC platform height and additional ambient cross-flow on the fan flow rate. The study shows substantial differences in cross-flow influence on fan performance due to fan design, and it points out the importance of fan position in the ACC array, that is, perimeter fan compared to center fans. A gradual decline of the system cooling flow rate was found, resulting in a decrease of around 20% at 9 m/s ambient cross-flow velocity. This may serve as a reference

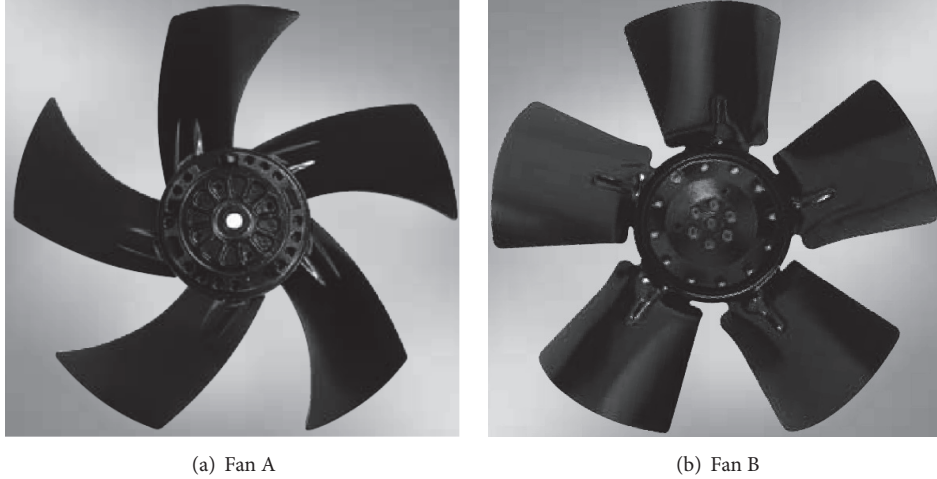


FIGURE 1: Test fans without shroud and guard grille.

figure to the results from the presented work's examination in perpendicular configuration. For individual fans at the ACC perimeter, decreases of 60% to 80% are reported in [22], but they are subject to strong additionally induced drafts from the center fans. Unfortunately, the results and empirical model by Fourie et al. do not translate well to the configuration of this work's approach, where no platform height exists.

The approach of the paper at hand extends the available information by examining single isolated axial fans in an ambient flow environment at various operating points. Thus, the influence of different angles  $\gamma$  between fan axis and ambient flow field (velocity  $U_0$ ) on fan pressure and efficiency curves is elaborated. The novelty of this approach lies in the experimental examination of cross-flow influence on an isolated single axial fan, while eliminating effects caused by neighboring fans and platform height. The presented work attempts to investigate integral fan behavior in a way more abstract from ACC application. It allows insight into fan performance under many different ambient flow field and installation conditions, over a wide range of flow rates (i.e., operating points).

This work aims at examining the influence of different ambient flow conditions at either fan inlet or fan outlet for a forward skewed industrial fan and a straight bladed fan. Installation conditions such as the presence of a concentric guard grille and the intake direction (motor side of the hub at inlet versus rotor side at inlet) are compared, and since shroud extensions have been reported to reduce negative cross-flow influence in ACC simulations [10, 12], the effect of different solid and porous cylindrical and conical inlet extensions is examined too.

## 2. Experimental Setup

**2.1. Wind Tunnel Fan Test Rig.** Inside a Göttinger type wind tunnel test section (2.80 m long, nozzle  $1.87 \times 1.40 \text{ m}^2$ ), the test fans shown in Figures 1 and 2, and described in Table 1, were mounted to a square duct section of  $D_{\text{duct}} \times D_{\text{duct}} = 300 \times 300 \text{ mm}^2$  with either outlet in forced draft (FD) configuration

TABLE 1: Test fans manufacturer's specifications.

	Fan A	Fan B
Blade skew	Forward	None
$\xi_{\text{hub}}$	+20°	0°
$\xi_{\text{tip}}$	+60°	0°
Number of blades	5	5
$D_{\text{fan}}$	298 mm	300 mm
Hub to tip ratio	0.342	0.307
$\dot{V}_{\text{max}}$	0.947 m <sup>3</sup> /s	0.767 m <sup>3</sup> /s
$f_0$ at $\dot{V}_{\text{max}}$	45.0/s	44.2/s
$P_{\sim}$ at $\dot{V}_{\text{max}}$	230 W	180 W
$\Delta p_{\text{ts,max}}$	200 Pa	150 Pa

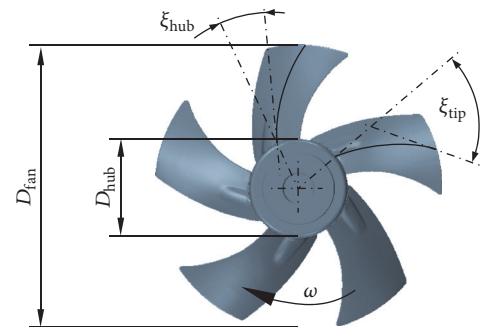


FIGURE 2: Test fan geometry (Fan A).

or inlet in induced draft (ID) configuration. The fan axis was located  $1.5D_{\text{duct}}$  above the test section ground. The experimental setup is shown in Figure 3, with the wind tunnel fan test rig (WFT) mounted to a rotatable platform to realize different angles  $\gamma$  between fan and wind tunnel flow. Fan flow rate  $\dot{V}$  was measured inside a settling chamber using multinozzles as described in ISO 5801 [27]. In Figure 3, the direction of  $\dot{V}$  is indicated for FD operation, and it would be reversed for ID.

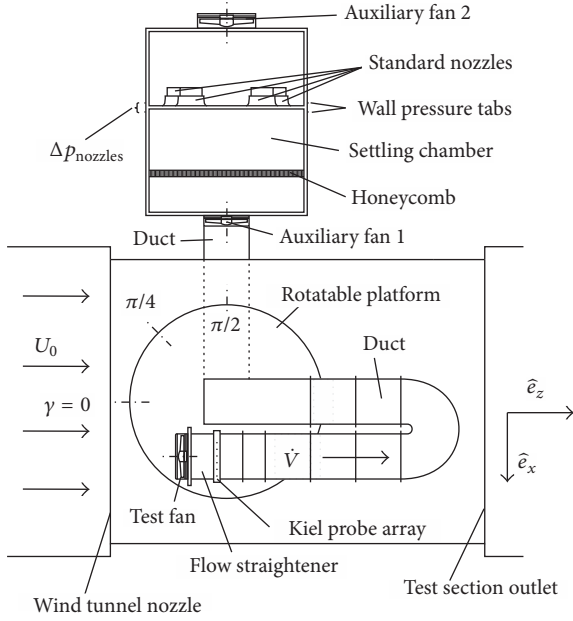


FIGURE 3: Wind tunnel fan test rig.

The test rig was designed to reduce wind tunnel blockage at different angles  $\gamma$ . To facilitate rapid total fan pressure measurements for a large number of operating points and configurations, a custom design array of  $9 \times 9$  Kiel stagnation pressure probes as introduced in [28] was used inside the duct downstream of a  $D_{\text{duct}}/2$  long star shaped flow straightener (FS). This was necessary to reduce the swirl component at the fan outlet and realize flow directions below the critical onflow angles of the Kiel probes. The setup is shown in detail in Figure 4, where the manufacturer guard grille (GG) is in place at the fan inlet, fixing the hub's motor side to the shroud nozzle. This configuration is labeled FD-SI-GG, since the fan stator (motor side of the hub) is located at the inlet (SI), in forced draft operation (duct at fan outlet).

For the configuration without guard grille (noGG), Figure 4 also applies, with the notable difference that only four thin struts fix the fan motor to the shroud, instead of the sketched GG. A mirrored version of the fan with reverse operating direction design allows a rotor inlet (RI) configuration, where the rotating side of the hub is at the fan inlet.

In ID mode, the sketch in Figure 4 applies as well, with the following alternations: the fan flow direction  $\dot{V}$  is reversed by  $180^\circ$ , and so is the orientation of the Kiel probe array. The absence of a considerable rotational velocity component in the duct, which means upstream of the fan inlet in ID also allows for the flow straightener to be omitted. With these three minor adaptations, Figure 4 illustrates the ID-SO-GG configuration, in which the free, motor side fan outlet is covered with a guard grille.

**2.2. Assessment of Uncertainty and Comparability.** Due to the spatial restrictions of the wind tunnel environment, the fan test rig described above was not in accordance with ISO 5801.

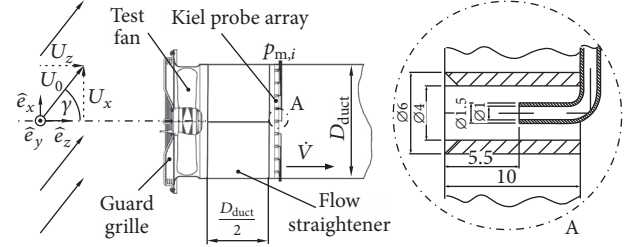


FIGURE 4: Measuring setup with Kiel probe array (FD-SI-GG).

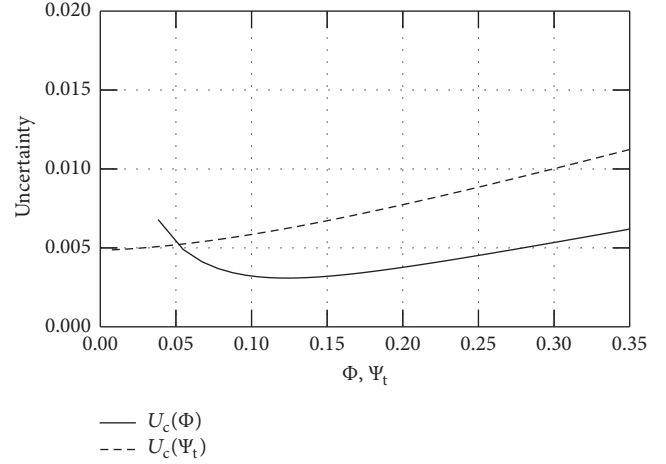


FIGURE 5: Expanded combined uncertainties of flow rate and total fan pressure coefficients (95% level of confidence).

Figure 5 shows the extended combined uncertainties [29] of both flow rate coefficient

$$\Phi = \frac{4\dot{V}}{\pi D_{\text{fan}}^2 \cdot (1 - \nu_{\text{hub}}^2) \cdot u_{\text{tip}}} = \frac{\bar{c}_z}{u_{\text{tip}}} \quad (1)$$

and total fan pressure coefficient (in FD)

$$\begin{aligned} \Psi_t &= \frac{2}{\rho u_{\text{tip}}^2} \left[ \left( \sum_{i=1}^{81} \frac{P_{m,i}}{81} \right) - \frac{\rho}{2} (U_0 \cdot \cos \gamma)^2 \right] \\ &= \frac{2\bar{p}_m}{(\rho u_{\text{tip}}^2)} - \mu_z^2, \end{aligned} \quad (2)$$

with blade tip velocity  $u_{\text{tip}} = \pi f_0 D_{\text{fan}}$  and the measured stagnation pressures over ambient pressure  $p_{m,i}$  at the 81 Kiel probes (cf. Figure 4). The dynamic pressure caused by the ambient flow field is subtracted, introducing the ratio of wind tunnel velocity to blade tip velocity  $\mu = U_0/u_{\text{tip}}$  and its axial projection  $\mu_z = \mu \cdot \cos \gamma$ .

As defined in [29], the expanded interval of uncertainty  $U_c(\Phi)$  combines the individual measurement uncertainties of rotation rate  $f_0$ , density  $\rho$ , and static pressure difference over the multinozzles measured in accordance with ISO 5801, weighted by their linearized influence on  $\Phi$ . For the fan pressure coefficient,  $U_c(\Psi_t)$  combines the uncertainties of  $\rho$ ,  $f_0$ ,  $\gamma$ , and  $p_{m,i}$  and the wind tunnel stagnation pressure

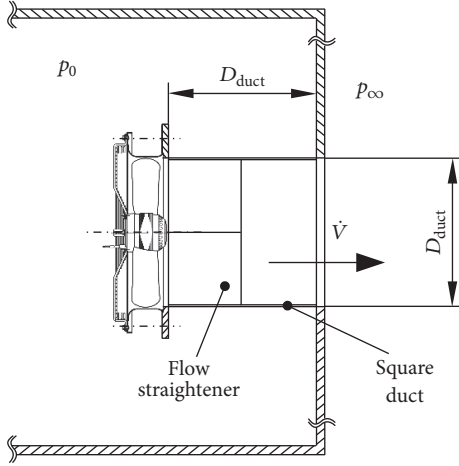


FIGURE 6: Standard fan test rig reference setup.

used to compute  $U_0$ . Uncertainties due to invariant fan geometries ( $D_{fan}$ ,  $\nu_{hub}$ ) are not considered. The resulting values  $U_c$  depend on the operating point and are shown in Figure 5 for a level of confidence of 95%. It can be seen how the nonstandard capturing of fan pressure  $\Psi_t$  is less precise than  $\Phi$ , but the measuring setup and equipment are still considered sufficiently accurate for the performed parametric studies.

Besides the estimation of uncertainty, results measured in the WFT are compared to data gathered in a standard fan test rig (SFT) which meets the requirements of ISO 5801. Static fan pressure  $\Psi_s$  from the free-inlet free-outlet SFT is compared to the static fan pressure estimate  $\Psi_s^*$  gained by subtracting the area averaged fan flow rate  $\dot{V}$  from measured stagnation pressure  $\bar{p}_m$  in WFT; that is,

$$\Psi_s = \frac{2(p_0 - p_{\infty})}{\rho u_{tip}^2}, \quad (3)$$

$$\Psi_s^* = \Psi_t - \Phi^2.$$

The static fan efficiency coefficients  $\bar{\eta}_s$  and  $\bar{\eta}_s^*$  are defined analogous to (3) with the product of fan pressure and flow rate scaled by measured electric power input  $P_e$ :

$$\bar{\eta} = \Phi \cdot \Psi \cdot \rho \pi D_{fan}^2 (1 - \nu_{hub}^2) \cdot \frac{u_{tip}^3}{(8P_e)} \quad (4)$$

with  $\Psi = \Psi_s$  and  $\Psi_s^*$ , respectively. The SFT test setup is comprised of a  $D_{duct}$  long duct section at the fan outlet, including the flow straightener, as shown in Figure 6. The systematic difference increases with remaining tangential and radial velocities  $c_\theta$  and  $c_r$  and with the axial velocity variance  $\sigma_{c_z}^2$  over the duct cross section:

$$\Psi_s^* - \Psi_s = \frac{\overline{c_r^2 + c_\theta^2 + c_z^2} - \bar{c}_z^2}{u_{tip}^2} = \frac{\overline{c_r^2} + \overline{c_\theta^2} + \sigma_{c_z}^2}{u_{tip}^2} \geq 0. \quad (5)$$

Figure 7 shows static fan curves from SFT and WFT for motor side inlet and guard grille configuration (SI-GG) and

for free rotor side inlet configuration without a guard grille (RI-noGG). It was found that WFT and SFT results agree very well, yet WFT tends to underestimate the static fan pressure and efficiency curves slightly at flow rates  $\Phi \geq 0.27$ . Given the greater overestimation of  $\Psi_s^* - \Psi_s$  in (5) at lower flow rates  $\Phi$ , it can be stated that lower values of fan pressure over flow rate in the order of  $\Delta\Psi_s \leq 0.02$  were measured systematically in WFT compared to SFT. Deviations can be attributed to the differing operating and measuring setup. The developed WFT setup described above is deemed adequate for the quantitative estimation of the influence of the different parameters on fan performance curves under the influence of uniform ambient flow fields, as outlined in the Introduction.

### 3. Integral Fan Performance

With the WFT setup described and assessed above, the performance of the two axial test fans was examined in different configurations. The influence of ambient flow fields at the fan inlet (FD) with different angles  $\gamma$  and ambient velocity ratios  $\mu$  is described first, followed by the case of a flow field at the fan outlet (ID). Finally, different shroud extensions are assessed in their potential to reduce adverse flow field influence in FD on Fan A.

Tests were performed with constant wind tunnel velocities  $U_0$ , and the industrial fans' rotation rates  $f_0$  showed moderate sensitivity to the operating point  $\Phi$ . The mean ratio of cross-flow to blade tip velocity  $\bar{\mu}$  is the arithmetic mean over all operating points per data set.

**3.1. Free Fan Inlet in an Ambient Flow Field.** Because of its practical relevance, multiple combinations of direction  $\gamma$ , fan blade geometries (Fan A versus Fan B) and inlet configuration (RI-noGG versus SI-GG) were examined in FD configuration. The effect of  $\bar{\mu} = 0.25$  at different incidence angles  $\gamma$  on the fan total pressure curves  $\Psi_t(\Phi)$  is shown as measured in the WFT in Figures 8–10.

For the rotor inlet configuration of Fan A without guard grille shown in Figure 8, fan pressure was significantly affected by any direction  $\gamma$  of the inlet ambient flow field. Even with the subtraction of stagnation pressure  $\mu_z^2$ , parallel onflow ( $\gamma = 0^\circ$ ) caused an increase in fan pressure, and so did angles  $\gamma \leq 56.3^\circ$ . Further increment of  $\gamma$  led to greater decrease of  $\Psi_t(\Phi)$  in an almost linear manner, in magnitudes of 0.04 to 0.08. With the absolute reduction of total fan pressure being greater at high flow rates  $\Phi$ , the affected fan pressure curves are more inclined than the reference curve ( $\mu = 0$ ). The respective change in efficiency  $\bar{\eta}_t$  is shown in Figure 11. While also showing larger decreases at high flow rates at angles  $\gamma \geq 56.3^\circ$ , an increase in efficiency at acute angles  $\gamma \leq 45^\circ$  was measured only at higher flow rates  $\Phi > 0.2$ .

A comparison with results from the literature is difficult, since volumetric efficiency of the system is usually reported, which implies heat exchanger resistance characteristics. The drop of total efficiency  $\bar{\eta}_t$  of about 43% at  $\Phi = 0.15$ ,  $\gamma = 90^\circ$ , and  $\mu = 0.258$  from Figure 11 can best be roughly compared to the approx. 20% volumetric effectiveness decline found in [22] mentioned above, which was at  $\mu \approx 0.27$  and a

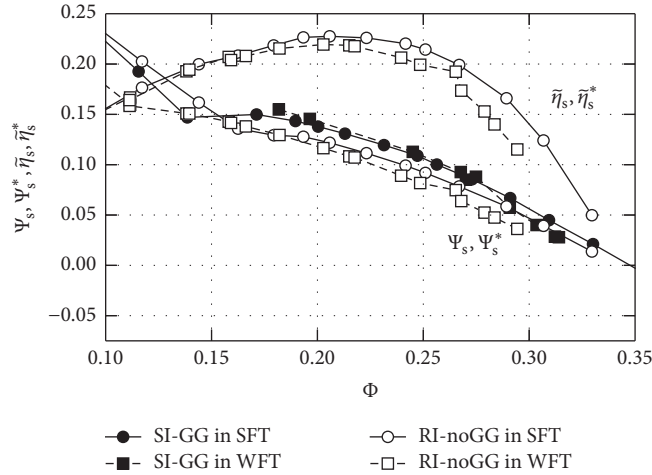


FIGURE 7: Comparison of static fan pressure and efficiency measured in standard fan test rig and wind tunnel fan test rig of Fan A in FD.

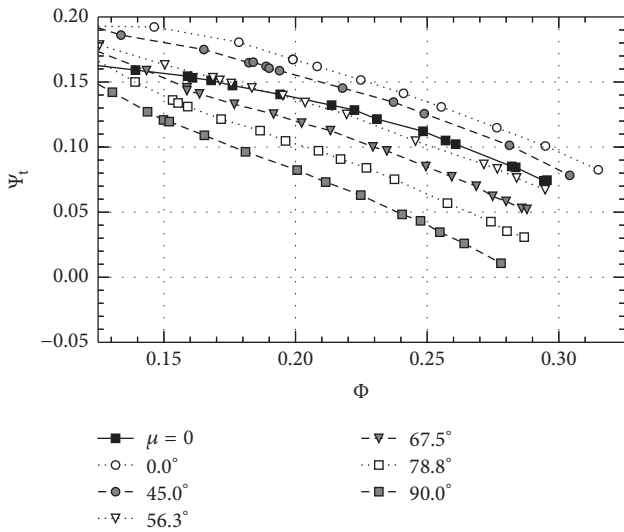


FIGURE 8: Fan A FD-RI-noGG total fan pressure at  $\bar{\mu} = 0.25$  and different  $\gamma$ .

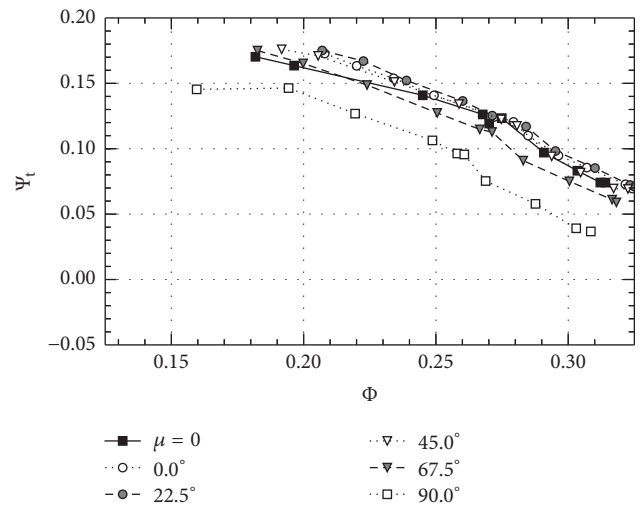


FIGURE 9: Fan A FD-SI-GG total fan pressure at  $\bar{\mu} = 0.25$  and different  $\gamma$ .

lower operating point  $\Phi \approx 0.1$ . Even though comparable figures may be concluded for more similar  $\Phi$ , differences and variation in experimental and computational setup (fan design, ACC application and system characteristics, platform influence, operating point, etc.) of the works found in the literature still prevail. This interdicts any further quantitative comparison beyond the statement that, in general, results of a similar magnitude were found in this study.

In the configuration with the motor side of the hub and the guard grille at the fan inlet FD-SI-GG, the reference performance without ambient flow of Fan A was better than that in FD-RI-noGG. From Figure 9 it can be found that an inlet flow field with  $\bar{\mu} = 0.25$  showed much smaller influence on total fan pressure  $\Psi_t$  for any  $\Phi$  and  $\gamma$ . Small gains in fan pressure were found for  $\gamma \leq 45^\circ$  and  $\Phi < 0.25$ . Greater angles  $\gamma$  between flow and fan axis caused a reduction of  $\Psi_t(\Phi)$  in the range of 0.02 to 0.05, also showing an increased inclination of

the fan curves, that is, a greater reduction of fan pressure at higher flow rates than at small ones.

The same favorable inlet configuration FD-SI-GG is examined for the straight bladed reference Fan B in Figure 11. All angles  $\gamma \leq 45^\circ$  caused a considerable increase of the fan pressure at  $\Phi < 0.25$  and a moderate increase beyond that operating point. Only cross-flow of  $\gamma = 90^\circ$  was found to induce a substantial decline in fan performance. Again, all fan curves showed the characteristically more inclined shape compared to the reference curve ( $\mu = 0$ ).

A decline in fan efficiency and pressure due to inlet cross-flow was to be expected, as summarized from results in the literature above. From there it is known that a flow detachment at the upwind edge of the fan shroud is common, which creates an asymmetric velocity distribution in longitudinal direction over the fan inlet. Even without this inlet vortex, the angle of attack at the fan blades varies laterally, with increases in relative velocities where fan blades

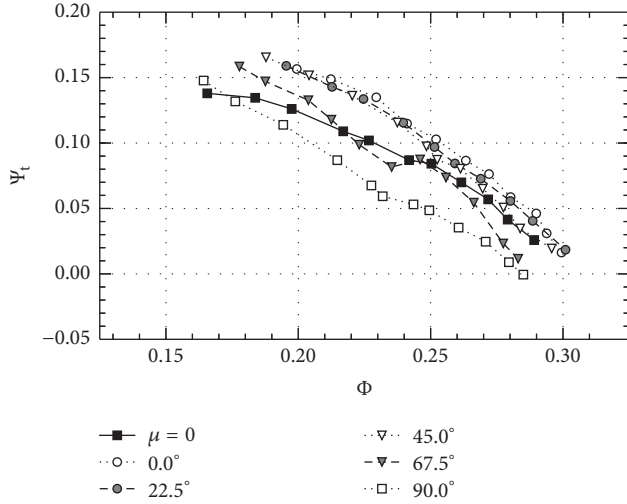


FIGURE 10: Fan B FD-SI-GG total fan pressure at  $\bar{\mu} = 0.25$  and different  $\gamma$ .

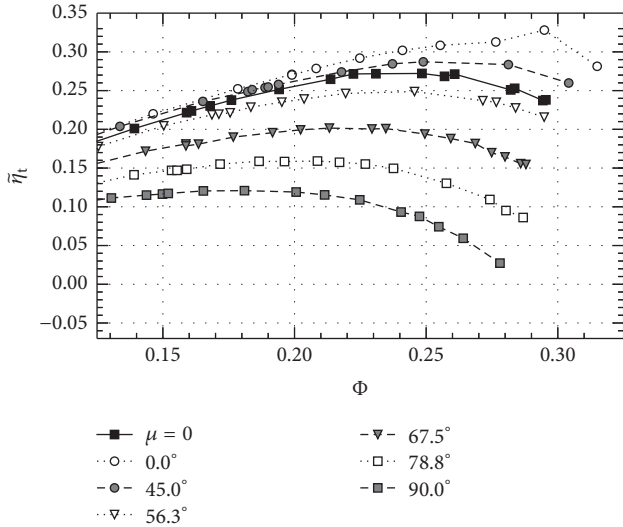


FIGURE 11: Fan A FD-RI-noGG total fan efficiency at  $\bar{\mu} = 0.25$  and different  $\gamma$ .

advance against  $U_0$  and vice versa where they retreat. These two effects can be expected to result in a strong azimuthal variation of the radial circulation around the blades (see, e.g., [23]). This causes the flow to increasingly detach from the blades and losses to become greater. The radial flow component over the blades due to longitudinal inertia of the inlet flow field is believed to introduce further asymmetries and detachments, especially considering effects at hub and shroud.

Comparing FD-RI-noGG and FD-SI-GG results, the guard grille has been shown to reduce the influence of the inlet flow field, which can be attributed to its guiding and straightening effect on the inlet flow before it enters the rotor plane. The annular concentric guard grille is an obstacle especially to radial inlet velocity components.

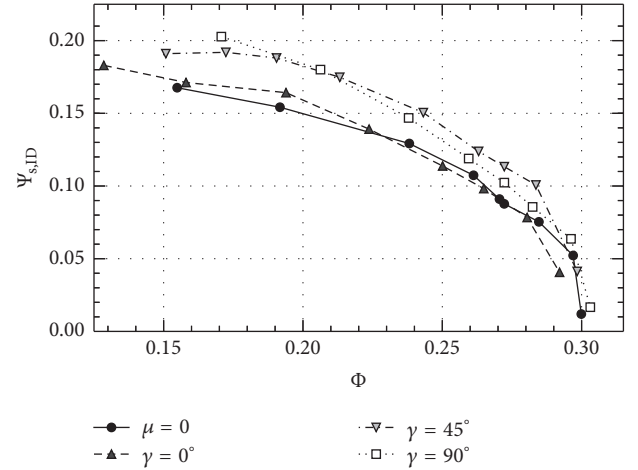


FIGURE 12: Fan A ID-SO-GG static fan pressure at  $\bar{\mu} = 0.25$  and different angles  $\gamma$ .

**3.2. Free Fan Outlet in an Ambient Flow Field.** Fan A was tested in ID configuration, that is, with its inlet mounted to the duct section and its outlet under the influence of an ambient flow field. As outlined above, the fan was fixed with a guard grille to the motor side of the hub at its outlet (SO-GG). Figure 12 shows the static fan pressure, computed as

$$\Psi_{s,ID} = \mu_z^2 - \frac{2\bar{p}_m}{\rho u_{tip}^2} = \left| \frac{2\bar{p}_m}{\rho u_{tip}^2} - \mu_z^2 \right|, \quad (6)$$

with the measured averaged pressure difference  $\bar{p}_m < 0$  between Kiel probes and static ambient pressure in the wind tunnel test section, assuming an outlet pressure increase by stagnation pressure  $\mu_z^2$ .

Parallel to the fan axis ( $\gamma = 0^\circ$ ), the static fan pressure curve was hardly affected by the ambient flow directed against fan operating direction. Interestingly, a gain in static pressure was found for  $\gamma = 45^\circ$  and  $90^\circ$  with decreasing flow rate  $\Phi$ . This may be caused by the effective (but not measured) lower pressure directly at the fan outlet caused by the detachment and deflection of the ambient flow around the fan outlet.

**3.3. Effect of Shroud Extensions on Adverse Inlet Cross-Flow Influence.** As shown in the literature above, inlet cross-flow is a common effect in ACC fans with a detrimental influence on fan performance. The experimental findings presented in the previous sections confirm this effect in more detail for varying incidence angles  $\gamma$ , different fan design, and installation configurations. Based on positive influence shown by Duvenhage et al. [10] and Meyer [12], various inlet shroud extension designs were examined in their potential to reduce the negative cross-flow influence on the more stable FD-SI-GG configuration of Fan A, which was shown in Figure 9.

A total of seven different shroud extensions were manufactured from thin metal sheet material. The basic cylindrical and conical shapes are defined in Figures 13(b) and 13(c), differing in length to fan diameter ratio  $\zeta$ . A short solid

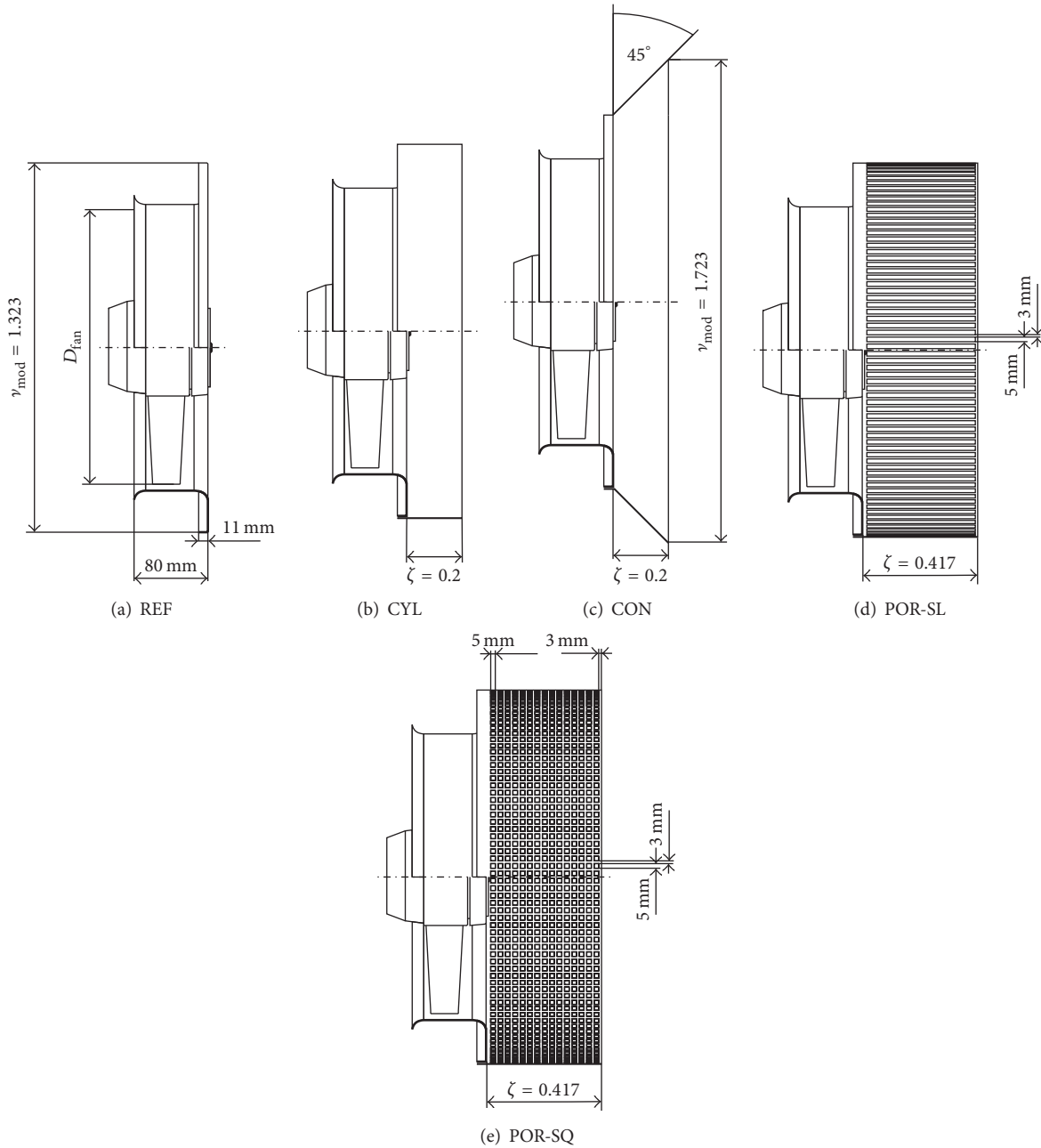


FIGURE 13: Basic geometries of inlet shroud extensions.

cylindrical inlet extension CYL-S and a longer one (CYL-M) were tested, with  $\zeta = 0.2$  and  $0.417$ .

Two cylindrical porous sheet designs with  $\zeta = 0.417$  were examined, denoted as POR-SL for a slot design shown in Figure 13(d), and POR-SQ for a square hole design illustrated in Figure 13(e). The respective solidity ratios of the sheets were  $0.375$  and  $0.609$ .

Three different solid conical inlet extensions were tested with  $\zeta = 0.2, 0.417,$  and  $0.733$ . The uniform aperture of  $90^\circ$  resulted in different outlet diameter ratios  $v_{mod}$  for the short, medium, and long conical devices CON-S, CON-M, and CON-L, listed in Table 2.

Reference results without ambient flow field ( $\mu = 0$ ) are shown in Figure 14 for the cylindrical shroud extension and in Figure 15 for the conical ones. While all fan curves lie in proximity to the reference fan curve, some configurations already induced a detectable negative influence on  $\Psi_t(\Phi > 0.26)$ . In particular CYL-M showed detrimental reference performance.

Under the influence of cross-flow ( $\gamma = 90^\circ$ ), any cylindrical device did clearly not improve fan performance, as it becomes obvious from Figure 16. Neither of the tested configurations CYL-S, CYL-M, POR-SL, and POR-SQ can be recommended as a good approach to reducing the adverse

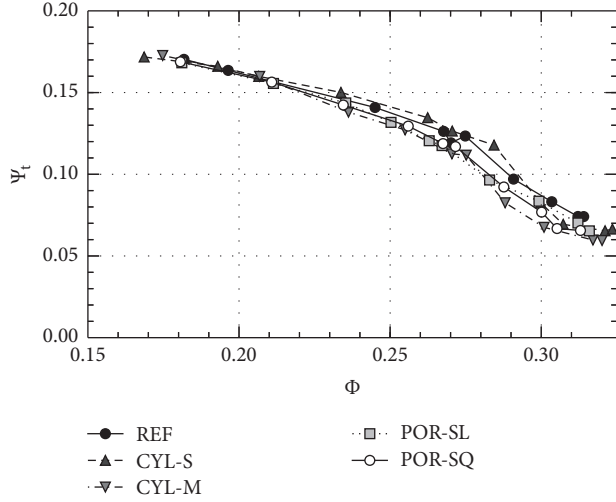
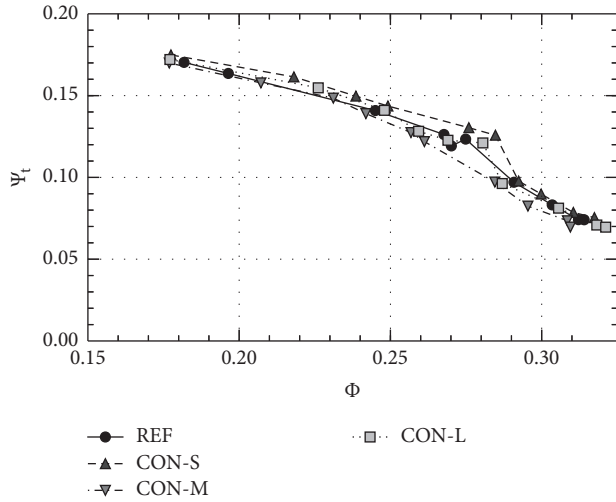
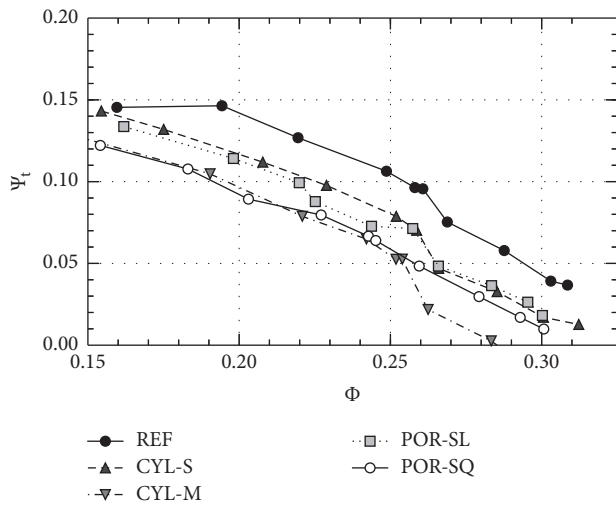
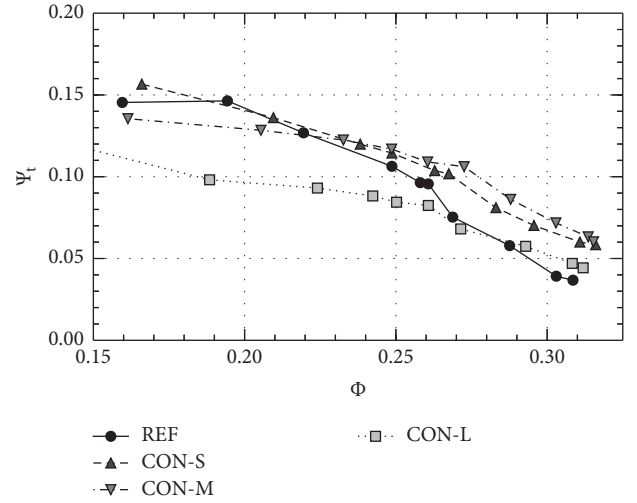
FIGURE 14: Influence of cylindrical shroud extensions ( $\mu = 0$ ).FIGURE 15: Influence of conical shroud extensions ( $\mu = 0$ ).FIGURE 16: Influence of different cylindrical shroud extensions under  $\bar{\mu} = 0.245$  and  $\gamma = 90^\circ$ .

TABLE 2: Geometric parameters of inlet shroud extensions.

Name	Solidity	$\zeta$	$\nu_{\text{mod}}$
REF	-	0.0	-
CYL-S	1.0	0.200	1.323
CYL-M	1.0	0.417	1.323
POR-SL	0.375	0.417	1.323
POR-SQ	0.609	0.417	1.323
CON-S	1.0	0.200	1.723
CON-M	1.0	0.417	2.157
CON-L	1.0	0.733	2.790

FIGURE 17: Influence of different conical shroud extensions under  $\bar{\mu} = 0.245$  and  $\gamma = 90^\circ$ .

influence of inlet cross-flow compared to the given reference configuration.

Conical devices on the other hand did show a potentially beneficial influence on the fan performance under cross-flow influence, as shown in Figure 17. At very high flow rates  $\Phi > 0.28$ , all three extension sizes CON-S, CON-M, and CON-L increased total fan pressure, but below that the long conical device was not effective. Both the short and medium conical shroud extensions yielded higher fan pressures than the reference curve at  $\Phi > 0.22$ , with CON-S performing better at lower flow rates and CON-M at higher flow rates. Generally, a flattening of the total fan pressure curve  $\Psi_t(\Phi)$  was achieved by the implementation of conical shroud extensions. It is believed that the flow detachment at the upwind edge of the shroud, which was documented, for example, in [12–16] simulations of inlet cross-flow, has less of a blocking effect at the fan inlet, because the vortex is more distant from the fan inlet axially and longitudinally (i.e., in wind direction). A more uniform flow field at the rotor inlet is the expected result of this, with consequently better fan performance.

## 4. Conclusions

The influence of different uniform ambient flow fields at the inlet or outlet of industrial axial fans on their integral performance curves was investigated in a nonstandard fan test rig inside a wind tunnel test section. The fan test rig and total fan pressure measurements using an array of Kiel probes were assessed and in good comparison to results from a standard fan test rig.

In the practically most relevant case of a flow field at the fan inlet (FD), ambient flow fields caused an inclination of the fan curves at any angle relative to the fan axis. In a rotor inlet configuration without guard grille, great sensitivity to ambient flow was observed, with potential fan pressure gains at small angles between flow and fan axis but substantial reductions towards greater angles up to cross-flow. With the motor side of the hub and the guard grille at the inlet, fan curves varied much less due to uniform inlet flow fields. Compared to the forward skewed blade test fan, the straight bladed fan showed to behave much less sensitively to ambient flow, with relevantly lowered total fan pressure measured only in perpendicular cross-flow configuration.

A uniform ambient flow field at the fan outlet (ID) parallel to the fan axis hardly affected static fan pressure. Off-axis configurations up to cross-flow were found to even increase static fan pressure, especially at lower flow rates.

Possible performance gains with inlet shroud extensions were investigated in an inlet cross-flow configuration. Solid and porous sheet cylindrical devices showed detrimental influence, while short solid conical shroud extensions improved fan performance compared to the reference configuration, especially at high flow rates.

## 5. Discussion and Outlook

The presented test setup made a large quantity of parameter permutations possible, such that multiple aspects of ambient flow influence on fan performance could be investigated. The examination of cross wind influence could be extended from single operating point research to wide fan operating ranges. This resulted in the presented effect of increasingly adverse affection of total fan pressure with the fan flow rate due to cross-flow. But the rapid measurement procedure with the Kiel probe array has the disadvantage that the flow straightener's effect is always included in the measured characteristic curves, which is presumably not linear with the flow rate or with azimuthal effects. With the restriction to  $\gamma = 90^\circ$ , future experimental setups could be designed more suitable and deliver results independent of such an outlet stator.

For technical application, single design aspects could be isolated and examined more in detail in their behavior under inlet or outlet cross-flow. More elaborate modifications of the blade shape, inlet shroud, or guard grille are worth investigating, advisably with a more precisely designed prototype fan instead of industrial fans, with controlled rotation rate and torque. To better understand the flow phenomena caused by cross-flow, optical measurements or numerical simulation of the fan flow field could be undertaken, which may, for

example, clarify how design modifications alter the inlet shroud detachment vortex with reference to the influence on the characteristic flow field.

## Conflicts of Interest

The authors declare that they have no conflicts of interest.

## Acknowledgments

The research leading to these results has received funding from the European Union's Seventh Framework Programme (FP7/2007–2013) under Grant Agreement no. 256797, within the "MACCSol" project.

## References

- [1] J. S. Maulbetsch and M. N. DiFilippo, "Cost and value of water use at combined cycle power plants," California Energy Commission, 2006.
- [2] J. S. Maulbetsch, "Cost/Performance Comparisons of Water Conserving Power Plant Cooling Systems," in *Proceedings of the ASME 2011 International Mechanical Engineering Congress and Exposition*, pp. 385–390, Denver, Colorado, USA.
- [3] G. Kröger, *Air-Cooled Heat Exchangers and Cooling Towers*, PennWell Books, 2004.
- [4] K. Duvenhage and D. G. Kröger, "The influence of wind on the performance of forced draught air-cooled heat exchangers," *Journal of Wind Engineering & Industrial Aerodynamics*, vol. 62, no. 2-3, pp. 259–277, 1996.
- [5] C. Meyer and A. Zapke, "A modelling strategy for large scale mechanical draught air-cooled systems," in *Proceedings of the 10th Int Conf on CFD in oil & gas, metallurgical and process industries (SINTEF)*, Trondheim, Norway, 2014.
- [6] M. T. F. Owen and D. G. Kröger, "An investigation of air-cooled steam condenser performance under windy conditions using computational fluid dynamics," *Journal of Engineering for Gas Turbines and Power*, vol. 133, no. 6, Article ID 064502, 2011.
- [7] M. T. F. Owen and D. G. Kröger, "The effect of screens on air-cooled steam condenser performance under windy conditions," *Applied Thermal Engineering*, vol. 30, no. 16, pp. 2610–2615, 2010.
- [8] C. A. Salta and D. G. Kröger, "Effect of inlet flow distortions on fan performance in forced draught air-cooled heat exchangers," *Heat Recovery Systems and CHP*, vol. 15, no. 6, pp. 555–561, 1995.
- [9] S. J. Van Der Spuy, F. N. Le Roux, T. W. Von Backström, and D. G. Kröger, "The simulation of an axial flow fan performance curve at low flow rates," in *Proceedings of the ASME 2011 Turbo Expo: Turbine Technical Conference and Exposition, GT2011*, pp. 425–434, Canada, June 2011.
- [10] K. Duvenhage, J. A. Vermeulen, C. J. Meyer, and D. G. Kröger, "Flow distortions at the fan inlet of forced-draught air-cooled heat exchangers," *Applied Thermal Engineering*, vol. 16, no. 8-9, pp. 741–752, 1996.
- [11] J. R. Bredell, D. G. Kröger, and G. D. Thiart, "Numerical investigation of fan performance in a forced draft air-cooled steam condenser," *Applied Thermal Engineering*, vol. 26, no. 8-9, pp. 846–852, 2006.
- [12] C. J. Meyer, "Numerical investigation of the effect of inlet flow distortions on forced draught air-cooled heat exchanger performance," *Applied Thermal Engineering*, vol. 25, no. 11-12, pp. 1634–1649, 2005.

- [13] S. J. van der Spuy, T. W. von Backström, and D. G. Kröger, "An evaluation of simplified methods for modelling the performance of axial flow fan arrays," *Research and Development Journal of the South African Institute of Mechanical Engineering*, pp. 12–20, 2010.
- [14] S. J. van der Spuy and T. W. von Backström, "An evaluation of simplified CFD models applied to perimeter fans in air-cooled steam condensers," *Proc Inst of Mech Eng Part A: J Power Energy*, no. Part A, pp. 948–967, 2015.
- [15] X. Zhang and H. Chen, "Performance Forecast of Air-Cooled Steam Condenser under Windy Conditions," *Journal of Energy Engineering*, vol. 142, no. 1, Article ID 04015010, 2016.
- [16] X. Zhang and T. Wu, "Effects of diffuser orifice plate on the performance of air-cooled steam condenser," *Applied Thermal Engineering*, vol. 98, pp. 179–188, 2016.
- [17] Z. Gu, X. Chen, W. Lubitz, Y. Li, and W. Luo, "Wind tunnel simulation of exhaust recirculation in an air-cooling system at a large power plant," *International Journal of Thermal Sciences*, vol. 46, no. 3, pp. 308–317, 2007.
- [18] C. Butler and R. Grimes, "The effect of wind on the optimal design and performance of a modular air-cooled condenser for a concentrated solar power plant," *Energy*, vol. 68, pp. 886–895, 2014.
- [19] L. Xiao, Z. Ge, X. Du, L. Yang, and Z. Xu, "Operation of air-cooling CHP generating unit under the effect of natural wind," *Applied Thermal Engineering*, vol. 107, pp. 827–836, 2016.
- [20] J. S. Maulbetsch, M. N. DiFilippo, and J. O'Hagan, "Effect of wind on air-cooled condenser performance," in *Proceedings of the ASME 2011 Int Mech Eng Congr & Expo*, vol. 1, pp. 391–396.
- [21] J. S. Maulbetsch and M. N. DiFilippo, "Effect of wind on the performance of air-cooled condensers," Final Project Report CEC, California Energy Commission, 2010.
- [22] N. Fourie, S. J. van der Spuy, and T. W. von Backström, "Simulating the effect of wind on the performance of axial flow fans in air-cooled steam condenser systems," *Journal of Thermal Science and Engineering Applications*, vol. 7, no. 2, Article ID 021011, 2015.
- [23] G. D. Thiart and T. W. von Backström, "Numerical simulation of the flow field near an axial ow fan operating under distorted inflow conditions," *Journal of Wind Engineering & Industrial Aerodynamics*, vol. 45, no. 2, pp. 189–214, 1993.
- [24] G. D. Thiart, *A Numerical Procedure for Predicting the Effects of Distorted Inflow Conditions on the Performance of Axial Flow Fans [Ph.D. thesis]*, University of Stellenbosch, 1990.
- [25] C. J. Meyer and D. G. Kröger, "Numerical simulation of the flow field in the vicinity of an axial flow fan," *International Journal for Numerical Methods in Fluids*, vol. 36, no. 8, pp. 947–969, 2001.
- [26] W. H. Stinnes and T. W. von Backström, "Effect of cross-flow on the performance of air-cooled heat exchanger fans," *Applied Thermal Engineering*, vol. 22, no. 12, pp. 1403–1415, 2002.
- [27] ISO 5801:2007, "Industrial fans – Performance testing using standardized airways," 2007.
- [28] T. Heinemann, C. Bakeberg, H. Lienhart, and S. Becker, "Total pressure measurements behind an axial ventilator using a Kiel probe array," *Notes on Numerical Fluid Mechanics and Multidisciplinary Design*, vol. 124, pp. 573–581, 2014.
- [29] BIPM Joint Committee for Guides in Metrology, "Evaluation of measurement data – guide to the expression of uncertainty in measurement JCGM 100:2008," in *GUM 1995 with minor corrections*, 2008.

## Research Article

# Design, Modeling, and CFD Analysis of a Micro Hydro Pelton Turbine Runner: For the Case of Selected Site in Ethiopia

Tilahun Nigussie,<sup>1</sup> Abraham Engeda,<sup>2</sup> and Edessa Dribssa<sup>1</sup>

<sup>1</sup>*School of Mechanical and Industrial Engineering, Addis Ababa Institute of Technology, Addis Ababa, Ethiopia*

<sup>2</sup>*Department of Mechanical Engineering, Michigan State University, East Lansing, USA*

Correspondence should be addressed to Tilahun Nigussie; [tilahun.nigussie@aait.edu.et](mailto:tilahun.nigussie@aait.edu.et)

Received 4 June 2017; Revised 17 August 2017; Accepted 29 August 2017; Published 12 October 2017

Academic Editor: Rafat Al-Waked

Copyright © 2017 Tilahun Nigussie et al. This is an open access article distributed under the Creative Commons Attribution License, which permits unrestricted use, distribution, and reproduction in any medium, provided the original work is properly cited.

This paper addresses the design, modeling, and performance analysis of a Pelton turbine using CFD for one of the selected micro hydro potential sites in Ethiopia to meet the requirements of the energy demands. The site has a net head of 47.5 m and flow rate of 0.14 m<sup>3</sup>/s. The design process starts with the design of initial dimensions for the runner based on different literatures and directed towards the modeling of bucket using CATIA V5. The performance of the runner has been analyzed in ANSYS CFX (CFD) under given loading conditions of the turbine. Consequently, the present study has also the ambition to reduce the size of the runner to have a cost effective runner design. The case study described in this paper provides an example of how the size of turbine can affect the efficiency of the turbine. These were discussed in detail which helps in understanding of the underlying fluid dynamic design problem as an aid for improving the efficiency and lowering the manufacturing cost for future study. The result showed that the model is highly dependent on the size and this was verified and discussed properly using flow visualization of the computed flow field and published result.

## 1. Introduction

Despite the fact that many rural communities have good access to plenty of water resources, the most serious problem faced by a country like Ethiopia is that of rural electrification. One of the most important and achievable methods to produce electricity is to introduce a standalone electric power generation, using renewable resources. Rural Electrification Fund (REF), which is operating under the Ministry of Water, Irrigation and Energy (MWIE), is working to control the energy crisis in the country [1–3]. In its effort, it has identified some potential micro hydro sites in the country. This potential for small-scale hydro power is estimated to be 10% of the total potential (1,500–3,000 MW) [3, 4]. So far, out of the total potentials for micro hydro power (MHPs) in the country (over 1000 MW) only a minute portion of it (less than 1%) is developed [4]. If these water resources were properly harnessed, it will help Ethiopia to meet its power demand and maintain her economic growth for the next decade. Due to the existence of these numerous sites in Ethiopia, suitable for

micro hydro turbine installations, the need for development of micro hydro turbines using locally available materials and with local manufacturing capability has been identified for those sites which have been evaluated and proved to be viable, the aim being to cut the equipment cost which is imported from various countries from Europe and Asia. As a result, future of micro hydro developments in the country would need a manufacturer to provide turbines and parts with new design.

Figure 1 shows some MHP areas. These areas are mainly in the Western and South-Western part of the country and they are characterized by high mean annual rainfall ranging from 300 mm to over 900 mm. For many of these sites, a Pelton turbine is the only option. This is due to higher mountains providing higher heads and seasonal variation in flow rates appropriate for the choice of Pelton turbines for hydro power projects in the country [4–6].

Depending on water flow and design, Pelton wheels operate best with heads from 15 meters to 1,800 meters, although there is no theoretical limit. In this turbine, water

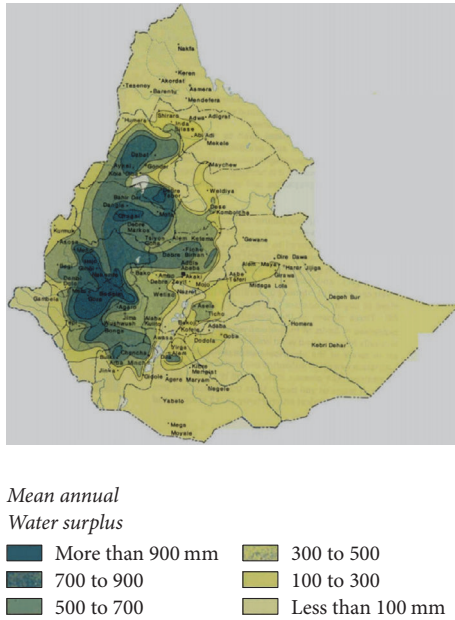


FIGURE 1: Distribution of MHP potential sites in Ethiopia [4].

is brought down through the penstock pipe to a nozzle, and it comes out into the turbine casing. The jet is then directed at a wheel, or runner, which has a number of buckets around its edge. The force of the jet on this wheel makes it turn and gives the output power [7–9]. However, investigation reveals that there is no company or institution engaged in supplying this micro Pelton turbine locally in the country. As a result, the necessity and the possibilities to design and manufacture Pelton turbines locally are increasing. More often the material and the skilled labour as well as technical staff are available but what is missing is the information and knows-how [4, 6].

More precisely, in the new context where harvesting small hydro potentials can become economically viable, there is also a need to provide solutions to reduce the design cycle time and cost for Pelton runners. It is known that, with increasing demand, the performance analysis of turbine such as efficiency and dynamic behavior is also an important aspect to analyze its suitability under different operating conditions [7]. Additionally, it is used by the turbine producer to guarantee the hydraulic performance of a turbine to the customer. However, it is known that design of Pelton turbine is mainly conducted from know-how and extensive experimental testing, which provide an empirical understanding of factors that are important to turbine design. But, in today's highly competitive market of turbine, the performance is often difficult to determine in the short term with this traditional practice. Therefore, the incorporation of computational fluid dynamics (CFD) in the design of micro hydro turbines appears to be necessary in order to improve their efficiency and cost-effectiveness beyond the traditional design practices [7, 10–12].

The main topic of investigations by the CFD method has focused on the interactions between the jet and the rotating buckets as well as the relative flows within the buckets. These are flows that are so far not easily accessible by experimental

measurements [11]. CFD simulations are therefore likely considered as an available way for investigating complex flows in Pelton turbines, provided that they are reliable and able to reveal the possibility of improving the system efficiency and reducing the manufacturing cost. In addition, CFD provide deeper understanding of the flow mechanisms that govern performance. The most detailed CFD analysis of rotating Pelton turbine was done by Perrig et al. [13, 14] by considering five buckets and the computed results were compared with experimental results at best efficiency point (BEP).

As explained by Zhang [7] in Pelton turbine book, hydraulic design of a Pelton turbine, the related practical experiences have thus always played a major role besides applying general design rules. Even the optimum bucket number and the size of a Pelton wheel, for instance, were determined only by experience or model tests without relying on any hydro mechanical background. The main reasons for this were the complex flow conditions in both the high-speed jet and the unsteady interaction between the high-speed jet and the rotating Pelton buckets [7, 11]. But nowadays, the largest amount of publications on modeling of Pelton turbines uses commercial code ANSYS CFX [7, 10, 14]. The capability of solving complex impulse turbine related problems that include multiphase flow with free surfaces has been demonstrated by a number of studies and is becoming increasingly significant [10–18]. However, large computational cost of the simulations is also the main factor why there is a lack of publications on CFD usage for Pelton turbines [11]. As a result, various authors made different simplifying assumptions in order to reduce this cost as much as possible and make Pelton simulation for performance predictions possible. Most CFD simulations reviewed in the literatures were assuming symmetry in the flow as simplifying assumption and therefore they model only half of a runner or a bucket. Because of the periodic behavior assumption, the majority of simulations used also only a fraction of a runner with the number of buckets in the section modeled being 2, 3, 5, 7, or even 10 [11]. Many authors used only 3 consecutive buckets where the torque was measured only on the bucket in the middle. This torque measured on a single middle bucket was then used to construct the torque on the runner assuming that every bucket would undergo identical loading [10, 11]. The first bucket was required to produce the back-splashing water that impacts the middle bucket. The third bucket was required to realistically cut the jet when it is impacting the second bucket. Even though, it was shown that it is possible to model the complete runner; this could be seen as unnecessary usage of computational resources. For instance, using the same computational resources and a reduced complexity simulation with only 3 buckets would allow simulations with better discretized grids (therefore improving accuracy) or analyzing more operating points or design variations and enable the optimization of Pelton turbine (see [11, 13, 14]).

So far, few investigators have only reported diverse values of maximum efficiencies as shown in Table 1. Because of commerciality of the turbine, many of the investigators normalized their results in their publications. Most papers report that the shape of the efficiency curve is well captured, while actual differences between measured and numerically

TABLE 1: Some Pelton turbine studies and maximum efficiency levels attained.

Investigators	Net head (m)	Flow rate (m <sup>3</sup> /sec)	Runner speed (rpm)	PCD (mm)	Maximum efficiency, %
Panthee et al. [10]	53.9	0.05	600	400	82.5
Panagiotopoulos et al. [19]	100	135% of BEP	1000	400	86.7
Solemslie and Dahlhaug [20]	70	—	—	513	77.75
Pudasaini et al. [21]	80.85	0.09218	600	490	87.71

TABLE 2: Proposed site data for MHP development [22].

Region	Zone	Wereda	Kebel	River name	Head (m)	Flow rate (L/s)
Oromia	W/showa	Tokikutay	Melkey Hera	Indris	>50	140

predicted efficiency remain unreported. An exception is [10, 19–21], where predicted efficiency was quite close to the measurements. Fewer still go deeper into the design and performance analysis of the turbine.

Due to the natural limitations concerning publication of results concerning turbines from commercial companies, one of the goals of this research paper has been to design and simulate using a Pelton turbine and compare the obtained result with the reference from Table 1. The results in Table 1 may have also depended on the laboratory settings and other controls of design parameters; the results still indicate room for further performance improvement. Even though this is a well-established turbine technology, there are many unanswered questions regarding design and optimization. Thus, further development is still relevant today. As a main feature, previous studies have mainly focused on experimental studies of turbine efficiency as a function of different geometrical parameters of the buckets. No paper that consists of design analysis, modeling, numerical performance analysis of rotating Pelton turbine runner, and its comparison with experimental data to reduce the size of the turbine has been published as far as we know. Therefore, a design study that takes into account the links between the size of the runner and the flow field characteristics is needed. This paper addresses this issue for one of the selected potential sites (Indris River) in Ethiopia to meet the requirements of the energy demands. The design process consists of sequential stages: parametric design of turbine, and CFD simulation with the baseline design and a smaller size of the turbine from the baseline design. The result of this study will be an input to the optimization of the runner for future study. In this way, a study was carried on Pelton turbine runner specifically designed and the result of this research was compared with that of Table 1 (published results). In the second part of this article, optimization of the geometry of this turbine, local manufacturing of the optimal geometry and testing of this turbine in the lab, and finally comparison of the results obtained will be presented. The result of this research will also ensure availability of documented procedure by contributing knowledge for designing micro hydro Pelton turbine in the

country. Most importantly, a general awareness and technical understanding of successful micro hydro turbine technology will be developed and fostered at the local and regional levels so that rural electrification projects can be implemented effectively.

## 2. Method and Methodology

*2.1. Problem Description.* After surveying different villages in the South-West District of Ethiopia, we narrowed our choices down to one: Melkey Herra Village. It is a rural community, Keble, roughly 149 kilometers from Addis Ababa, and is well renowned for tourism. Its geographical coordinates are 08° 51' 40" North and 37° 45' 10" East which does not have the access to electricity. The selected water resource for hydroelectric generation is "Indris River" for the communities living in the village called "Melkey Herra" [22]. The micro hydroelectric project is a main priority to the community. Due to the recent crises of electricity in the community, it is utmost need for the utilization of micro hydropower. The data (Table 2) has been found from primary and secondary data collection.

*2.2. Steps Involved in Design of the Turbine.* To start the initial design, calculations will be conducted to size turbine parts. The theory behind these is mainly taken from the "Micro Hydro Pelton Turbine Manual, by Thake [6]". Different assumptions are made in the design process using design guides and literature.

*2.2.1. Calculation of the Net Head ( $H_n$ ).* The net head at the nozzle exits can be expressed by the following formula [6]:

$$H_n = H_g - H_l, \quad (1)$$

where  $H_g$  is the gross head and  $H_l$  is total head losses due to the open channel, trash rack, intake, penstock, and gate or valve. These losses approximately equal 5% of gross head [6]. This makes the net head available at the end of penstock as 50 m – 2.5 m = 47.5 m.

*2.2.2. Selection of Turbine.* For the proposed site data head, 50 m, and flow rate, 140 liter/sec combination (from Table 2),

TABLE 3: Calculation summary to determine the turbine speed ( $N$ ) and PCD.

Name	Symbol	Unit	Value			
Number of jets	$n_{jet}$	—	1	2	3	4
Jet diameter	$d_{jet}$	mm	77.0	54.4	44.4	38.5
Runner PCD	PCD	m	699.667	494.740	403.953	349.834
Available PCD	PCD	mm	700	500	425	350
Turbine speed	$N$	rpm	371	520	611	742
Gear ratio	$X$	—	4.04	2.89	2.45	2.02

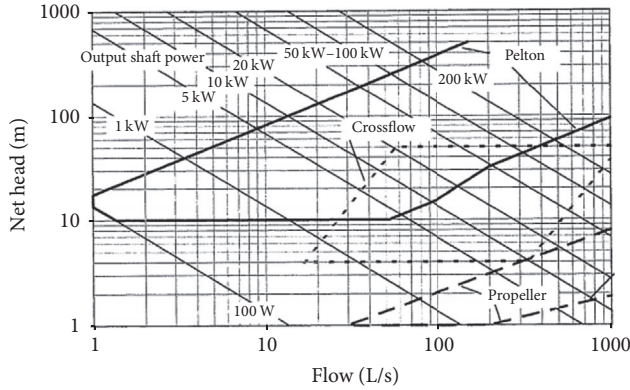


FIGURE 2: Application ranges for different types of turbine [6].

principally a choice was necessary between Pelton and cross flow situations as shown in Figure 2. The figure shows the approximate application ranges of turbines for micro hydro. Therefore, this chart can be used for selection of the turbine type. The area highlighted in solid line shows an indicative range of operation for the Pelton runner used in this research paper.

2.2.3. *Calculation of Jet Diameter ( $d_{jet}$ ).* The pressure at the bottom of the penstock creates a jet of water with velocity,  $V_{jet}$

$$V_{jet} = K_N \sqrt{2gH_n} \quad (2)$$

where  $V_{jet}$  is jet velocity (m/s),  $K_N$  is nozzle velocity coefficient (normally around **0.95** to **0.99**), and  $H_n$  is net head at the nozzle. The flow rate ( $Q$ ) is then given by this velocity multiplied by the cross-sectional area of the jets:

$$\begin{aligned} Q &= A_{jet} \times V_{jet} \times n_{jet} \\ &= \Pi \frac{d_{jet}^2}{4} \cdot V_{jet} \cdot n_{jet}, \end{aligned} \quad (3)$$

where  $n_{jet}$  is number of jets and  $d_{jet}$  is diameter of jets (m)

Combining (2) and (3) and using an average value of 0.97 for  $K_N$ , then solving for  $d_{jet}$  becomes

$$d_{jet} = \frac{0.54}{H_n^{1/4}} \cdot \sqrt{\frac{Q}{n_{jet}}}. \quad (4)$$

The next step in the turbine design process is to determine the pitch circle diameter (PCD) of the turbine.

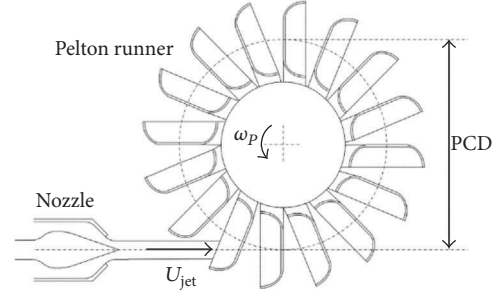


FIGURE 3: Diagram of a Pelton runner showing PCD [6].

2.2.4. *Calculation of the Runner Circle Diameter (PCD).* Figure 3 shows a schematic of a Pelton runner with a pitch circle diameter  $D (=2R)$  rotating at angular velocity  $\omega_p$ .

Beginning with the derived formula to determine the turbine speed which can be expressed as

$$2\pi \frac{N}{60} \cdot \frac{D}{2} = x \cdot V_{jet}, \quad (5)$$

where ( $D$ ) or PCD is pitch circle diameter (m) and  $x$  is ratio of runner velocity to jet velocity ( $x = 0.46$  is used to produce the maximum power out of the turbine) [6].  $N$  is rotational velocity of runner (rpm). Substituting for  $V_{jet}$ , from (2), and using  $x = 0.46$ , (2) becomes

$$D = 37.7 \times \frac{\sqrt{H_n}}{N}. \quad (6)$$

A spreadsheet is prepared as shown in Table 3 to determine the turbine speed ( $N$ ) and PCD.

From Table 3 all the gear ratios are possible with belt drives. From the result in Table 3, runner pitch diameters ( $D$ ) of 350 mm and 425 mm with 4-jet and 3-jet turbine, respectively, have smaller pitch diameter. However, for a turbine of these powers making is very complex and needs considerable expertise, so these are probably not an option [6]. The single jet solution is possible, but a 700 mm PCD runner makes a very big turbine. The best solution is the 500 mm, 2-jet turbine. Therefore, we can take the PCD to be 500 mm in our design analysis. To estimate the final system power output, efficiency values for the nozzles, turbine, and generator can be assumed. Thake [6] provides reasonable values for each. Table 4 shows the values of assumed efficiency in this research.

The equations used to determine the different design parameters of wheel are collected in Table 5.

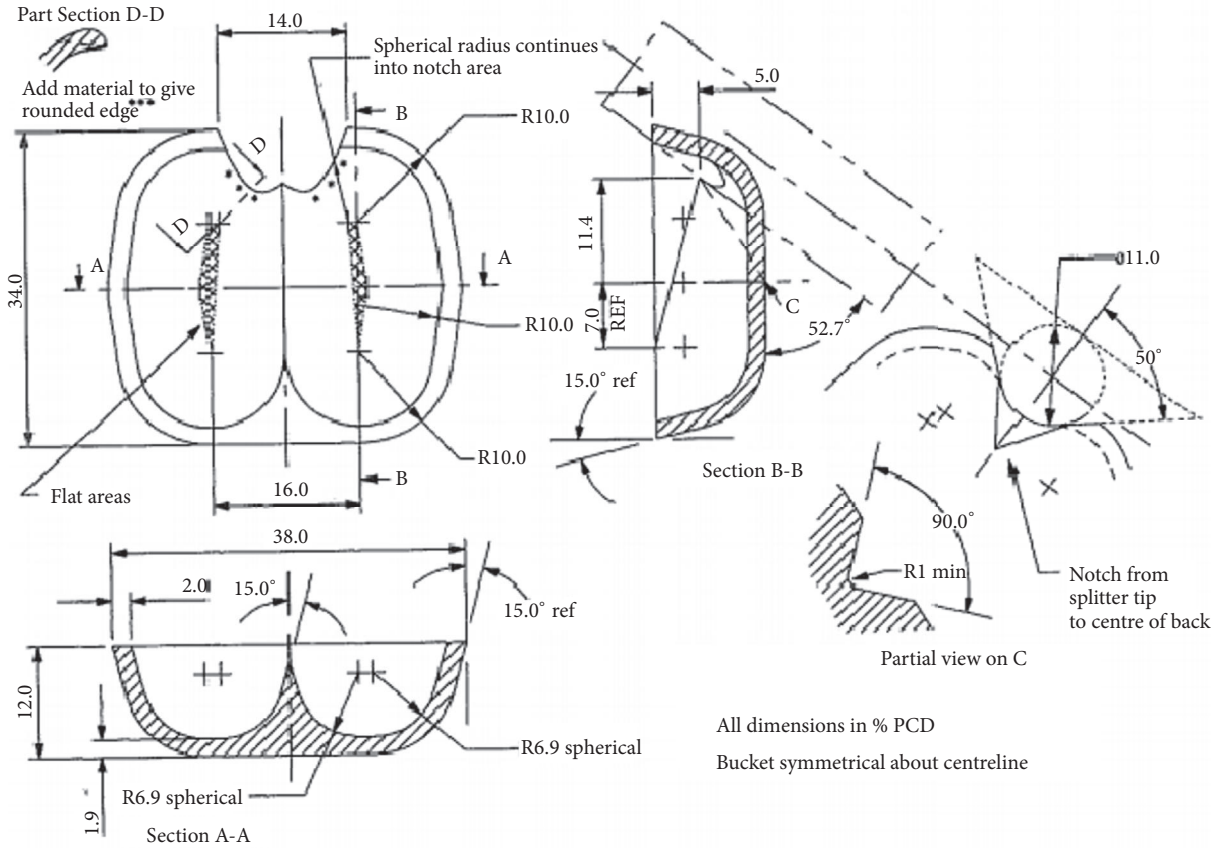


FIGURE 4: A scalable Pelton bucket. All dimensions are in % of PCD [6].

TABLE 4: Pelton turbine parts' assumed efficiency [6].

Part	Symbol	Assumed efficiency
Penstock	$\eta_p$	0.95
Manifold	$\eta_m$	0.98
Nozzle	$\eta_n$	0.94
Runner	$\eta_r$	0.8
Drive	$\eta_d$	1
Generator	$\eta_g$	0.8
Overall efficiency	$\eta_o$	0.56

2.2.5. *Detail Bucket Geometry Design.* Figure 4 shows the dimensions of the bucket as percentage values of the PCD of the turbine. Like the basic bucket model changing the PCD value within the model allows it to be scaled [6]. The physical dimensions of the bucket for the selected site data based on empirical relations for 500 mm PCD are shown in Table 6 which is used in this report for modeling of the bucket.

A basic stem for machining, used for bolting or clamping the buckets to the hub, is shown in Figure 5. Bolted buckets are an ideal solution for this research and are chosen as discussed in [6].

From all the above calculated parameters in Table 6 and some standard parameters using Figures 4 and 5, the

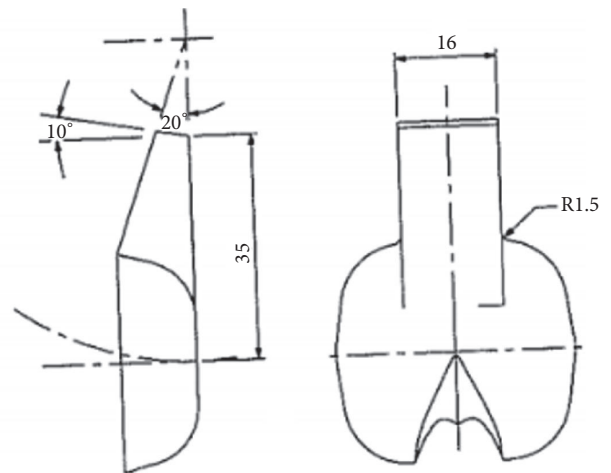


FIGURE 5: A basic bucket stem design for bolted fixing. All dimensions are in % PCD [6].

modeling of the bucket is done using CATIA V5 software as shown in Figure 6(a). The bucket design was specified by defining the outline of the bucket using the dimensions given in Figures 4 and 5.

The basic bucket model was adapted to form an entire bucket by the use of patterning. Two-disc plate was used to

TABLE 5: Basic design calculation summary of Pelton turbine.

Descriptions	Data	Unit	Design guidelines Thake 2000 [6]
$H_{\text{-net turbine}}$	46.5	mm	$H_{\text{-net turbine}} = H_{\text{-net}} \times \text{manifold efficiency}$
$K_N$	0.97	—	Ranges (between 0.95–0.99).
$V_{\text{-jet}}$	29.6	m/s	Velocity of the jet (for $n_{\text{jet}} = 2$ )
$d_{\text{-jet}}$	54.4	mm	Diameter of the jet (for $n_{\text{jet}} = 2$ ) $d_{\text{-jet}} = 0.11 \times \text{PCD}$
$x(U/V\text{-jet})$	0.46	—	For maximum power output (blade speed/ $V\text{-jet}$ ) ratio
Bucket speed	13.6	m/s	$U = x \cdot V_{\text{jet}} = 0.46 \times 29.6$
$N$	1500	Rpm	Standard generator RPM
$N\text{-}r$	1170	Rpm	Runaway speed = 1.8, turbine optimum speed
$\eta$	0.56		Total system efficiency
$P$	36.57	kW	Estimated electrical power = $\rho g H_{\text{-net}} \times Q \times \eta_0$
$P\text{-turbine}$	51.2	kW	Turbine mechanical power = $\rho g H_{\text{-net turbine}} \times Q \times \eta_r$

TABLE 6: Physical baseline bucket dimensions result for the selected site data.

Parameters, formula [6]	Calculation	Dimensions/result	Unit
Height of bucket, $h = 0.34D$	$h = 0.34 \times 500$	170	mm
Cavity length: $h1 = 5.6\%D$	$h1 = (0.056) \times 500$	28	mm
Length to impact point: $h2 = 0.114D$	$h2 = 0.114 \times 500$	57	mm
Width of bucket opening, $a = 0.14D$	$a = 0.14 \times 500$	56	mm
Bucket thickness: $t1 = 0.002D$	$t1 = 0.002 \times 500$	1	mm
Approximate number of buckets, $Z$	$Z = D/2d + 15$	18	
Depth of the bucket, $t = 0.121D$	$t = 0.121 \times 500$	60.5	mm
Width of the bucket, $b = 0.38D$	$b = 0.38 \times 500$	190	mm

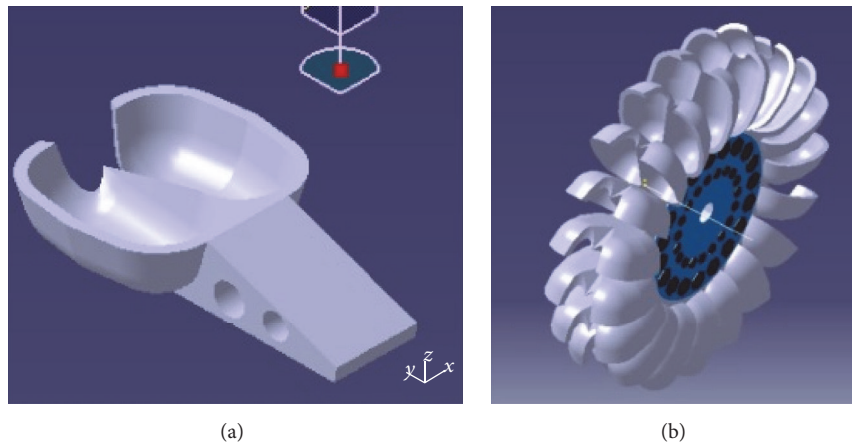


FIGURE 6: Solid model of Pelton turbine for the selected site data, (a) bucket and (b) 3D view of the runner right.

mount the buckets circularly as shown in Figure 6(b). The discs were to sandwich the buckets into place.

### 3. Computational Analysis

For the selected Melkey Herra's micro hydro power site, Pelton turbine was the most suitable hence chosen for our numerical performance analysis. The main dimensions of the turbine examined here correspond to this ideal plant. The numerical techniques created during this section included

many numerical and physical assumptions to simplify the problem. This was necessary because accurate modeling of impulse turbines (Pelton in this case) that include complex phenomena like free surface flow, multifluid interaction, rotating frame of reference, and unsteady time dependent flow is a challenge from a computational cost point of view [10–18].

*3.1. Physical Assumptions and Scaling Down.* The computational domain was created removing the features that were

TABLE 7: Turbine geometry and setup values for prototype and model.

Parameters	Symbol	Unit	Prototypes' values	Selected model operating condition
Flow rate	$Q$	Lts/s	140	20.84278
Head	$H$	m	47.5	13.34275
PCD	$D$	mm	500	265
Bucket width	$B$	mm	190	100.7 > 80 mm
Power	$P$	KW	51.2	2.14
Number of buckets	$Z$		<b>18</b>	<b>18</b>

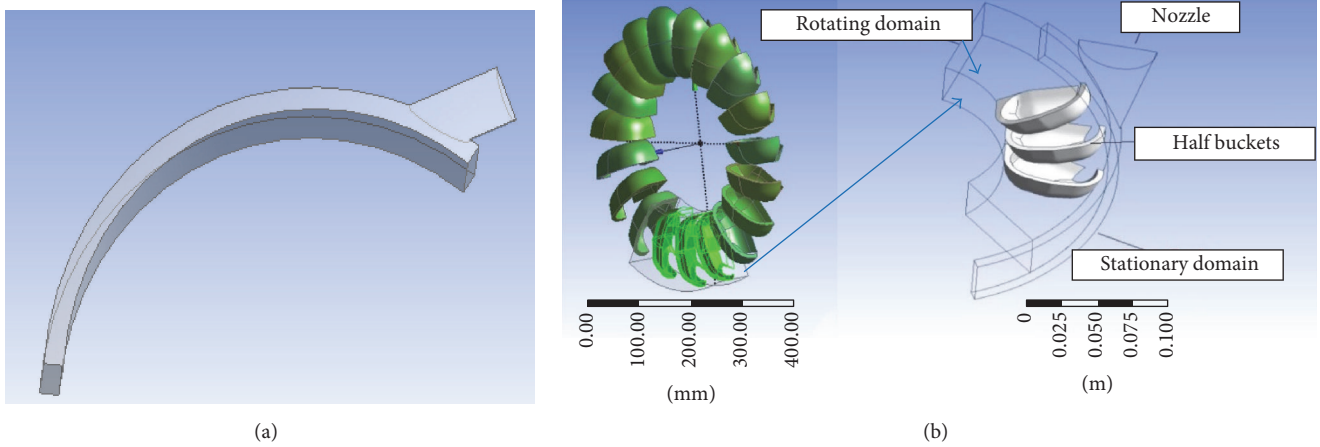


FIGURE 7: Domain geometries: stationary (a) and assembly of the rotating and stationary domain (b).

assumed to have no or minor effect when comparing the runner designs as follows. The following are some of the simplifying assumptions made in the analysis.

*No Casing.* Modeling the Pelton turbine without casing, similar methods can be found in the literatures [10, 11].

*Symmetry.* To reduce computational cost, the buckets, nozzle, and water-jet are cut in half at the symmetry axis [10, 11].

*Single Jet.* Modeling of only the single jet operation was found in most of the publications reviewed in Section 1 [10, 11].

*No Hub.* The flow will not be interacting with any other part of the runner except for the bucket. Hence, there is no need to include the hub into the CFD model, as suggested in the literatures [10, 11, 13].

*Periodic Torque.* Three buckets are enough to recreate the complete runner torque and are used also in this research [10, 11].

*“Similitude”.* Similitude in a general sense is the indication of a known relationship between a model and a prototype. Equation (7) represents head coefficient, flow coefficient, and power coefficient for model studies [10]. In order to achieve similarity between model and prototype behavior, all the corresponding terms must be equated between model and

prototype. So, the model is presumed to have the same values of speed ratio, flow ratio, and specific speed.

$$\begin{aligned} \left( \frac{H}{D^2 N^2} \right)_{\text{prototype}} &= \left( \frac{H}{D^2 N^2} \right)_{\text{model}}, \\ \left( \frac{Q}{ND^3} \right)_{\text{prototype}} &= \left( \frac{P}{ND^3} \right)_{\text{model}}, \\ \left( \frac{P}{D^5 N^3} \right)_{\text{prototype}} &= \left( \frac{P}{D^5 N^3} \right)_{\text{model}}. \end{aligned} \quad (7)$$

*Scaling Down.* Scaling down of the prototype is also important to reduce the time consumption and to ease the computational processing in normal computers. On the basis of the above considerations, the scaling factor of 0.53 was used to meet the minimum bucket width standard for model testing, and the Reynolds number also needs to be greater than  $2 \times 10^6$ . This is based on the international standard IEC 60193 of the International Electrotechnical Commission which applies to laboratory testing of model turbines [10, 23]. In this standard, the factor greater than 0.28 was found to satisfy IEC 60193 criteria for Pelton turbines.

Table 7 shows the values for prototype and model with the same speed of 520 rpm.

*3.2. Computational Domain Creation.* Figure 7 depicts the completed CAD drawings of the rotating and stationary

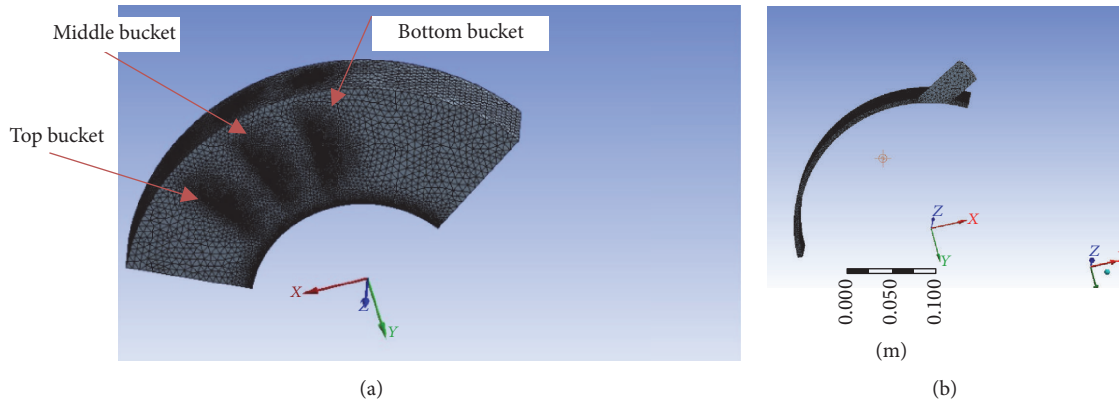


FIGURE 8: Meshed rotating (a) and stationary domain (b) sizing and inflations were applied.

domain which is modeled separately and assembled here to show their relative initial positions. Stationary domain contains half a cylinder for the inlet and a ring to accommodate an interface between the two domains.

Imagine that the rotating domain in Figure 7 is aligned with the stationary domain. When the rotating domain leaves this position, another identical domain is introduced at the top (the same geometry). Thus, one achieves a continuous simulation of a runner [11].

**3.3. Meshing.** Figure 8 shows both stationary and rotating domains meshed as they are imported into CFX-Pre. As suggested in the literature [10, 19], unstructured tetrahedral elements were used for the rotating domain meshing because of more complex geometry to be captured by the mesh and also to allow automatic meshing for all the upcoming geometry modifications. In order to determine the minimum grid size or mesh resolution required to resolve the boundary layer and the mean flow features, a grid independence study was conducted. This allows minimization of errors and uncertainties in the predicted results, for example, the runner power output or the efficiency. Therefore, grid convergence analysis has been carried out considering power output (in this study by monitoring torque) as a parameter of significant interest. The results of grid independence study are presented in Section 3.6.

**3.4. Physical Setup with ANSYS Preprocessing.** In this section, the essentials of the ANSYS Pre setup are presented.

**Analysis Type.** In each “Flow Analysis” in ANSYS Pre there is a tab called “Analysis Type.” This is where one defines whether or not the simulation is transient or steady-state, control simulation time and time steps. In this case, the transient option was chosen. Time steps are interval for which CFX solver calculates flow parameters in transient analysis. The time step was 1/20 total time, which corresponds to 0.001714 sec to capture 20 time frames per rotation.

**Multiphase Model.** The flow through the penstock pipe is having only single phase for the fluid. As the water-jet comes

out of the nozzle, it is directly freed to the atmosphere and the effect of free water-jet will come into picture. This flow passes through runner buckets, and it will be a free surface flow. This free surface flow glides through internal surface of the buckets and the momentum transfer takes place. The flow leaving the runner bucket will be converted into dispersed water droplets as the fluid leaves contact from the buckets. This way the flow through the Pelton turbine is multiphase in nature in agreement with the literatures [10, 11, 13, 14]. To capture the flow accurately, homogenous multiphase analysis is performed in this research.

**Volume Fraction of Water.** As suggested by the literature [5], the volume fraction of water should change from 0 to 1. In each control cell, the volume fractions of the water and air sum to 1,  $\alpha_w + \alpha_g = 1$ . Then  $\alpha_w = 0$  denotes cells filled with air, while  $\alpha_w = 1$  denotes cells filled with water and  $0 < \alpha_i < 1$  denotes that the cell contains an interface between the water and air. In the beginning of the simulation, both domains are full of air with 0 m/s velocity. Therefore, the given initial conditions are 0 m/s velocity and 0 Pa for relative pressure. Initial water volume fraction is 0 and initial air volume fraction is 1.

**Turbulence Model.** Shear Stress Turbulence (SST) model is able to capture turbulent scales in flow in high shear stress regions [10, 11]. So SST turbulence model is chosen for further simulations.

**Domain Interface.** The interface type between the stationary and rotating domains was Fluid-Fluid [10, 11]. Interface model for this type was General Connection and the Transient Rotor Stator option was selected for Frame Change/Mixing Model. Pitch ratio was maintained to value 1 between domain interfaces by maintaining equal area in interface region. To apply a rotation to the rotating domain, domain motion in the rotating domain was set to rotating, and angular velocity was defined by the expression “Omega.” In this case, the angular velocity is negative because the domain was modeled to rotate in the negative rotation direction about the z-axis. This method is also found in the literatures [10, 11, 14].

TABLE 8: Expressions defined in ANSYS Pre for the baseline design [5, 11].

Name	Expression	Description
Gravity	9.82 [ms <sup>-2</sup> ]	Acceleration due to gravity
Head	13.34 [m]	Model head based on scaling
Turbine radius	132.5 [mm]	Model turbine radius based on scaling
Inlet velocity	$(2 \times \text{gravity} \times \text{head})^{0.5}$ [m/s]	Water velocity at the nozzle inlet
Omega	Inlet velocity/(2 × turbine radius) [rad/s]	Angular velocity: rotation in the negative direction is selected
Torque middle bucket wall	<i>Torque_z@Middel Bucket Wall</i>	The entire middle bucket is selected
Total time	$((120 \times \text{pi})/180)/\text{Omega}$	Total simulation running time

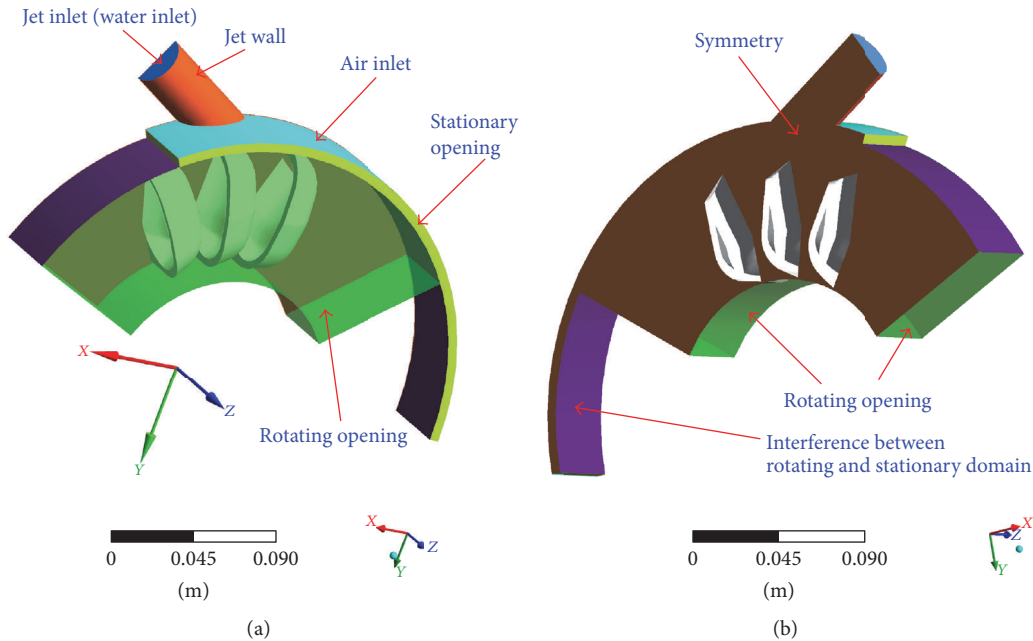


FIGURE 9: Boundaries applied on the domains.

**Boundary Condition in Rotating Domain.** This section contains a list of boundaries and their conditions. No boundary for outlet is defined in the rotating domain. Rather, opening type boundary condition has been defined. The bucket surface is defined by wall type boundary condition and an interface type boundary condition at interface between the rotating and stationary domain. All other remaining boundaries are defined as opening type since it is unpredictable about the actual outlet and flow pattern of fluid through the runner. An overview of the boundary conditions can be found in Figure 9.

**Solver Control and Output.** The chosen advection scheme was High Resolution according to the CFX Modeling Guide. This gives a good compromise between robustness and accuracy. Second-Order Backward Euler option was selected for the Transient Scheme as it is generally recommended for most transient runs in CFX [5, 10, 11, 13, 14].

**Monitor Points.** The main output of the simulation is the total torque on the middle bucket. A monitor for the expression “*Torque on Middle Bucket Wall*” was added, which logged the

torque and made it possible to monitor the torque during the simulation. The calculated torque data on the middle bucket was extracted from the simulation using an inbuilt torque function applied to the Named Selections created for the regions for the middle bucket. This function is then plotted as a Monitor Point, while the simulation runs, allowing the calculated torque at each time step to be exported.

**Expressions.** Defining expressions is a good way of streamlining a CFD case. The expressions in Table 8 are used in the setup. This way of defining expressions can be also found in the literatures [5, 11].

**3.5. Result and Discussion.** In general rule, a small runner is cheaper to manufacture than the larger one. It takes less material to cast it and the housing and associated components also can be smaller. For this reason, consequences of reducing PCD (=400 mm) from the baseline design (PCD = 500 mm) are evaluated and results are compared with those published by Panthee et al. [10] and Panagiotopoulos et al. [19], respectively. The geometrical characteristics of their Pelton turbine model used for their study correspond to a Pelton

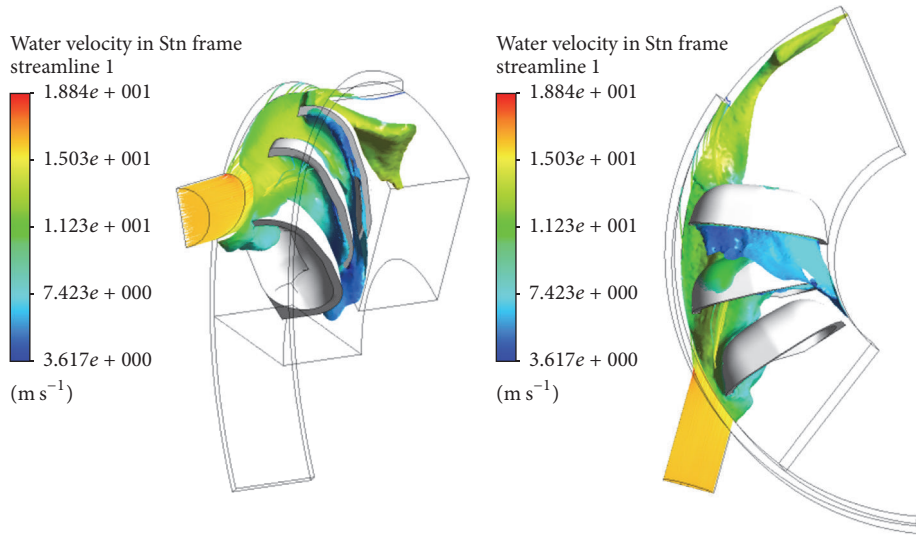


FIGURE 10: Flow visualization of the baseline design, side views, and face views (PCD = 500 mm).

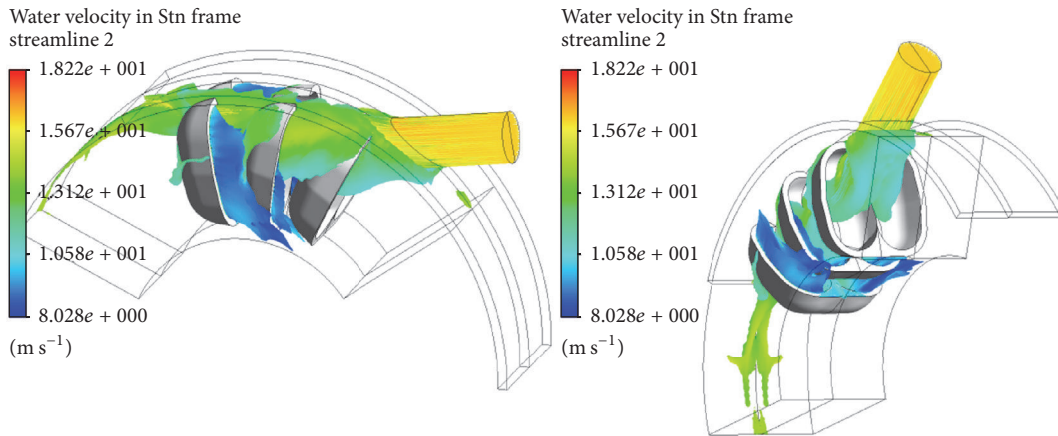


FIGURE 11: Flow distribution of the runner: water velocity in Stn frame, side views, and face views (PCD = 500 mm).

turbine installed in Khimti Hydropower in Nepal [10] and the National Technical University of Athens [19], respectively. The PCD of the model runner for both power plants was 400 mm, and the axis is horizontal with two injectors.

Next, a visualization of the flow in the turbine buckets for this study can be seen in Figure 10.

As seen in Figures 10 and 11, only very small amount of “leaked” water is present next to the bottom bucket with low jet velocity. These visualizations give good information about the flow pattern. The streamlines that came from the nozzle entered into the runner, hitting the buckets and dividing the jet into three portions (Figures 10 and 11). First, the portion from the bottom of the jet touched the outside and inside of the top bucket that is close to the nozzle. The second portion of the jet was the one from the middle, which hit the next middle bucket. Finally, the rest portion of the jet crossed into the latter bucket. On the face and side view on Figure 10, one can observe the part of the flow escaping from the cutout of the bucket as well as the lateral sheet flow.

It can be observed on Figure 12 that the maximum pressure point, in red, corresponds to the PCD of the bottom bucket and the tip of the middle bucket which is aligned with the axis of the impinging jet. Similar finding is observed in the literature [10].

As seen in Figure 13, when the PCD is reduced to 400 mm, a large amount of water does not leave the buckets, causing severe backwash on the backside of the bucket, which varies from certain sound value at the place of impingement to the reduced values as water goes outward (Figure 13(b)). However, there is a small amount of the flow that leaves through the cutout with high velocity without being utilized (cutout leakage). This phenomenon has to be reduced during the optimization stage.

The water is unevenly distributed across the buckets and there are several local accumulations of cells with a high volume fraction of water, most visible in the bottom bucket in Figure 14. This volume of fraction of water will vary with time as the buckets rotate. This occurs when the portion of

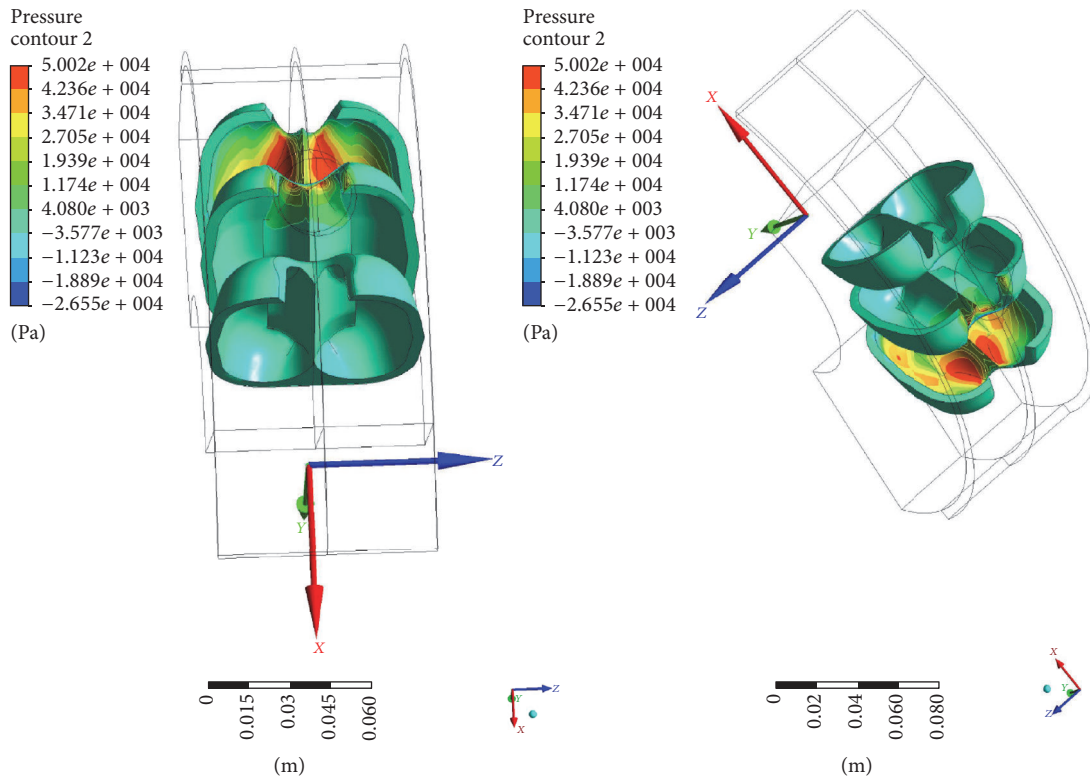


FIGURE 12: Pressure contours on the bucket (PCD = 500 mm).

the jet is going to leave out completely from the bottom bucket and completely enters the next top and consequential buckets. The red and blue regions show, respectively, water and air in the computational domain. In a more complex situation, the atmosphere also exerts pressure on the surface (water-vapor interface) [24].

Looking at Figures 13(b) and 14, it is clear that, as the water starts entering into the top bucket, the inner surface of the middle and bottom bucket will still be having some water volume fraction inside it. It means that, for a particular instance of time and runner rotation, more than one of the runner buckets are having water volume fraction. The amount of the water flow touching the runner bucket sides and back surface of the bucket (backwash) is also visible. This water fraction at the back side and side surface of the bucket will impart some force to the buckets and if this fraction is high, then the intensity of force on the bucket will be higher and it will reduce the strength of the buckets [11, 13, 14]. Another effect of this is that the water is acting as a brake on the runner, rather than helping it turn, and this gives a serious loss of power. These energy losses occur with jet entering the bucket and providing some amount of counter-torque as the outer side of the bucket hits by the surface of the jet.

The pressure distribution in the bucket was due to impact of high jet. This pressure distribution applied on the bucket again varies with the time due to the rotation of the runner. It was found that the pressure peaks are obtained at bucket tip and PCD of the runner. The pressure peak in bucket tip is due to flow disturbance when jet strikes bucket tip. It is obvious to

obtain the pressure peak at the runner PCD since the Pelton runners are designed such that it would convert most of the hydraulic energy to mechanical energy when the jet strikes the runner PCD. Result showed high pressure with the value of  $3.559 \times 10^4$  Pa for the first top and the second middle bucket at some degree of rotation of the runner as shown in Figure 15. This pressure value is lower than the previous value when PCD = 500 mm (Figure 12). This might indicate that there is energy loss in the runner.

The images in Figure 15 are taken of the right bucket half; then it is mirrored here to ease the comparison through symmetry. The next step will be focused on future simulations regarding the study of the hydraulic efficiency; a better approximation of the numerical torque.

The hydrodynamic torque and the hydraulic efficiency of the runner are computed after completing the evaluation of a jet-bucket interaction flow, starting from the moment of impingement (jet cut in) until the evacuation of the bucket (jet cutout) [11]. The calculations are then continued for the particles of the oncoming frames, until all particles of a frame impinge on the next coming bucket (jet cut). As can be observed in Figure 15, the shape of the torque curve is also similar to the previous studies by different authors [10, 19], but the irregularity of the curve in this area was attributed due to the Coanda effect and the impact of the back flow which creates counter-torque on the bucket and makes it slightly different from the previous studies [5, 11, 19]. Some indicative pictures from the turbine examined here show how the energy transfer occurred in a single bucket as illustrated in Figure 16.

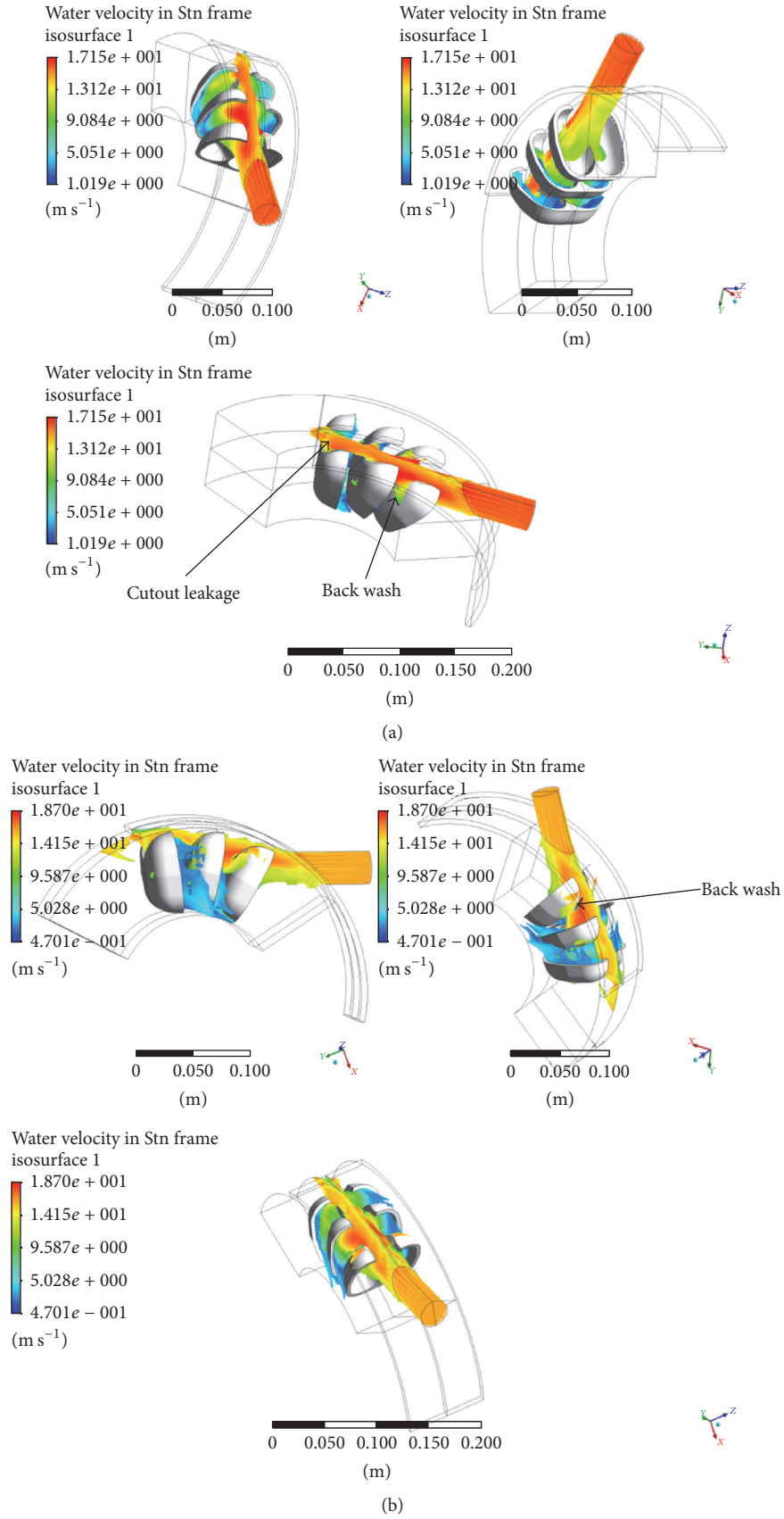


FIGURE 13: Flow distribution of the runner: water velocity in Stn frame, side views, and face views (PCD = 400 mm).

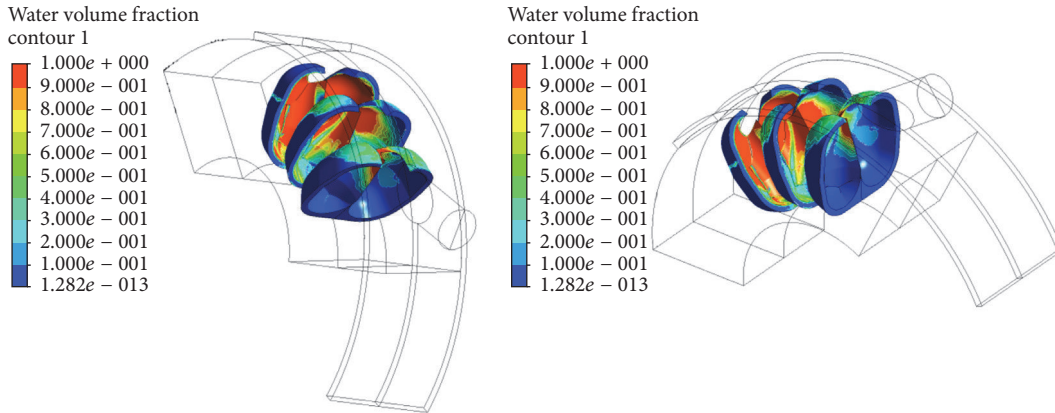


FIGURE 14: Volume fraction of water for reference bucket design at a particular time step (PCD = 400 mm).

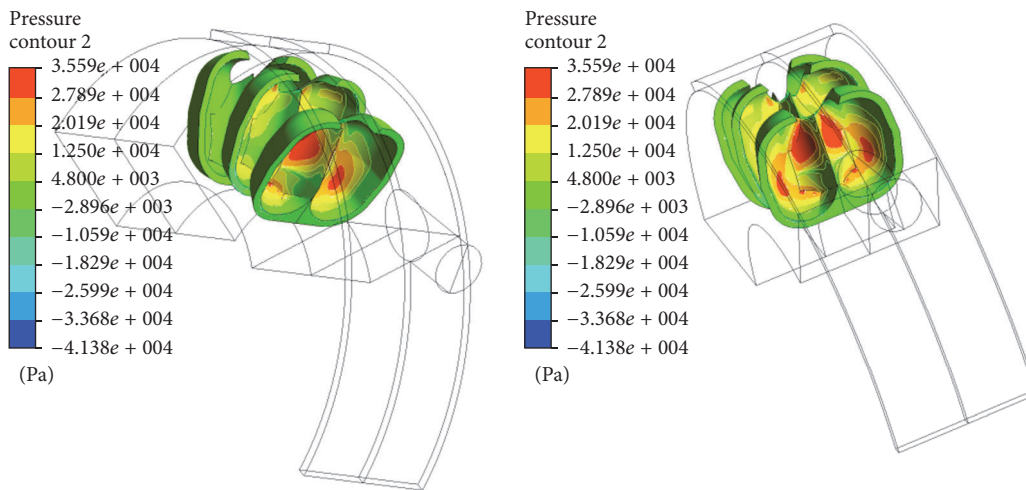


FIGURE 15: Pressure distribution at some degree of rotation of reference bucket design (PCD = 400 mm).

At the start (cut in) a counter-torque can also be observed caused by the interaction of the jet with the back surface of the bucket; this value is larger for PCD = 400 mm comparing to the baseline design (Figure 16). Just afterwards, the torque is increasing as more water interacts with the inner surface until the full jet interacts with the bucket to produce the maximum torque. The maximum torque produce by the baseline design (500 mm) is larger than that of a reduced PCD (400 mm). The result in Figure 16 shows also that smaller turbine is faster than the larger one which is true.

Next, the total curves of the complex unsteady flow in the bucket for the seven buckets analyzed can be acquired with the aid of time history views like the ones in Figures 17 and 18. The total torque curve is shifted by the single blade passage phase for the whole range of total torque values and summed to give the total torque acting on the turbine shaft. In this research paper, the torque generated by the middle bucket is replicated over time to determine total torque generated by Pelton turbine. This is done by assuming that at stable conditions every bucket is producing identical torque periodically. The replication was done till the summation graph gave steady values which occurs after

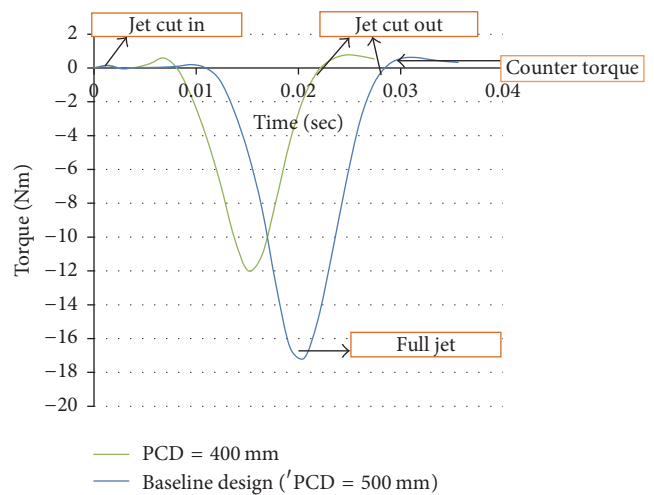


FIGURE 16: Torque generated by middle bucket versus time.

three buckets covered by the water sheets at 0.03 sec of the rotation of the runner. The plot obtained was due to half

TABLE 9: Mesh dependent test analyzed for PCD = 500 mm.

Mesh type	M1	M2	M3	M4	M5	M6	M7	M8
Total number, elements	294952	520687	2011665	2239650	2398044	2861243	3955723	5050204
Calculated total torque (Nm)	-30.93	-32.20	-34.32	-34.50	-34.69	-34.92	-35.02	-35.25
Standard torque (Nm)	-35.06	-35.06	-35.06	-35.06	-35.06	-35.06	-35.06	-35.06
Torque error percent (%)	11.8	8.2	2.1	1.6	1.1	0.4	0.1	0.5

TABLE 10: Mesh dependent test analyzed for PCD = 400 mm.

Mesh type	M1	M2	M3	M4	M5	M6	M7	M8
Total number, Elements	128251	128546	130961	2321026	3019180	4052422	4771226	6855793
Calculated total torque (Nm)	-18.13	-18.15	-18.29	-21.84	-22.15	-22.27	-22.37	-22.41
Standard torque (Nm)	-28.05	-28.05	-28.05	-28.05	-28.05	-28.05	-28.05	-28.05
Torque error percent (%)	35.4	35.3	34.8	22.1	21.0	20.6	20.2	20.1

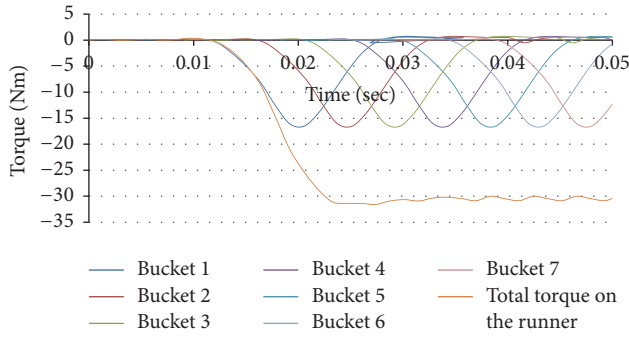


FIGURE 17: Dynamic runner and bucket torque over time for (PCD = 500 mm).

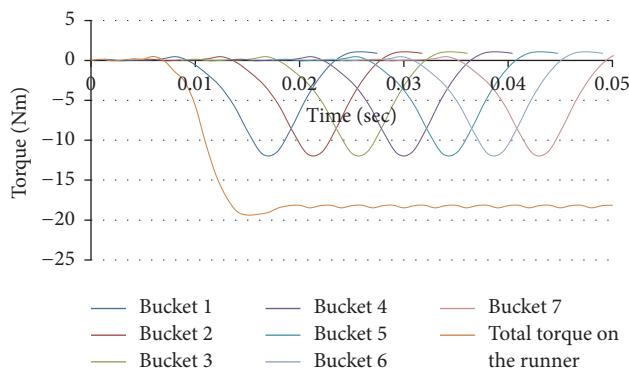


FIGURE 18: Dynamic runner and bucket torque over time for (PCD = 400 mm).

nozzle and the maximum torque on the runner at a time is given by peak value multiplied by 4 as there are two nozzles in each unit. This runner torque has been taken for power output calculations by taking the average value from 0.03 to 0.05 sec of the runner rotation. Methods of calculating the power output from a single bucket torque readings similar to

those described above are quite common and can be found in the literature [10–12].

To calculate the efficiency, power input has to be calculated as well which for a complete turbine is calculated using two variables describing the flow conditions: the net pressure head and the flow rate [11].

$$P_{\text{input}} = \rho g Q H_{\text{net}},$$

$$P_{\text{out}} = \frac{2 \times \Pi \times N \times T}{60}. \quad (8)$$

Therefore, (hydraulic) runner efficiency in this model was calculated using (9) as follows:

$$\eta = \frac{P_{\text{output}}}{P_{\text{input}}}. \quad (9)$$

The next validation phase is to compare efficiency of this model to the published results by Panthee et al. [10] and Panagiotopoulos et al. [19]. This will be done after checking the accuracy of the model, in agreement with the literature [10, 19].

**3.6. Mesh Independency Study and Model Validation.** Mesh or grid independent study is done in order to get a solution that does not vary significantly even when we refine our mesh further. Eight different mesh sizes were tested with an effective head of 47.5 m for two different cases. The mesh size on the rotating domain is controlled by element size. The relevance was increased for finer mesh. Afterwards, the orthogonal quality of the mesh has been checked and it was in an acceptable range (0.15–1.00) for each mesh developed. Each mesh was also created with the same physical setup and boundary conditions. During the simulations, results obtained were directly dependent on the accuracy in quality of mesh. And it was performed while analyzing the torque variation by developing the SST turbulence model.

Tables 9 and 10 indicate the grid information, the calculated torque, the standard torque, and the resulting modeled

TABLE 11: Validation and performance prediction of Pelton runner.

Parameters	Unit	Baseline design test cases			Off- design test cases			Published result by Panthee et al. [10]	Published result by Panagiotopoulos et al. [19]
Head	m	47.5	53.9	100	47.5	53.9	100	53.9	100
Flow rate	m <sup>3</sup> /s	0.14	0.05	135% BEP	0.14	0.05	135% BEP	0.05	135% BEP
PCD	mm	500	500	500	400	400	400	400	400
Runner speed	Rpm	520	520	520	650	600	1000	600	1000
Number of buckets	—	18	18	18	18	22	22	22	22
Model efficiency	%	78.8	83.5	84.6	62.6	66.1	71.6	82.5	86.7

runner efficiency for two different cases, namely, the baseline design (PCD = 500 mm) and the reduced size (PCD = 400 mm), respectively.

The standard torque was calculated with the power obtained from power coefficient and the angular velocity of runner for comparison. One can observe that, from the result in Tables 9 and 10, a finer mesh will give a solution of a little higher accuracy than required but at the expense of computational power and time. About 3.9 million elements were required to obtain mesh independent result, for PCD = 500 mm (Table 9). Similarly, for the PCD = 400 mm turbine, a total number of 6.8 million mesh elements were required to obtain mesh independent results for the torque output (Table 10). A solution was considered grid independent for less than 0.3 difference in the torque output between three different consecutive mesh sizes. It appears that no significant enhancement is to be expected from a further refinement of the mesh. As seen from the results, a relative error of 20.1%, between the CFD and the analytical data, was found for turbine with PCD = 400 mm and 0.1% relative error for the baseline turbine (PCD = 500 mm) at the design-point operating condition ( $Q = 0.14 \text{ m}^3/\text{s}$  and  $H = 47.5 \text{ m}$ ). Hence, high value of relative torque error indicates that there are losses in the reduced size of the turbine, influencing the efficiency characteristics. The torque variation curves of the runner obtained using different density meshes are also presented in Figures 19 and 20.

Table 11 shows the performance prediction and comparison of the model results with two published results.

The computational analysis results presented in Table 11 showed that the performance of the baseline’s turbine design was very good since the relative error is only 0.4% at the design operating conditions. Torque value from mesh (M7) resulted in 78.8% of model runner efficiency for PCD = 500 mm (baseline design). The postprocessing visualization (Figures 10 and 11) was able to qualitatively show that the reason for the better performance for the case of baseline design may be explained by less cutout leakage and a more optimal bucket design for its intended use. As presented in Table 11, the model hydraulic efficiencies for reduced size of the turbine (PCD = 400 mm) for mesh (M8) were only 62.6%, 66.1%, and 71.64%. It can be observed that, from the results of the different cases analyzed, these hydraulic efficiencies were remarkably lower than that of the baseline

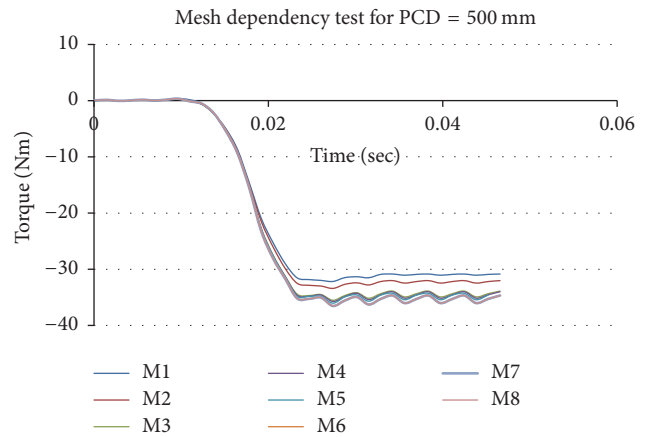


FIGURE 19: Total torque variations for different mesh sizes for PCD = 500 mm.

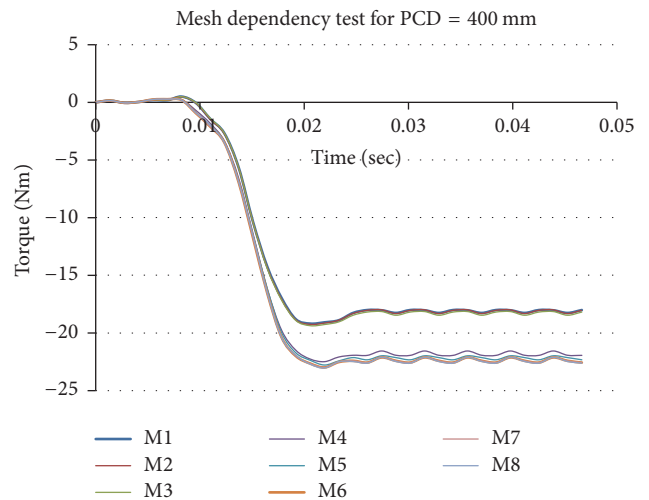


FIGURE 20: Total torque variations for different mesh sizes for PCD = 400 mm.

design. Moreover, it can be observed that for a reduced flow rate and an increase in number of buckets equal to  $0.05 \text{ m}^3/\text{s}$ , 22, respectively, more water was caught by the inner surface of the buckets. This could explain why the predicted efficiency increases rapidly for volume flow less than the design flow

rate. The lower efficiency of the model at off-design condition (PCD = 400 mm) is mainly due to a little back splash (the breaking effect) on the bucket and the missing jet velocity (leakage flow rate) because of a nonoptimized bucket design. As this phenomenon highlighted before, the qualitative views of Figures 13–15 are reasonable for the lower efficiencies in the off-design cases. Thus, the goal was to compare flow visualization at these two conditions, using image postprocessing, in order to explain the difference in runner performance. An explanation for the discrepancy is that a decrease in PCD from the baseline design (PCD = 500 mm) to PCD = 400 mm would lead to high hydraulic losses, even though it will result in less value of manufacturing cost. It is important to note that the bucket shape used in the baseline design (as shown in Figure 4) in this paper is based on Jeremy Thake 2000 book [6]. In this book, it is suggested that “the design jet diameter is 11% of PCD” which will give a PCD of approximately 500 mm. Therefore, if we optimize/change the shape of this bucket for each case analyzed above, the optimum results presented in both published results above and the reduced size of the turbine (PCD = 400 mm) might be different from this study. For future work, the design optimization of this turbine bucket will be made by keeping the PCD to be 400 mm, to lower the manufacturing cost and improve efficiency of the runner. CFD results by Židonis and Aggidis [25] also show that less number of buckets were required to increase the hydraulic efficiency. Therefore, as the final step, it was decided to change the length, depth, and angular position (jet-bucket interaction) and alter the surface close to the lip and redefine the shape of the lip curve to reduce the leakage, intern to reduce the energy loss.

#### 4. Conclusion

The next-generation turbine designs for small-scale hydro-power systems seek higher efficiency and low manufacturing costs. The (size of Pelton turbine) PCD is an important parameter to lower the manufacturing cost of a Pelton turbine runner. However, no consistent guidance based on numerical research data is available in the public domain. This study provides a guideline for selecting, designing, modeling, and performance analysis of a micro hydro Pelton turbine and provides an example of how the size of turbine (PCD) can affect the efficiency of the turbine.

The paper describes also the methods used for CFD analysis of scaled model Pelton turbine which is ideally designed for Melkey Herra Village hydropower plant using ANSYS CFX software. The bucket model was designed according to the baseline design or calculated parameters. The time and cost in CFD analysis of Pelton turbine are also reduced by selecting 3 buckets to predict the flow behavior of complete turbine. One of the objectives was to understand how the turbine performance will change when the flow field is perturbed by reducing the size of turbine for a given operating condition (i.e., flow rate and head). Results obtained from the baseline design (PCD = 500 mm) have been successfully compared to that of the reduced size (PCD = 400 mm) of the turbine. The results of the two turbine designs at the design flow rate and head of turbine are as follows: one turbine (PCD =

400 mm) has a maximum efficiency of 62.6% and the baseline design turbine (PCD = 500 mm) has a maximum efficiency of 78.8%. The flow visualization study of this research provides insights into the reasons for efficiency as well as guidance for improving the efficiency. The low efficiency in the reduced size of the turbine is mainly caused by a large amount of water leaving the bucket through the lip and hence transferring close to zero of its energy to the shaft. The problem was therefore the choice of the runner PCD that could give the best advantages in terms of efficiency on the whole plant's operational field. For the purpose of validation and performance characterization, two Pelton turbines reported in the literature were considered. The first turbine has PCD = 400 mm, a maximum efficiency of 82.5%, which was studied by Panthee et al., 2014, for Khimti Hydropower in Nepal [10]. The second turbine has also the same PCD (=400 mm) but with a maximum efficiency of 86.7%, which was studied by Panagiotopoulos et al., 2015 [19], using a reference case corresponding to a Pelton turbine installed in the LHT, at the National Technical University of Athens. These were essential for the purpose of computational validation and performance characterization.

The design optimization, production, and experimental testing of a model runner based on this design may also be realized in the next part of this paper. Based on the result obtained, this study planned a modification on the baseline design and will consist of the following new designs being tested:

- (i) Changing the length, depth, angular position (Jet-bucket interaction), and number of the buckets while keeping all other parameters constant
- (ii) Altering the surface close to the lip and redefining the shape of the lip curve to reduce the leakage

Based on the results presented in this study, there are opportunities for improving the maximum efficiency as well as reducing manufacturing cost of Pelton turbines, if the design is prescribed using the above criteria, followed by high-fidelity computational simulations. It would then no longer be necessary to start the design and numerical simulation each time from scratch.

A natural extension of this paper would be also to validate the model for other selected sites. Achieving such a goal would be a great step towards improving the understanding of the micro hydro power development and making tools for validating CFD results, so that the benefits of this technology can be brought to rural populations.

#### Abbreviations

CFD:	Computational fluid dynamics
CFX:	CFD code by ANSYS
SST:	Shear stress transport
VOF:	Volume of fluid
MHP:	Micro hydro power
MHT:	Micro hydro turbine
MWIE:	Ministry of Water, Irrigation and Energy
BEF:	Best efficiency point.

## Conflicts of Interest

The authors declare that they have no conflicts of interest.

## Acknowledgments

This paper was funded by Ministry of Water, Irrigation and Energy. The authors would like to thank Ministry of Water, Irrigation and Energy Office for the fund and for all information and data provided to accomplish the research work.

## References

- [1] Energy Situation, <https://energypedia.info/wiki/Ethiopia>.
- [2] A. Dalelo, Rural Electrification in Ethiopia, opportunities and bottlenecks, Addis Ababa University, College of Education.
- [3] World Small Hydropower Development Report 2013– The Need for Further Resource Assessments, L. Esser, International Center on Small Hydro Power, Division of Multilateral Development, Hangzhou, Ethiopia.
- [4] S. Melessaw, “Ethiopia’s Small Hydro Energy Market-GiZ–target market analysis-hydro ethiopia,” <http://www.german-energy-solutions.de/enwww.gtz.de/projektentwicklungsprogram>.
- [5] L. F. Barstad, *CFD Analysis of a Pelton Turbine [Master, thesis]*, Norwegian University of Science and Technology, 2012.
- [6] J. Thake, *The Micro-Hydro Pelton Turbine Manual: Design, Manufacture and Installation for Small-Scale Hydro-Power*, ITDG publishing, London, UK, 2000.
- [7] Z. Zhang, Pelton turbines book, published by Springer Nature, the registered company is Springer International Publishing, AG, Switzerland, 2016.
- [8] MHPG, Series, “Harnessing Water Power on a Small Scale” Vol. 9 (Micro Pelton Turbines), Published by SKAT, Swiss Center for Appropriate Technology, 1991.
- [9] A. Harvey, Micro hydro design manual, a guide to small scale water power schemes.
- [10] A. Panthee, B. Thapa, and H. P. Neopane, “CFD Analysis of pelton runner,” *International Journal of Scientific and Research Publications (IJSRP)*, vol. 4, no. 8, 2014.
- [11] A. Židonis, A. Panagiotopoulos, G. A. Aggidis, J. S. Anagnostopoulos, and D. E. Papantonis, “Parametric optimisation of two Pelton turbine runner designs using CFD,” *Journal of Hydrodynamics*, vol. 27, no. 3, pp. 840–847, 2015.
- [12] J. D. Anderson, *Computational Fluid Dynamics: The Basics with Applications*, McGraw-Hill, New York, NY, USA, 1995.
- [13] A. Perrig, *Hydrodynamics of the free surface flow in Pelton turbine buckets [Ph. D. Thesis]*, École polytechnique féd, 2007.
- [14] A. Perrig, F. Avellan, J.-L. Kueny, M. Farhat, and E. Parkinson, “Flow in a Pelton turbine bucket: numerical and experimental investigations,” *Journal of Fluids Engineering*, vol. 128, no. 2, pp. 350–358, 2006.
- [15] Y. X. Xiao, T. Cui, Z. W. Wang, and Z. G. Yan, “Numerical simulation of unsteady free surface flow and dynamic performance for a Pelton turbine,” in *Proceedings of the 26th IAHR Symposium on Hydraulic Machinery and Systems*, chn, August 2012.
- [16] M. Eisenring, Micro Pelton turbines. St. Gallen, Switzerland: Swiss Center for Appropriate Technology, 1991.
- [17] B. Janetzky, H. Ruprecht, C. Keck, C. Schärer, and E. A. Göde, “Numerical simulation of the flow in a Pelton bucket,” in *Proceedings of the in. IAHR*, pp. 276–283, 1998.
- [18] J. S. Anagnostopoulos and D. E. Papantonis, “A fast Lagrangian simulation method for flow analysis and runner design in Pelton turbines,” *Journal of Hydrodynamics B*, vol. 24, no. 6, pp. 930–941, 2012.
- [19] A. Panagiotopoulos, A. Židonis, G. A. Aggidis, J. S. Anagnostopoulos, and D. E. Papantonis, “Flow Modeling in Pelton Turbines by an Accurate Eulerian and a Fast Lagrangian Evaluation Method,” *International Journal of Rotating Machinery*, vol. 2015, Article ID 679576, 2015.
- [20] B. W. Solemslie and O. G. Dahlhaug, “A reference Pelton turbine design,” in *Proceedings of the IAHR, 26th IAHR Symposium on Hydraulic Machinery and Systems, IOP Conf.*, Earth and Environmental Science, Beijing, China, August 2012.
- [21] S. Pudasaini, H. P. Neopane, Amod P. et al., “Computational Fluid Dynamics (CFD) analysis of Pelton runner of Khimti Hydro-power Project of Nepal,” in *Rentech Symposium Compendium*, vol. 4, September 2014.
- [22] N. Tilahun, W. Bogale, F. Bekele, and E. Dribssa, “Feasibility study for power generation using off- grid energy system from micro hydro-PV-diesel generator-battery for rural area of Ethiopia: The case of Melkey Hera village, Western Ethiopia,” *AIMS Energy*, vol. 5, no. 4, pp. 667–690, 2017.
- [23] Hydraulic Turbines, Storage pumps and pump turbines- Model acceptance tests (IEC 60193), 1999.
- [24] F. M. White and I. Coreld, *Viscous Fluid Flow*, vol. 3, McGraw-Hill, New York, NY, USA, 2006.
- [25] A. Židonis and G. A. Aggidis, “Pelton turbine: Identifying the optimum number of buckets using CFD,” *Journal of Hydrodynamics*, vol. 28, no. 1, pp. 75–83, 2016.